2

Radiometric Constraints on the Timing, Tempo, and Effects of Large Igneous Province Emplacement

Jennifer Kasbohm[1], Blair Schoene[1], and Seth Burgess[2]

ABSTRACT

There is an apparent temporal correlation between large igneous province (LIP) emplacement and global environmental crises, including mass extinctions. Advances in the precision and accuracy of geochronology in the past decade have significantly improved estimates of the timing and duration of LIP emplacement, mass extinction events, and global climate perturbations, and in general have supported a temporal link between them. In this chapter, we review available geochronology of LIPs and of global extinction or climate events. We begin with an overview of the methodological advances permitting improved precision and accuracy in LIP geochronology. We then review the characteristics and geochronology of 12 LIP/event couplets from the past 700 Ma of Earth history, comparing the relative timing of magmatism and global change, and assessing the chronologic support for LIPs playing a causal role in Earth's climatic and biotic crises. We find that (1) improved geochronology in the last decade has shown that nearly all well-dated LIPs erupted in < 1 Ma, irrespective of tectonic setting; (2) for well-dated LIPs with correspondingly well-dated mass extinctions, the LIPs began several hundred ka prior to a relatively short duration extinction event; and (3) for LIPs with a convincing temporal connection to mass extinctions, there seems to be no single characteristic that makes a LIP deadly. Despite much progress, higher precision geochronology of both eruptive and intrusive LIP events and better chronologies from extinction and climate proxy records will be required to further understand how these catastrophic volcanic events have changed the course of our planet's surface evolution.

2.1. INTRODUCTION

The observation that large igneous province (LIP) magmatism has in some cases occurred concurrently with mass extinctions (Courtillot & Renne, 2003; Ernst, 2014; Ernst & Youbi, 2017; Ernst et al., Chapter 1 this volume) leads to the question of whether there is a cause-and-effect relationship between them. While various hypotheses exist as to how LIPs lead to catastrophic climate change that can lead to ecosystem collapse and mass extinctions, they generally focus on volatile release from either magma-derived gases or indirectly through heating of organic-, carbonate-, or evaporite-rich sediments (Bond & Sun, Chapter 3 this volume; Mather & Schmidt, Chapter 4 this volume; Self et al., 2006; Svensen et al., 2004; Thordarson & Self, 1996). Determining whether any of these mechanisms are important contributors to climate change requires understanding the relative rate of both extrusive and intrusive magmatism, and correlating these with paleoenvironmental records. The only way to directly date the rates of LIP emplacement is through radioisotope geochronology. Furthermore, as LIP lava flows and biological evidence for mass extinctions rarely occur in the same stratigraphic sections, making direct stratigraphic temporal correlation impossible, geochronology is also essential to test the plausibility of causality.

Although a wide range of geochronologic techniques have been applied to dating LIPs, uranium-lead (U-Pb)

[1]*Department of Geosciences, Princeton University, Princeton, New Jersey, USA*

[2]*United States Geological Survey, Volcano Science Center, Menlo Park, California, USA*

Large Igneous Provinces: A Driver of Global Environmental and Biotic Changes, Geophysical Monograph 255, First Edition.
Edited by Richard E. Ernst, Alexander J. Dickson, and Andrey Bekker.

DOI: 10.1002/9781119507444.ch2

and argon-argon ($^{40}Ar/^{39}Ar$) geochronometers are the most widely used geochronometers for this application because their parent isotopes are characterized by long half-lives and relatively high concentrations in a variety of mineral phases (Reiners et al., 2017; Renne et al., 1998a). Temporal correlation between some LIPs and mass extinctions was suggested over 30 years ago (McLean, 1985), and this was rapidly tested using $^{40}Ar/^{39}Ar$ geochronology on basalts (Courtillot et al., 1986; Duncan & Pyle, 1988). However, not until the 1990s were $^{40}Ar/^{39}Ar$ and U-Pb geochronology used to demonstrate a temporal coincidence between the Siberian Traps LIP and the end-Permian mass extinction to within ~1 Ma (Campbell et al., 1992; Dalrymple et al., 1995; Renne & Basu, 1991; Kamo et al., 2003; Reichow et al., 2002). Attempts to further correlate LIPs and mass extinctions have both capitalized on and pushed the development of higher precision geochronology. Because the duration of the hypothesized individual environmental effects of LIPs can vary in timescale from years (cooling associated with sulfate aerosols, acid rain, ozone depletion) to 100 ka (warming associated with CO_2) (Black & Manga, 2017; Wignall, 2001), greater and greater precision is required to test hypotheses relating LIPs to paleoclimate and paleontological records. Geochronological uncertainties >1 Ma, which were commonplace in data sets from the early efforts to date these events, obscure the relative timing of LIP eruptions versus global change on relevant climatic timescales, and limit assessment of the plausibility of a causal connection. However, the last decade has seen dramatic improvement in the precision and accuracy of dates generated by radiogenic geochronology, such that recently published data sets can begin to compare and resolve relative timing differences between the onset and duration of LIP magmatism and potential downstream environmental effects, such as biotic decline, ecosystem deterioration, global warming and carbon cycling, and sea level change. With methodological advances in U-Pb geochronology, it is now possible to discern a coincidence of events with precision of 10–100 ka, allowing testing of a potential causal connections at the sub-100 kyr level. However, further increases in analytical precision of dates for LIPs and of age models for stratigraphic sections that contain paleoenvironmental records will be required in order to resolve the timing of environmental effects operating on shorter timescales, such as cooling due to SO_2.

In this chapter, after describing the methodological advances that have led to improved accuracy and precision in geochronology, we will review the geochronology of 12 LIP–global environmental change couplets (Fig. 2.1). We chose to focus on LIPs that coincided in time with a dramatic global environmental event, and further narrowed that focus to pairs wherein the LIP and/or the environmental event had been the subject of recent high-precision geochronological study. To complement our narrative review below, we also present tables detailing the samples included in our analysis (see Tables 2.1 and 2.2). This new compilation is able to highlight some similarities and some differences between LIPs that permit discussion of both the geodynamics of LIPs and their timing relative to environmental catastrophes.

2.1.1. Dating Methods for Large Igneous Provinces

Most dates for LIPs and their corresponding environmental perturbations are derived from the $^{40}Ar/^{39}Ar$ or U-Pb techniques. Historically, $^{40}Ar/^{39}Ar$ studies have yielded a temporal framework of LIP emplacement at ~1% resolution (e.g., Barry et al., 2013; Kerr et al., 2003; Marzoli et al., 2018; Renne et al., 1995), sufficient to establish a broad correlation, but in excess of that required to resolve the relative timing of LIP emplacement relative to environmental change. This relatively coarse resolution is due to small concentrations of the parent isotope, ^{40}K, found in whole-rock basalt samples or plagioclase separates. U-Pb geochronology can yield higher-precision dates (to better than ± 0.1%), but amenable minerals (e.g., zircon, baddeleyite) are not ubiquitous in LIPs. With their particular strengths and shortcomings, both techniques have been crucial to improving understanding of the connection between LIPs and environmental change, and working to better understand that connection has produced methodological breakthroughs in both geochronometers. In this section, we will briefly describe the methodological advances leading to improved accuracy and precision for both techniques, with a stronger focus on U-Pb methods as these have provided the majority of high-precision ages discussed in this review. We follow the definitions of accuracy and precision summarized in Schoene et al. (2013): An accurate date agrees with the actual age of an event within uncertainty, while precision is defined as the reported uncertainties, which may include both random and systematic uncertainties (Renne et al., 1998b; Schoene, 2014).

The accuracy of $^{40}Ar/^{39}Ar$ dates has increased as methodology evolved from analyzing primarily LIP whole-rock/groundmass samples, to more recent efforts focused on analysis of aliquots of plagioclase or biotite separated from basalts, or sanidines separated from intercalated silicic ashes. These recent studies have also used more careful means to handpick plagioclase grains to avoid the effects of weathering, and choosing grains of sufficient size to mitigate effects from ^{39}Ar recoil (Renne et al., 2015). New procedures also treat translucent, inclusion-free grains with an HF solution in an ultrasonic bath to

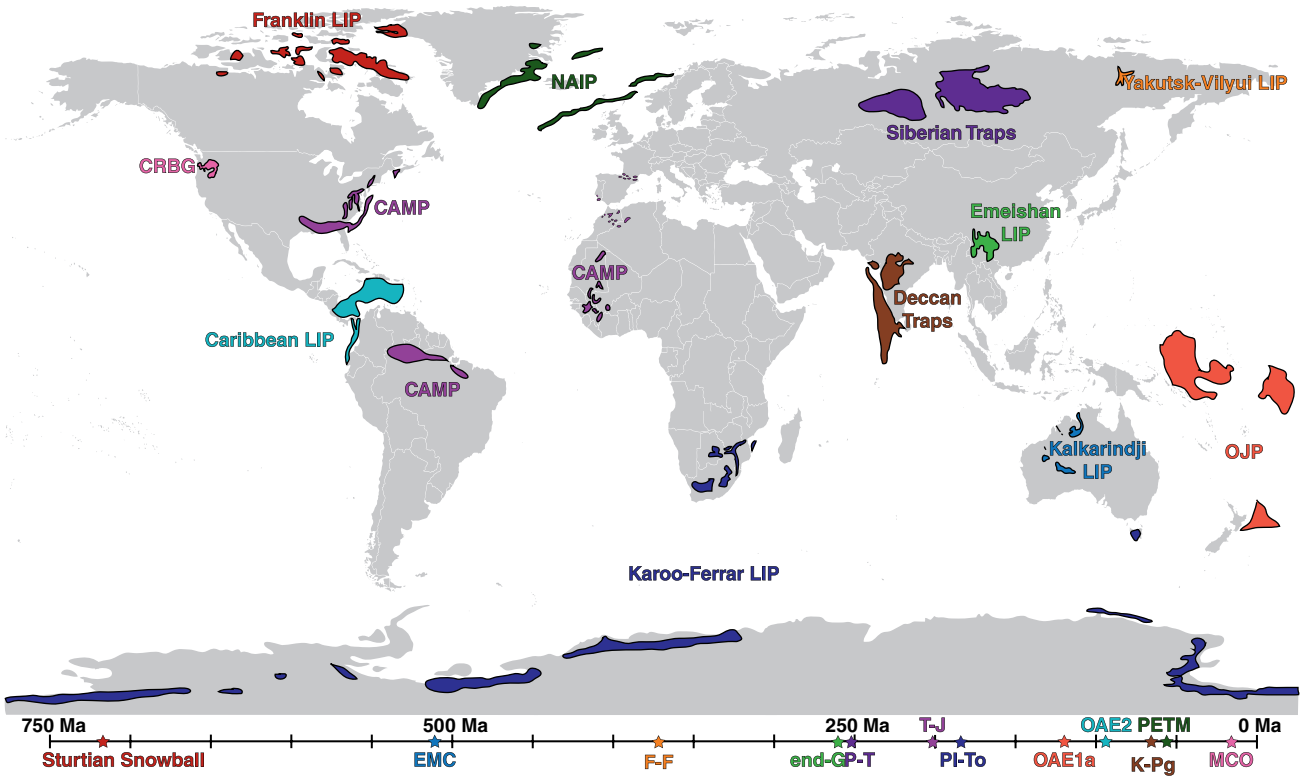

Figure 2.1 Map of large igneous provinces. This map shows the current location of the large igneous provinces described in Chapter 2, after Bryan and Ferrari (2013). Below, a timeline shows the ages of the global events with which the LIPs are associated. LIP/event couplets are color coded, and the ages of the LIPs overlap with the ages of the events shown on the timeline. CAMP: Central Atlantic Magmatic Province; CRBG: Columbia River Basalt Group; EMC: Early-Middle Cambrian extinction; F-F: Frasnian-Famennian extinction; end-G: end-Guadalupian extinction; K-Pg: end-Cretaceous extinction; MCO: Miocene Climate Optimum; NAIP: North Atlantic Igneous Province; OAE: oceanic anoxic event; OJP: Ontong Java plateau; PETM: Paleocene-Eocene Thermal Maximum; Pl-To: Pliensbachian-Toarcian boundary event; P-T: end-Permian extinction; T-J: end-Triassic extinction.

lessen the effect of surface alteration (Sprain et al., 2019). While these efforts aid in improving the accuracy of $^{40}Ar/^{39}Ar$ dates, increases in analytical precision have resulted from increasing the number of different aliquots from the same sample used to derive a weighted mean plateau age, densely bracketing samples with standards during irradiation (Sprain et al., 2019), and advances in mass spectrometry, including the use of multicollector mass spectrometers (Jicha et al., 2016). As will be discussed further below, the decades-long effort to reduce uncertainties resulting from neutron fluence monitors that act as age standards in $^{40}Ar/^{39}Ar$ geochronology (Kuiper et al., 2008; Renne et al., 1998b, 2010, 2011), as well as efforts to better quantify decay constants (Min et al., 2000; Renne et al., 2010, 2011), have also helped to advance the accuracy and precision of dates.

U-Pb geochronology has been applied to three different U-bearing accessory minerals in pursuit of dating LIPs: baddeleyite, perovskite, and zircon. Baddeleyite has proven useful for dating diabase dikes and gabbros as well as hydrothermal contact aureoles (Fraser et al., 2004; Heaman & LeCheminant, 1993; Kamo et al., 1989; Söderlund et al., 2103), but can be prone to Pb-loss (e.g., Rioux et al., 2010). Perovskite has also been utilized to date LIPs, but >50% of the Pb in the mineral can be "common" Pb, not derived from radioactive decay, making the accuracy of perovskite dates accordingly sensitive to the chosen isotopic composition of common Pb (Burgess & Bowring, 2015; Kamo et al., 2003). Zircon lacks common Pb, but is rarely saturated and crystallized in LIP basalts. However, it has been dated from coarse-grained intrusions (sills and/or dikes) and thick lava flows (Blackburn et al., 2013; Burgess & Bowring, 2015; Davies et al., 2017; Dunning & Hodych, 1990; Kamo et al., 1996; Krogh et al., 1987; Schoene et al., 2010; Svensen et al., 2009, 2010), and from silicic ashes intercalated with LIP lava stratigraphy (Kasbohm & Schoene, 2018; Schoene et al., 2015, 2019). U-Pb dates are obtained through secondary ion mass spectrometry (SIMS), laser ablation inductively coupled plasma mass spectrometry (LA-ICPMS), and

Table 2.1 High-Precision Geochronology of LIPs

LIP	Formation(: Member) and/or Location	Lithology	Method	Mineral	Sample	Age	[X]	[Y]	[Z]	MSWD	n	Age interp.	Tracer/ Standard	Reference
Franklin LIP	intruding Wynniatt Formation	diabase sill	U-Pb	b	S8	716.33	0.54			0.6	5	WMA		Macdonald et al., 2010
Franklin LIP	Kikiktat Volcanics, Alaska	volcaniclastic	U-Pb	z	F624B	719.47	0.29			0.57		WMA	ET535	Cox et al., 2015
Kalkarindji LIP	Milliwindi	dolerite dike	U-Pb	z	Z01	510.67	0.17	0.30	0.62	2.0	5	WMA	ET2535	Jourdan et al., 2014
Emeishan LIP	Daheishan syenite	syenitic pluton	U-Pb	z	DHS-1	259.1	0.5			0.5	5	WMA	BGC	Shellnutt et al., 2012
Emeishan LIP	Woshui syenite	metaluminous syenite	U-Pb	z	GS05-067	259.6	0.5			1.5	6	WMA	BGC	Shellnutt et al., 2012
Emeishan LIP	Huangcao syenite	fayalite+quartz bearing syenite	U-Pb	z	GS05-059	258.9	0.7			0.7	5	WMA	BGC	Shellnutt et al., 2012
Emeishan LIP	Cida granite	granite	U-Pb	z	GS04-143	258.4	0.6			1.8	5	WMA	BGC	Shellnutt et al., 2012
Emeishan LIP	Dyke intruding Baima peralkaline syenite	mafic dyke	U-Pb	z	GS05-005	259.2	0.4			1.9	8	WMA	BGC	Shellnutt et al., 2012
Emeishan LIP	Dyke intruding Baima peralkaline syenite	mafic dyke	U-Pb	z	GS03-105	259.4	0.8			0.2	7	WMA	BGC	Shellnutt et al., 2012
Emeishan LIP	Dyke intruding Woshui syenite	mafic dyke	U-Pb	z	GS03-111	257.6	0.5			0.5	6	WMA	BGC	Shellnutt et al., 2012
Emeishan LIP	Binchuan section, subunit P2-5	felsic ignimbrite	U-Pb	z	JW-1	259.1	0.5			0.7	6	WMA	BGC	Zhong et al., 2014
Siberian Traps	Bratsk/Padunskii	sill	U-Pb	z	A10-23-1	251.681	0.063	0.091	0.28	1.2	8	WMA	ET2535	Burgess & Bowring, 2015
Siberian Traps	Bratsk/Padunskii	sill	U-Pb	z	A10-23-2	251.539	0.056	0.086	0.28	1.2	11	WMA	ET2535	Burgess & Bowring, 2015
Siberian Traps	Bratsk/Padunskii	sill	U-Pb	z	A10-23-3	251.460	0.051	0.083	0.28	1	12	WMA	ET2535	Burgess & Bowring, 2015
Siberian Traps	Nepa/lower sill/ Scholokhovskoie pipe	sill	U-Pb	z	194/35/ 860	251.354	0.088	0.110	0.29	0.4	4	WMA	ET2535	Burgess & Bowring, 2015

Table 2.1 (Continued)

Siberian Traps	Nepa/Scholokhovskoie pipe	sill	U-Pb	z	SHI-3085	251.501	0.071	0.097	0.29	0.34	10	WMA	ET2535	Burgess & Bowring, 2015
Siberian Traps	Lower Tungusskaya	sill	U-Pb	z	LT10-1-1	251.786	0.054	0.085	0.28	0.69	8	WMA	ET2535	Burgess & Bowring, 2015
Siberian Traps	Lower Tunguska	sill	U-Pb	z	LT10-2-2	251.795	0.070	0.096	0.29	1.3	14	WMA	ET2535	Burgess & Bowring, 2015
Siberian Traps	Lower Tunguska	sill	U-Pb	z	NT12-5-4	251.74	0.18	0.19	0.33	0.65	2	WMA	ET2535	Burgess & Bowring, 2015
Siberian Traps	Bratsk/Oktybroskoe deposit	sill	U-Pb	z	S68-700	251.509	0.044	0.079	0.28	1.4	13	WMA	ET2535	Burgess & Bowring, 2015
Siberian Traps	Bratsk/Oktybroskoe deposit	sill	U-Pb	z	O-6832	251.504	0.059	0.088	0.28	0.36	8	WMA	ET2535	Burgess & Bowring, 2015
Siberian Traps	Noril'sk/Kharaelakh	sill	U-Pb	z	KZ1818-1691	251.71	0.14	0.16	0.31	0.13	3	WMA	ET2535	Burgess & Bowring, 2015
Siberian Traps	Noril'sk/Talnakh	sill	U-Pb	z	KZ1799-1195	251.801	0.088	0.110	0.29	0.45	10	WMA	ET2535	Burgess & Bowring, 2015
Siberian Traps	Noril'sk/Chernogorsky	sill	U-Pb	z	R06-05	251.660	0.064	0.092	0.28	0.7	9	WMA	ET2535	Burgess & Bowring, 2015
Siberian Traps	Noril'sk/Noril'sk 1	sill	U-Pb	z	G22-105-2	251.64	0.10	0.12	0.30	0.48	11	WMA	ET2535	Burgess & Bowring, 2015
Siberian Traps	Noril'sk/Noril'sk 1	sill	U-Pb	z	G22-63-5	251.907	0.067	0.094	0.29	0.7	2	WMA	ET2535	Burgess & Bowring, 2015
Siberian Traps	Noril'sk/Noril'sk 1	sill	U-Pb	z	G22-65-0	251.813	0.065	0.092	0.28	1	5	WMA	ET2535	Burgess & Bowring, 2015
Siberian Traps	Daldykansky	sill	U-Pb	z	N12-3-2	251.376	0.050	0.082	0.28	1.1	7	WMA	ET2535	Burgess & Bowring, 2015
Siberian Traps	Maymecha-Kotuy	lava	U-Pb	ps	K08-14-3	252.20	0.12	0.16	0.31	1.1	15	WMA	ET2535	Burgess & Bowring, 2015

(*Continued*)

Table 2.1 (Continued)

LIP	Formation(: Member) and/or Location	Lithology	Method	Mineral	Sample	Age	[X]	[Y]	[Z]	MSWD	n	Age interp.	Tracer/ Standard	Reference
Siberian Traps	Maymecha-Kotuy	lava	U-Pb	ps	K09-6-1	252.27	0.11	0.15	0.31	1.1	12	WMA	ET2535	Burgess & Bowring, 2015
Siberian Traps	Maymecha-Kotuy	welded tuff	U-Pb	z	M09-11-1	251.901	0.061	0.089	0.28	1.6	21	WMA	ET2535	Burgess & Bowring, 2015
Siberian Traps	Maymecha-Kotuy	welded tuff	U-Pb	z	M09-12-1	251.483	0.088	0.110	0.29	1.1	7	WMA	ET2535	Burgess & Bowring, 2015
Siberian Traps	Angara river	pyroclastic breccia	U-Pb	z	A10-13-3	256.56	0.46	0.51	0.58		1	WMA	ET2535	Burgess & Bowring, 2015
Siberian Traps	Noril'sk	pyroclastic breccia	U-Pb	z	SG2610.4	255.58	0.38	0.43	0.51		1	YZ	ET2535	Burgess & Bowring, 2015
CAMP	North Mountain Basalt	Lava	U-Pb	z	NMB-03-1	201.38	0.02	0.22	0.31	1.2	20	WMA	ET535 or ET2535	Schoene et al., 2010
CAMP	North Mountain Basalt, Canada	Lava	U-Pb	z	AVC-1-2	201.522	0.064	1.4	1.4	0.71	8	WMA	ET2535	Blackburn et al., 2013
CAMP	North Mountain Basalt, Canada	pegmatite lens in lava	U-Pb	z	NMB_03	201.523	0.028	0.059	0.22	1.5	10	WMA	ET2535	Davies et al., 2017
CAMP	North Mountain Basalt, Canada	Lava (base of flow)	U-Pb	z	SU1201	201.440	0.047	0.71	0.23	3.5	13	WMA	ET2535	Davies et al., 2017
CAMP	Amelal Sill (Argana Basalt correlate), Morocco	Sill correlated as lava	U-Pb	z	MOR	201.564	0.054	0.075	0.23	0.93	10	WMA	ET2535	Blackburn et al., 2013
CAMP	Palisades Sill, New Jersey, USA	Sill correlated as lava	U-Pb	z	NB08-13	201.515	0.033	0.02	0.22	1.7	10	WMA	ET2535	Blackburn et al., 2013
CAMP	Butner Diabase, North Carolina, USA	Sill correlated as lava	U-Pb	z	Butner Diabase	200.916	0.064	0.075	0.23	1.5	14	WMA	ET2535	Blackburn et al., 2013
CAMP	Preakness Basalt, New Jersey, USA	Lava	U-Pb	z	NB08-12	201.274	0.032	0.062	0.22	0.71	15	WMA	ET2535	Blackburn et al., 2013
CAMP	York Haven Diabase, Pennsylvania, USA	Sill	U-Pb	z	YORK	201.509	0.035	0.063	0.22	0.77	6	WMA	ET2535	Blackburn et al., 2013
CAMP	Rapidan Sheet, Virgina, USA	Sill	U-Pb	z	030507-2	201.498	0.033	0.062	0.22	0.44	5	WMA	ET2535	Blackburn et al., 2013

Table 2.1 (Continued)

CAMP	Rossville Diabase, Pennsylvania, USA	Sill	U-Pb	z	ROSSGPH	201.305	0.034	0.063	0.22	1.4	6	WMA	ET2535	Blackburn et al., 2013
CAMP	Messejana dyke, Spain	dyke	U-Pb	z	MD48	201.585	0.034	0.063	0.22	2	8	WMA	ET2535	Davies et al., 2017
CAMP	Shelborne dyke, Canada	dyke	U-Pb	z	SD1_2	201.364	0.084	0.099	0.24	0.01	2	WMA	ET2535	Davies et al., 2017
CAMP	Foum Zguid dyke, Morocco	dyke	U-Pb	z	AN731	201.111	0.071	0.089	0.23	1.7	3	WMA	ET2535	Davies et al., 2017
CAMP	Hodh Sill, Mauritania	gabbro sill	U-Pb	z	HD38	201.440	0.031	0.061	0.22	4	7	WMA	ET2535	Davies et al., 2017
CAMP	Foura Djalon sill, Guinea	Sill	U-Pb	z	GUI22-26	201.493	0.051	0.073	0.23	1.5	8	WMA	ET2535	Davies et al., 2017
CAMP	Kakoulima intrusion, Guinea	Sill (layered ultramafic intrusion)	U-Pb	z	GUI126	201.635	0.029	0.06	0.22	1.8	16	WMA	ET2535	Davies et al., 2017
CAMP	Amazonia sill high Ti, Brazil	gabbro sill	U-Pb	z	RP113	201.364	0.023	0.057	0.22	1.88	9	WMA	ET2535	Davies et al., 2017
CAMP	Amazonia sill low Ti, Brazil	gabbro sill	U-Pb	z	RP126	201.525	0.065	0.076	0.23	1.2	9	WMA	ET2535	Davies et al., 2017
CAMP	Tarabuco sill, Bolivia	Sill	U-Pb	z	Bol	201.612	0.046	0.07	0.23	1.2	5	WMA	ET2535	Davies et al., 2017
CAMP	Amelal sill, Morocco	Sill	U-Pb	z	LV34	201.569	0.042			1.1	4	WMA	ET2535	Marzoli et al., 2019
CAMP	Solimões Basin, Brazil	Sill	U-Pb	z	Amostra 8	201.470	0.089	0.13	0.25	0.16	3	WMA-YF	ET535	Heimdal et al., 2018
CAMP	Amazonas Basin, Brazil	Sill	U-Pb	z	1-MA-1-PA-2883.18	201.477	0.062	0.11	0.24	1.7	5	WMA	ET535	Heimdal et al., 2018
Ferrar LIP	Storm Peak, Central Transantarctic Mountains (CTM)	uppermost lava	U-Pb	z	85-76-63	182.43	0.04	0.06	0.20	1.6	7	WMA	ET535 or ET2535	Burgess et al., 2015
Ferrar LIP	Mt. Bumstead, CTM	lowermost lava	U-Pb	z	96-55-2	182.48	0.20	0.21	0.28	0.81	3	WMA	ET535 or ET2535	Burgess et al., 2015
Ferrar LIP	Mt. Bumstead, CTM	uppermost lava	U-Pb	z	96-52-1	182.54	0.20	0.21	0.28	1	4	WMA	ET535 or ET2535	Burgess et al., 2015
Ferrar LIP	Nilsen Plateau, CTM	sill	U-Pb	z	96-65-11	182.59	0.08	0.093	0.22	0.94	6	WMA	ET535 or ET2535	Burgess et al., 2015
Ferrar LIP	Mt. Picciotto, CTM	sill A	U-Pb	z	85-4-18	182.633	0.049	0.069	0.21	1.3	9	WMA	ET535 or ET2535	Burgess et al., 2015
Ferrar LIP	Mt. Picciotto, CTM	sill B	U-Pb	z	85-4-4	182.616	0.049	0.068	0.21	0.47	4	WMA	ET535 or ET2535	Burgess et al., 2015
Ferrar LIP	Dawson Peak, CTM	sill	U-Pb	z	85-5-6	182.635	0.068	0.100	0.22	1.4	6	WMA	ET535 or ET2535	Burgess et al., 2015
Ferrar LIP	Wahl Glacier, CTM	sill	U-Pb	z	85-6-16	182.643	0.055	0.073	0.21	0.2	6	WMA	ET535 or ET2535	Burgess et al., 2015

(*Continued*)

Table 2.1 (Continued)

LIP	Formation(: Member) and/or Location	Lithology	Method	Mineral	Sample	Age	[X]	[Y]	[Z]	MSWD	n	Age interp.	Tracer/ Standard	Reference
Ferrar LIP	Roberts Massif, CTM	sill	U-Pb	z	96-74-6	182.746	0.054	0.072	0.21	0.7	7	WMA	ET535 or ET2535	Burgess et al., 2015
Ferrar LIP	Rougier Hill, CTM	sill	U-Pb	z	96-51-67	182.753	0.037	0.060	0.20	0.9	10	WMA	ET535 or ET2535	Burgess et al., 2015
Ferrar LIP	Mt. Falla, CTM	sill	U-Pb	z	90-63-6	182.779	0.033	0.061	0.20	0.98	14	WMA	ET535 or ET2535	Burgess et al., 2015
Ferrar LIP	Dawson Peak, CTM	sill	U-Pb	z	90-3-12	182.85	0.34	0.35	0.40	0.23	2	WMA	ET535 or ET2535	Burgess et al., 2015
Ferrar LIP	Brimstone Pea, South Victoria Land (SVL)	uppermost lava	U-Pb	z	97-55-1	182.635	0.077	0.090		0.9	4	WMA	ET535 or ET2535	Burgess et al., 2015
Ferrar LIP	Bull Pass, SVL	basement sill	U-Pb	z	05-06-01	182.680	0.038	0.061	0.20	0.84	8	WMA	ET535 or ET2535	Burgess et al., 2015
Ferrar LIP	Pandora Spire, SVL	Peneplain sill	U-Pb	z	A-236-A	182.689	0.038	0.061	0.20	0.87	6	WMA	ET535 or ET2535	Burgess et al., 2015
Ferrar LIP	Labyrinth Intrusion, SVL	intrusion	U-Pb	z	04-03-04	182.750	0.048	0.067	0.21	0.74	7	WMA	ET535 or ET2535	Burgess et al., 2015
Ferrar LIP	Pearse Valley, SVL	basement sill	U-Pb	z	90-76-13	182.776	0.059	0.098	0.22	0.78	6	WMA	ET535 or ET2535	Burgess et al., 2015
Ferrar LIP	Red Hill, Tasmania	sill	U-Pb	z	97-17	182.540	0.059	0.075	0.21	1.1	6	WMA	ET535 or ET2535	Burgess et al., 2015
Ferrar LIP	Forrestal granophyre, Dufek intrusion	Granophyre	U-Pb	z	PRR-8633	182.700	0.050	0.066	0.21	0.85	7	WMA	ET535 or ET2535	Burgess et al., 2015
Ferrar LIP	Lexington granophyre, Dufek intrusion	Granophyre	U-Pb	z	PRR-09305	182.629	0.029	0.056	0.20	1.3	11	WMA	ET535 or ET2535	Burgess et al., 2015
Karoo LIP	New Amalfi Sheet, South Africa	intrusion	U-Pb	z	I-247	182.246	0.045	0.066	0.21	0.74	5	WMA	ET535 or ET2535	Burgess et al., 2015
Deccan Traps	Jawhar Fm (lower)	coarse grained gabbro veinlets	U-Pb	z	DEC13-30	66.296	+0.037 /-0.030	+0.042 /-0.038	+0.081 /-0.080			TPB	ET2535	Schoene et al., 2019
Deccan Traps	Thakurvadi Fm (lower-middle)	redbole	U-Pb	z	RBAB	66.225	+0.077 /-0.071	+0.078 /-0.075	+0.104 /-0.104			TPB	ET2535	Schoene et al., 2019
Deccan Traps	Thakurvadi Fm (middle)	redbole	U-Pb	z	RBAG	66.185	+0.061 /-0.056	+0.068 /-0.060	+0.094 /-0.093			TPB	ET2535	Schoene et al., 2019
Deccan Traps	Khandala Fm (uppermost)	redbole	U-Pb	z	RBBQ	66.161	+0.066 /-0.069	+0.070 /-0.073	+0.099 /-0.101			TPB	ET2535	Schoene et al., 2019
Deccan Traps	Bushe Fm (2m below Poladpur Fm)	redbole	U-Pb	z	RBBL	66.132	+0.069 /-0.058	+0.071 /-0.064	+0.100 /-0.096			TPB	ET2535	Schoene et al., 2019
Deccan Traps	Poladpur Fm (10 m above Bushe contact)	breccia fill redbole	U-Pb	z	RBBI	66.088	+0.032 /-0.026	+0.043 /-0.034	+0.081 /-0.077			TPB	ET2535	Schoene et al., 2019
Deccan Traps	Poladpur Fm (middle)	breccia fill redbole	U-Pb	z	RBBM	66.07	+0.031 /-0.028	+0.036 /-0.032	+0.077 /-0.078			TPB	ET2535	Schoene et al., 2019

Table 2.1 (Continued)

Deccan Traps	Poladpur Fm (middle)	breccia fill redbole	U-Pb	z	RBBR	66.055	+0.017 /-0.018	+0.026 /-0.024	+0.074 /-0.073		TPB	ET2535	Schoene et al., 2019
Deccan Traps	Poladpur Fm (middle)	redbole	U-Pb	z	RBBJ	66.052	+0.015 /-0.018	+0.023 /-0.023	+0.073 /-0.072		TPB	ET2535	Schoene et al., 2019
Deccan Traps	Poladpur Fm (upper)	redbole	U-Pb	z	RBBS	66.047	+0.017 /-0.020	+0.025 /-0.027	+0.073 /-0.073		TPB	ET2535	Schoene et al., 2019
Deccan Traps	Poladpur Fm (uppermost)	redbole	U-Pb	z	RBAW	66.044	+0.019 /-0.022	+0.026 /-0.028	+0.073 /-0.073		TPB	ET2535	Schoene et al., 2019
Deccan Traps	Poladpur Fm (uppermost)	redbole	U-Pb	z	RBX	66.039	+0.022 /-0.030	+0.027 /-0.029	+0.074 /-0.075		TPB	ET2535	Schoene et al., 2019
Deccan Traps	Ambenali Fm (lower)	breccia fill redbole	U-Pb	z	RBBH	65.926	+0.035 /-0.028	+0.045 /-0.036	+0.081 /-0.079		TPB	ET2535	Schoene et al., 2019
Deccan Traps	Ambenali Fm	breccia fill redbole	U-Pb	z	RBBF	65.92	+0.032 /-0.031	+0.039 /-0.040	+0.080 /-0.079		TPB	ET2535	Schoene et al., 2019
Deccan Traps	Ambenali Fm (middle)	redbole	U-Pb	z	RBB2	65.905	+0.033 /-0.033	+0.042 /-0.045	+0.082 /-0.082		TPB	ET2535	Schoene et al., 2019
Deccan Traps	Ambenali Fm (middle)	breccia fill redbole	U-Pb	z	RBAY	65.895	+0.032 /-0.030	+0.042 /-0.041	+0.082 /-0.081		TPB	ET2535	Schoene et al., 2019
Deccan Traps	Ambenali Fm (middle)	redbole	U-Pb	z	RBAO	65.889	+0.029 /-0.028	+0.041 /-0.043	+0.081 /-0.080		TPB	ET2535	Schoene et al., 2019
Deccan Traps	Ambenali Fm (middle)	redbole	U-Pb	z	RBAN	65.885	+0.027 /-0.029	+0.042 /-0.044	+0.081 /-0.082		TPB	ET2535	Schoene et al., 2019
Deccan Traps	Ambenali Fm (middle-upper)	redbole	U-Pb	z	RBP	65.879	+0.024 /-0.029	+0.045 /-0.053	+0.084 /-0.086		TPB	ET2535	Schoene et al., 2019
Deccan Traps	Ambenali Fm (upper)	redbole	U-Pb	z	RBO	65.875	+0.022 /-0.042	+0.047 /-0.057	+0.085 /-0.088		TPB	ET2535	Schoene et al., 2019
Deccan Traps	Mahableshwar Fm	redbole	U-Pb	z	RBE	65.631	+0.053 /-0.030	+0.059 /-0.037	+0.088 /-0.080		TPB	ET2535	Schoene et al., 2019
Deccan Traps	Mahableshwar Fm	redbole	U-Pb	z	RBF	65.62	+0.028 /-0.021	+0.033 /-0.029	+0.075 /-0.075		TPB	ET2535	Schoene et al., 2019
Deccan Traps	Mahableshwar Fm	greenbole	U-Pb	z	DEC13-09	65.614	+0.015 /-0.017	+0.024 /-0.025	+0.073 /-0.073		TPB	ET2535	Schoene et al., 2019
Deccan Traps	Mahableshwar Fm (middle-upper)	redbole	U-Pb	z	RBG	65.59	+0.026 /-0.027	+0.032 /-0.033	+0.077 /-0.075		TPB	ET2535	Schoene et al., 2019
Deccan Traps	Jawhar Fm	lava	$^{40}Ar/^{39}Ar$	pl	KAS15-2	66.234	0.168		0.186	38	WMA	FCs = 28.294; Renne et al., 2011	Sprain et al., 2019
Deccan Traps	Jawhar Fm	lava	$^{40}Ar/^{39}Ar$	pl	KAS15-3	66.413	0.134		0.158	45	WMA	FCs = 28.294; Renne et al., 2011	Sprain et al., 2019
Deccan Traps	Neral Fm	lava	$^{40}Ar/^{39}Ar$	pl	MG7	66.153	0.100		0.132	36	WMA	FCs = 28.294; Renne et al., 2011	Sprain et al., 2019

(*Continued*)

Table 2.1 (Continued)

LIP	Formation(: Member) and/or Location	Lithology	Method	Mineral	Sample	Age	[X]	[Y]	[Z]	MSWD	n	Age interp.	Tracer/ Standard	Reference
Deccan Traps	Thakurvadi Fm	lava	$^{40}Ar/^{39}Ar$	pl	BOR14-1	65.912	0.136		0.158		38	WMA	FCs = 28.294; Renne et al., 2011	Sprain et al., 2019
Deccan Traps	Bhimashankar Fm	lava	$^{40}Ar/^{39}Ar$	pl	KHK15-1	66.171	0.152		0.176		36	WMA	FCs = 28.294; Renne et al., 2011	Sprain et al., 2019
Deccan Traps	Khandala Fm	lava	$^{40}Ar/^{39}Ar$	pl	MAT14-6	66.105	0.204		0.224		53	WMA	FCs = 28.294; Renne et al., 2011	Sprain et al., 2019
Deccan Traps	Khandala Fm	lava	$^{40}Ar/^{39}Ar$	pl	MAT14-7	66.158	0.164		0.186		57	WMA	FCs = 28.294; Renne et al., 2011	Sprain et al., 2019
Deccan Traps	Bushe Fm	lava	$^{40}Ar/^{39}Ar$	pl	VER14-3 (pooled)	65.974	0.168		0.186		86	WMA	FCs = 28.294; Renne et al., 2011	Sprain et al., 2019
Deccan Traps	Bushe Fm	lava	$^{40}Ar/^{39}Ar$	pl	POL15-2	66.059	0.158		0.180		43	WMA	FCs = 28.294; Renne et al., 2011	Sprain et al., 2019
Deccan Traps	Poladpur Fm	lava	$^{40}Ar/^{39}Ar$	pl	KJA14-1	65.977	0.302		0.316		##	WMA	FCs = 28.294; Renne et al., 2011	Sprain et al., 2019
Deccan Traps	Poladpur Fm	lava	$^{40}Ar/^{39}Ar$	pl	KJA15-1 (pooled)	65.988	0.638		0.658		44	WMA	FCs = 28.294; Renne et al., 2011	Sprain et al., 2019
Deccan Traps	Poladpur Fm	lava	$^{40}Ar/^{39}Ar$	pl	KJA14-2 (pooled)	65.94	0.184		0.202		91	WMA	FCs = 28.294; Renne et al., 2011	Sprain et al., 2019
Deccan Traps	Poladpur Fm	lava	$^{40}Ar/^{39}Ar$	pl	POL15-1 (pooled)	66.112	0.308		0.324		72	WMA	FCs = 28.294; Renne et al., 2011	Sprain et al., 2019
Deccan Traps	Ambenali Fm	lava	$^{40}Ar/^{39}Ar$	pl	AMB14-4	65.968	0.496		0.508		28	WMA	FCs = 28.294; Renne et al., 2011	Sprain et al., 2019
Deccan Traps	Ambenali Fm	lava	$^{40}Ar/^{39}Ar$	pl	AMB14-5	65.733	0.362		0.376		50	WMA	FCs = 28.294; Renne et al., 2011	Sprain et al., 2019
Deccan Traps	Ambenali Fm	lava	$^{40}Ar/^{39}Ar$	pl	AMB15-1 (pooled)	65.667	0.208		0.228		50	WMA	FCs = 28.294; Renne et al., 2011	Sprain et al., 2019
Deccan Traps	Mahableshwar Fm	lava	$^{40}Ar/^{39}Ar$	pl	AMB14-13	65.521	0.130		0.156		65	WMA	FCs = 28.294; Renne et al., 2011	Sprain et al., 2019
Deccan Traps	Mahableshwar Fm	lava	$^{40}Ar/^{39}Ar$	pl	AMB14-14	65.466	0.200		0.220		40	WMA	FCs = 28.294; Renne et al., 2011	Sprain et al., 2019

Table 2.1 (Continued)

Deccan Traps	Mahableshwar Fm	lava	$^{40}Ar/^{39}Ar$	pl	PAN15-3	65.422	0.206		0.224		51	WMA	FCs = 28.294; Renne et al., 2011	Sprain et al., 2019
NAIP	Tardree Rhyolite (between Antrim Plateau Volcanics), UK	Rhyolite	U-Pb	z	Tardree forest	61.32	0.09			1.1	6	WMA	Oslo 205Pb-235U tracer	Ganerød et al., 2011
NAIP	Vøring margin sill, offshore Norway	Sill	U-Pb	z	Utgard Upper Sill	55.6	0.3	0.4			4	WMA	Oslo 235U-205Pb-202Pb tracer	Svensen et al., 2010
NAIP	Vøring margin sill, offshore Norway	Sill	U-Pb	z	Utgard Lower Sill	56.3	0.4	0.5			1	YZ	Oslo 235U-205Pb-202Pb tracer	Svensen et al., 2010
NAIP	Skaergaard Intrusion, lower zone b, East Greenland	gabbroic pegmatite sill	U-Pb	z	SK-218	55.960	0.018	0.031	0.064	1.4	7	WMA	ET535 or ET2535	Wotzlaw et al., 2012
NAIP	Skaergaard Intrusion, Basistoppen Sill, East Greenland	tholeiitic sill	U-Pb	z	BZN	55.895	0.018	0.031	0.064	0.51	8	WMA	ET535 or ET2535	Wotzlaw et al., 2012
NAIP	Skaergaard Intrusion, Sandwich Horizon, East Greenland	ferrodiorite sill	U-Pb	z	SH-428	55.838	0.019	0.032	0.064	0.1	5	WMA	ET535 or ET2535	Wotzlaw et al., 2012
CRBG	Steens Basalt	Tuff 1 in Main Scarp	$^{40}Ar/^{39}Ar$	a	TB-124	16.592		0.028				WMA	FCs = 28.02; Renne et al.,	Mahood & Benson, 2017
CRBG	Steens Basalt	Tuff 2 in Main Scarp	$^{40}Ar/^{39}Ar$	a	TB-125	16.606		0.034				WMA	FCs = 28.02; Renne et al.,	Mahood & Benson, 2017
CRBG	Steens Basalt	Tuff 3 in Main Scarp	$^{40}Ar/^{39}Ar$	pl	TB-128A	16.499		0.104				WMA	FCs = 28.02; Renne et al.,	Mahood & Benson, 2017
CRBG	Steens Basalt	Tuff 4 in Main Scarp	$^{40}Ar/^{39}Ar$	pl	TB-128B	16.490		0.090				WMA	FCs = 28.02; Renne et al.,	Mahood & Benson, 2017
CRBG	Steens Basalt	Ignimbrite in East Creek	$^{40}Ar/^{39}Ar$	pl	ML-316	16.513		0.120				WMA	FCs = 28.02; Renne et al.,	Mahood & Benson, 2017
CRBG	Steens Basalt	Tuff 5 in Main Scarp	$^{40}Ar/^{39}Ar$	pl	TB-129	16.495		0.048				WMA	FCs = 28.02; Renne et al.,	Mahood & Benson, 2017
CRBG	Steens Basalt	Tuff in Rosebriar Creek	$^{40}Ar/^{39}Ar$	pl	TB-382	16.532		0.046				WMA	FCs = 28.02; Renne et al., 1998	Mahood & Benson, 2017
CRBG	above Steens Basalt	Alkali rhyolite lava capping Main Scarp	$^{40}Ar/^{39}Ar$	s	TB-130	16.485		0.028				WMA	FCs = 28.02; Renne et al., 1998	Mahood & Benson, 2017

(*Continued*)

Table 2.1 (Continued)

LIP	Formation(: Member) and/or Location	Lithology	Method	Mineral	Sample	Age	[X]	[Y]	[Z]	MSWD	n	Age interp.	Tracer/ Standard	Reference
CRBG	above Steens Basalt	Tuff capping Steens Basalt in East Creek	$^{40}Ar/^{39}Ar$	pl	TB-397	16.474		0.042				WMA	FCs = 28.02; Renne et al., 1998	Mahood & Benson, 2017
CRBG	above Steens Basalt	Tuff in Cottonwood Creek	$^{40}Ar/^{39}Ar$	s	TB-103A	16.475		0.054				WMA	FCs = 28.02; Renne et al., 1998	Mahood & Benson, 2017
CRBG	above Steens Basalt	Tuff of Monument Basin	$^{40}Ar/^{39}Ar$	s	TB-101	16.479		0.042				WMA	FCs = 28.02; Renne et al., 1998	Mahood & Benson, 2017
CRBG	Steens Basalt: Lower Steens	Redbole	U-Pb	z	CRB1625	16.653	0.063	0.071	0.073		1	YZ	ET535	Kasbohm & Schoene, 2018
CRBG	Steens Basalt: Upper Steens	Redbole	U-Pb	z	CRB1624	16.589	0.031	0.032	0.037		1	YZ	ET535	Kasbohm & Schoene, 2018
CRBG	Imnaha Basalt	Lapilli tuff	U-Pb	z	CRB1586	16.572	0.018	0.018	0.026		1	YZ	ET2535	Kasbohm & Schoene, 2018
CRBG	Grande Ronde Basalt: Wapshilla Ridge (lower)	Redbole	U-Pb	z	CRB1634	16.288	0.039	0.043	0.046		1	YZ	ET535	Kasbohm & Schoene, 2018
CRBG	Grande Ronde Basalt: Meyer Ridge / Wapshilla Ridge (upper)	Redbole	U-Pb	z	CRB1556	16.254	0.034	0.037	0.041		1	YZ	ET535	Kasbohm & Schoene, 2018
CRBG	Grande Ronde Basalt: Meyer Ridge / Wapshilla Ridge (upper)	Redbole	U-Pb	z	CRB1519	16.210	0.043	0.044	0.047		1	YZ	ET2535	Kasbohm & Schoene, 2018
CRBG	Wanapum Basalt: Frenchman Springs / Grande Ronde Basalt: Sentinel Bluffs (Vantage Interbed)	Pumice clasts	U-Pb	z	CRB1533	16.066	0.040	0.040	0.043		1	YZ	ET2535	Kasbohm & Schoene, 2018
CRBG	Wanapum Basalt: Priest Rapids (Basalt of Rosalia) / Roza	Ash	U-Pb	z	CRB1506	15.895	0.019	0.020	0.026		1	YZ	ET535	Kasbohm & Schoene, 2018

Note: This table compiles individual high-precision ages of LIPs, with stratigraphic and geographic context, the method by which an age was obtained, statistical information required to report the appropriate uncertainty, and references to the original studies in which these ages were presented. For comprehensive summaries of high-quality $^{40}Ar/^{39}Ar$ geochronology from the CAMP and NAIP, readers are directed to Marzoli et al. (2018, 2019) and Wilkinson et al. (2017). All U-Pb studies included are U-Pb CA-ID-TIMS. Abbreviations for Mineral: a = anorthoclase, b = baddeleyite, pl = plagioclase, ps = perovskite, s = sanidine, z = zircon. Abbreviations for Age interpretation: WMA = weighted mean age; WMA-YF = weighted mean age of youngest few zircons; YZ = youngest zircon; TPB = triangular prior in Bayesian age model. Abbreviations for Tracer/Standard used: ET = EARTHTIME; FCs = Fish Canyon Sanidine; BGC = Berkeley Geochronology Center tracer.

Table 2.2 High-Precision Geochronology of Environmental Events

Event	Location	Formation	Lithology	Method	Mineral	Sample	Age	[X]	[Y]	[Z]	MSWD	n	Age interp.	Tracer/ Standard	Reference
Sturtian Glaciation	Tambien Group, Ethiopia	Upper Mariam Bohkahko Formation	tuffaceous siltstone	U-Pb	z	SAM-ET-03	719.68	0.56	0.64	1.0	0.54	3	WMA	ET535 or ET2535	Maclennan et al., 2018
Sturtian Glaciation	Tambien Group, Ethiopia	Upper Mariam Bohkahko Formation	tuffaceous siltstone	U-Pb	z	SAM-ET-04	719.68	0.46	0.54	0.94	1.3	8	WMA	ET535 or ET2535	Maclennan et al., 2018
Sturtian Glaciation	Tambien Group, Ethiopia	over contact betw Didikama & Matheos	crystal-rich tuff	U-Pb	z	T46-102_2Z	735.25	0.25	0.39	0.88	0.36	5	WMA	ET535 or ET2535	Maclennan et al., 2018
Sturtian Glaciation	Bald Hill, Coal Creek Inlier, Canada	Mount Harper Volcanic Complex	quartz-phyric rhyolite	U-Pb	z	F837B	717.43	0.14			0.8	7	WMA	ET535	Macdonald et al., 2010
Sturtian Glaciation	Tango Tarn, Coal Creek Inlier, Canada	Eagle Creek Fm	green/pink brecciated tuff	U-Pb	z	F840A	716.47	0.24			1.1	6	WMA	ET535	Macdonald et al., 2010
Sturtian Glaciation	SW inlier, Coal Creek Inlier, Canada	Mount Harper Volcanic Complex	welded rhyolitic tuff	U-Pb	z	15PM06	718.1	0.3	0.5	0.9	0.42	4	WMA	ET535	Macdonald et al., 2017
Sturtian Glaciation	SW inlier, Coal Creek Inlier, Canada	Mount Harper Volcanic Complex	welded rhyolitic tuff	U-Pb	z	15PM08	718.1	0.2	0.4	0.8	0.98	6	WMA	ET535	Macdonald et al., 2017
Sturtian Glaciation	Bald Hill, Coal Creek Inlier, Canada	Mount Harper Volcanic Complex	rhyolite flow	U-Pb	z	F837A	717.8	0.2	0.4	0.8	0.64	4	WMA	ET535	Macdonald et al., 2017
Sturtian Glaciation	Bald Hill, Coal Creek Inlier, Canada	Mount Harper Volcanic Complex	rhyolite flow	U-Pb	z	F837C	717.7	0.3	0.5	0.9	0.29	3	WMA	ET535	Macdonald et al., 2017
Sturtian Glaciation	Tango Tarn, Coal Creek Inlier, Canada	Eagle Creek Fm	green tuff in diamictite	U-Pb	z	F917-1	716.9	0.4	0.5	0.9	1.5	5	WMA	ET535	Macdonald et al., 2017
Sturtian Glaciation	Jabal Akhdar region, Oman Mtns	Ghubrah Formation	tuffaceous sandstone	U-Pb	z	WM 54	711.52	0.20	0.31	1.09	0.18	5	WMA	ET535?	Bowring et al., 2007
Early-Middle Cambrian Extinction	Shropshire, England	Upper Comley Sandstone Formation	bentonite	U-Pb	z	Comley ub	509.1	0.22	0.56	0.77	0.51	7	WMA	ET535	Harvey et al., 2011
Frasnian-Famennian bounday	Steinbruch Schmidt Quarry, Germany	Bed 36	bentonite	U-Pb	z	Bed 36 bentonite	372.36	0.053	0.11	0.41	1.47	8	WMA	ET2535	Percival et al., 2018
end-Guadalupian Extinction	Sutherland, Northern Cape Province, South Africa	Poortjie Member, Tekloof Formation, Beaufort Group	white tuff 3.5 m above basal sstn	U-Pb	z	K1202-B1	260.259	0.081	0.14	0.31	1.5	4	WMA-YF	ET535	Day et al., 2015
End-Permian Extinction	Meishan, China	Changhsing Formation, Bed 25; extinction onset	ash	U-Pb	z	Bed 25-MBE0203	251.941	0.037		0.28	1.3	16	WMA	ET2535	Burgess et al., 2014
End-Permian Extinction	Meishan, China	Yinkeng Formation, Bed 28; extinction end	ash	U-Pb	z	Bed 28-MBE0205	251.880	0.031		0.28	0.76	13	WMA	ET2535	Burgess et al., 2014

(*Continued*)

Table 2.2 (Continued)

Event	Location	Formation	Lithology	Method	Mineral	Sample	Age	[X]	[Y]	[Z]	MSWD	n	Age interp.	Tracer/ Standard	Reference
End-Triassic Extinction	Pucara Basin, North Peru	onset of δ13C excursion	ash	U-Pb	z	LM4-86	201.510	0.15				1	YZ; MCMC	ET2535	Schoene et al., 2010; Wotzlaw et al., 2014
OAE2 (beginning)	Yezo Group, Hokkaido, Japan	Saku Formation, Hakkin Member	bentonite (felsic tuff)	U-Pb	z	HK017	94.436	0.093		0.14	0.8	5	WMA-YF	ET2535	Du Vivier et al., 2015
OAE2 (next; beginning)	Yezo Group, Hokkaido, Japan	Saku Formation, Hakkin Member	bentonite (felsic tuff)	U-Pb	z	CT103	94.536	0.170		0.21	0.4	6	WMA-YF	ET2535	Du Vivier et al., 2015
OAE2 (end)	Yezo Group, Hokkaido, Japan	Saku Formation, Hakkin Member	bentonite (felsic tuff)	U-Pb	z	HK018	93.92	0.031		0.11	2	3	WMA-YF	ET2535	Du Vivier et al., 2015
K-Pg boundary	Kiowa Core, Denver Basin, USA	D1 sequence; 1 ft above boundary	ash	U-Pb	z	KJ10-04	66.019	0.024	0.038	0.08	0.94	5	WMA	ET535	Clyde et al., 2016
K-Pg boundary	Bowring Pit, Denver Basin, USA	D1 sequence; 1.5 ft below boundary	ash	U-Pb	z	KJ08-157	66.082	0.022	0.037	0.08	0.78	12	WMA	ET535	Clyde et al., 2016
K-Pg boundary	Bowring Pit, Denver Basin, USA	D1 sequence; 3.2 ft above boundary	ash	U-Pb	z	KJ04-70	65.889	0.027	0.044	0.083	1.1	11	WMA	ET535	Clyde et al., 2016
K-Pg boundary	Denver Basin, USA	D1 sequence	K-Pg boundary	U-Pb	z		66.021	0.024	0.039	0.081			interpolated age		Clyde et al., 2016
K-Pg boundary	Hell Creek, Montana, USA	Hell Creek Fm / Fort Union Formation	Iridium Coal layer	$^{40}Ar/^{39}Ar$	af	IrZ	66.052	0.016		0.086		730	pooled WMA	FCs = 28.294; Renne et al., 2011	Sprain et al., 2018
PETM	Longyearben, Spitsbergen, Norway	Frysjaodden Fm, mid-excursion	bentonite	U-Pb	z	SB01-1	55.785	0.034	0.066	0.086	0.88	5	WMA-YF	ET535	Charles et al., 2011

Note: This table compiles individual high-precision ages of global change events, with stratigraphic and geographic context, the method by which an age was obtained, statistical information required to report the appropriate uncertainty, and references to the original studies in which these ages were presented. All U-Pb studies included are U-Pb CA-ID-TIMS. Abbreviations for Mineral: a = anorthoclase, af = alkali feldspar, z = zircon. Abbreviations for Age interpretation: MCMC = Markov Chain Monte Carlo; WMA = weighted mean age; WMA-YF = weighted mean age of youngest few zircons; YZ = youngest zircon. Abbreviations for Tracer/Standard used: ET = EARTHTIME; FCs = Fish Canyon Sanidine.

isotope dilution–thermal ionization mass spectrometry (ID-TIMS). While SIMS and LA-ICPMS techniques are rapid and well suited to studies requiring high spatial resolution, both of these techniques yield dates with analytical precision on the order of 2%–3% (Schoene, 2014). Because LIP emplacement and potentially associated environmental effects occur on timescales between 10 and 100 ka, here we focus only on U-Pb data sets generated via ID-TIMS, which commonly yields precision on the order of 0.1%.

ID-TIMS has seen a number of methodological advancements that have improved the accuracy and precision of analyses while reducing sample size. Reduction of laboratory blank and improvements in mass spectrometry over decades has enabled routine dating of single zircon grains and even fractions of single grains (e.g., Davis et al., 2003; Krogh, 1973; Michard-Vitrac et al., 1977; Parrish, 1987; Schoene, 2014). A key development allowing for substantial improvement to the accuracy of zircon ages came with the introduction of the chemical abrasion (CA) protocol, which preferentially dissolves portions of zircon grains that have been affected by radiation damage, and thus are more prone to Pb-loss (Mattinson, 2005). The EARTHTIME initiative has pushed for enhanced interlaboratory calibration through the use of the (^{202}Pb-)^{205}Pb-^{233}U-^{235}U tracer solutions (Condon et al., 2015; McLean et al., 2015), as well as a detailed account of uncertainties that factor into each date generated, allowing for comparison with dates derived from other methods (Bowring et al., 2011; McLean et al., 2011; Schmitz & Schoene, 2007).

While improvements in accuracy and precision have allowed geochronologists to better assess the correlation between LIPs and environmental perturbations, these breakthroughs have illuminated further complications inherent in interpreting the accuracy of an unknown quantity: the age of the rock being dated. Once a *date* is obtained, by using mass spectrometry to solve radioactive decay equations for time, geological uncertainty must be addressed at every stage of data interpretation, ultimately yielding an *age*, an interpretation of that date in terms of geological processes (Schoene, 2014). Geological uncertainty may be reflected in macroscopic questions, such as how well the timing of an intrusive unit aligns with its corresponding extrusive unit, or in essential smaller-scale questions of how to deal with complex age populations, when high-precision techniques yield individual dates that do not overlap within analytical uncertainty (Davydov et al., 2010; Keller et al., 2018; Mundil et al., 2004; Ramezani et al., 2007; Schoene et al., 2010).

Interpreting pre-eruptive zircon growth in volcanic ashes provides an instructive example of addressing complex age populations and geological uncertainty in geochronological data. This interpretation is an important consideration, as zircon geochronology of volcanic ashes has yielded most of the age constraints for the environmental perturbations described in this paper and for some of the constraints on the timing of LIP eruptions (e.g., Burgess et al., 2014; Clyde et al., 2016; Kasbohm & Schoene, 2018; Maclennan et al., 2018). Zircon dates obtained for dikes and sills are understandably more reproducible because zircon saturates very late during crystallization of mafic magmas. However, detecting age dispersion among single crystals is not unique to U-Pb zircon geochronology; high-precision ^{40}Ar/^{39}Ar studies utilizing multicollector mass spectrometry are beginning to resolve complex age populations of single sanidine crystals (Andersen et al., 2017), and the ramifications of these new data sets have yet to be teased out. Below, we discuss how this geological uncertainty has been addressed in zircon geochronology in the past decade, as it has not yet been routinely dealt with in the ^{40}Ar/^{39}Ar community.

Many of the studies presented here use weighted means of several individual zircon dates to provide an age for an ash bed, yielding lower uncertainty than that obtained for individual measurements. Calculating a mean square of weighted deviates (MSWD), with an expected value of 1, can assess how well analytical uncertainty explains the observed dispersion of dates about the mean (Wendt & Carl, 1991). However, a weighted mean should be used when the analytical uncertainty of the data corresponds to the actual error. Given evidence for protracted zircon crystallization and incorporation of xenocrysts and antecrysts in magma chambers, ~100 ka or even 1 Ma before an ash is deposited (Charlier & Zellmer, 2000; Ramezani et al., 2007; Schmitt, 2011; Schoene et al., 2010), a weighted mean age may underrepresent the geologic uncertainty in the age of an ash. An alternative approach using the youngest zircon dated in a population as the age of the rock may be more tenable, as one may assume this youngest crystal most closely approximates the timing of eruption (Kasbohm & Schoene, 2018; Schoene et al., 2010). This approach minimizes age bias from pre-eruptive crystallization, though it assumes the youngest zircon in the rock was sampled, and yields a lower-precision age than a weighted mean approach. Its accuracy may be assessed by observing whether or not the youngest zircon ages young upward in a comprehensively dated stratigraphic section. Some U-Pb studies utilize a combination of these approaches, by presenting the weighted mean age of the youngest few grains of the sample, which overlap within analytical uncertainty (Day et al., 2015; Kasbohm & Schoene, 2018; Meyers et al., 2012; Du Vivier et al., 2015). Importantly, unless high-precision single analyses are obtained by the method, either U-Pb or ^{40}Ar/^{39}Ar, geologic scatter cannot be recognized and accuracy cannot be assessed to better than the approximate precision of a single analysis.

While geological uncertainty can complicate interpretation of geochronological data, geological or stratigraphic constraints have been used to improve the accuracy and precision of geochronology through statistical modeling. Bayesian statistical models have been used in combination with high-precision data to evaluate eruptive ages for samples based on the timing of crystallization of individual zircon grains leading up to eruption (Keller et al., 2018; Schoene et al., 2019). Additionally, several studies incorporate Markov Chain Monte Carlo sampling of numerous samples taken from a single stratigraphic sequence, inspired by the practices of the radiocarbon community (Buck et al., 1991; Haslett & Parnell, 2008). Stratigraphic position has been leveraged to refine the precision of groups of zircon ages using this technique (Guex et al., 2012; Keller et al., 2018; Meyers et al., 2012; Schoene et al., 2015, 2019; De Vleeschouwer & Parnell, 2014). The combination of using high-precision dates and robust statistical models can test whether age interpretations of individual ash beds themselves are permissible.

Although accuracy and precision have improved in recent decades for U-Pb and $^{40}Ar/^{39}Ar$ geochronology, systematic uncertainties remain in radioactive decay constants, isotope tracer composition for U-Pb analysis, and ages of fluence monitors used in $^{40}Ar/^{39}Ar$ geochronology. Indeed, an early observation that U-Pb and $^{40}Ar/^{39}Ar$ ages for the Siberian Traps were offset at the ~1% level considering analytical uncertainty alone led to greater efforts to report and propagate systematic uncertainties for both methods (Renne et al., 1998b; Schoene et al., 2006). This offset has largely been attributed to inaccuracy in the ^{40}K decay constants (Renne et al., 2010). Although the ^{238}U and ^{235}U decay constants are among the best characterized in geochronology, with 0.11% and 0.14% uncertainty, respectively (Jaffey et al., 1971), these estimates derive from a single set of measurements, leaving open the possibility that inaccuracies in one or both U decay constants may exist (Parsons-Davis et al., 2018; Schoene et al., 2006).

Perhaps the most important remaining source of systematic uncertainty for Cenozoic samples is the adopted age of neutron fluence monitors used in $^{40}Ar/^{39}Ar$ geochronology. These monitors, also known as reference materials or standards, are natural minerals whose prescribed ages directly influence the calculated ages of samples. A typical monitor used is the Fish Canyon Sanidine, for which most $^{40}Ar/^{39}Ar$ labs have adopted the age of either 28.201 or 28.294 Ma (Kuiper et al., 2008; Renne et al., 2010, 2011). However, the U-Pb date for zircons from the Fish Canyon tuff from which the sanidine is derived is 28.196 ± 0.038 Ma (youngest zircon from Wotzlaw et al., 2013), agreeing better with the younger Fish Canyon sanidine age estimate of Kuiper et al. (2008). Studies working to intercalibrate U-Pb, astrochronology, and $^{40}Ar/^{39}Ar$ geochronology have shown improved concordance of U-Pb with $^{40}Ar/^{39}Ar$ ages when using the 28.201 Ma age for the Fish Canyon Sanidine (Kuiper et al., 2008; Meyers et al., 2012). This source of uncertainty affects the ability to compare U-Pb to $^{40}Ar/^{39}Ar$ dates as well as discern the existence of pre-eruptive zircon crystallization but is irrelevant for comparing dates within the $^{40}Ar/^{39}Ar$ system, if the same age, standard, and decay constants are used.

2.1.2. Data Reporting

In the sections below and in Tables 2.1 and 2.2, all U-Pb zircon dates reported are $^{238}U/^{206}Pb$ dates, and all $^{40}Ar/^{39}Ar$ are reported with the fluence monitor standard age used. All age uncertainties are reported in this paper at 2σ or 95% confidence. When possible, the ages in the text and table are reported at multiple levels of uncertainty, conventionally defined as follows: [X], the internal or random uncertainty, suitable for intralab comparison and interlab comparison when the same tracer is used; [Y], the uncertainty in tracer calibration or the age of the reference material used, for comparisons between labs using different ages or tracer solutions; and [Z], the uncertainty including decay constant uncertainty, permitting comparison between different geochronological methods (Schoene, 2014). High-precision U-Pb dates are calibrated with an EARTHTIME tracer, unless otherwise indicated in the text or in Table 2.1. To facilitate comparison of high-precision geochronology to that obtained for environmental crises, we have plotted the relative timing of both events with corresponding uncertainties in Figure 2.2

Many of the data sets are plotted as probability density functions (see Figs. 2.3–2.7, 2.9, and 2.10) to display the range of dates obtained from a LIP by various approaches; for plotting purposes, the maximum probability of each data set included in these figures has been scaled to a probability of 1. It is important to note that none of these plots are meant to represent rates or pulses of magmatism; they simply are a way to display what dates have been produced from rocks sampled for comparison purposes. Determining eruptive or intrusive rates requires integration of geologic and stratigraphic data with geochronology (e.g., Siberian Traps, CAMP, Deccan, NAIP).

2.2. GEOCHRONOLOGY OF 12 PAIRS OF LIPS AND ENVIRONMENTAL CRISES

2.2.1. Franklin LIP and Sturtian Snowball Earth

The Neoproterozoic Franklin LIP consists of lava flows, dikes, and sills emplaced over 2.25 million km^2 stretching across northern Canada from Alaska to Greenland. As one of the largest dike swarms on Earth, it includes diabase dikes up to 20 m wide in mainland

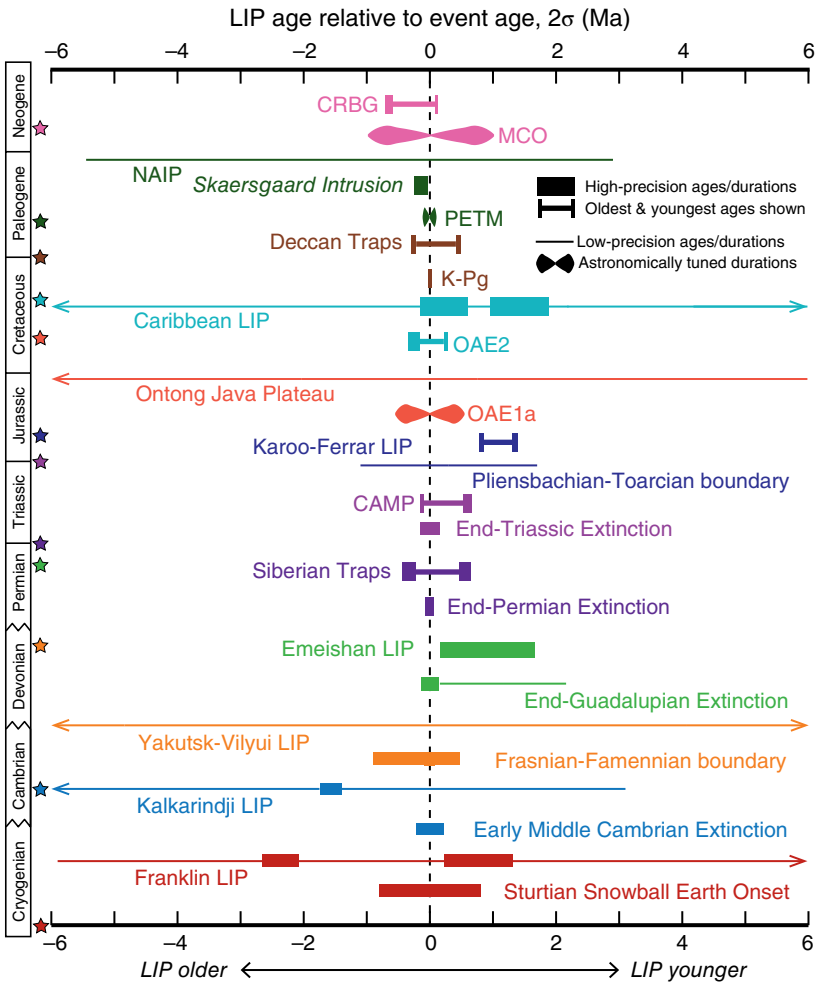

Figure 2.2 Relative timing of LIP eruptions and environmental events. This figure plots the timing and duration of each LIP, relative to that of the environmental event with which it is associated, plotted adjacently. For each couplet, 0 (black dashed line) is set at the most precise age constraint for the environmental change, or at the midpoint of the event's duration. Ages are plotted with 2σ analytical uncertainties [X], except for the end-Guadalupian constraint, shown with [Y] to reflect comparison with different tracers, and Yakutsk-Vilyui LIP/Frasnian-Famennian, which are shown with [Z] to compare $^{40}Ar/^{39}Ar$ and U-Pb results (arrows extending for the Yakutsk-Vilyui LIP indicate that the [Z] uncertainties extend beyond the bounds of the graph). The 0 line is removed for the Deccan Traps/K-Pg ages, since the high-precision extinction ages appear thinner than the line; U-Pb and $^{40}Ar/^{39}Ar$ calibrations are plotted separately to avoid inclusion of systematic uncertainties. Wide lines represent high-precision ages or durations, and thin lines represent low-precision ages. For populations shaped like an "I," the oldest and youngest ages in a data set are plotted with uncertainties, and there are a number of intervening high-precision ages between those bounds. The durations of OAE1a, the PETM, and the MCO have astronomical rather than radiometric age constraints, and so are demarcated with curved bars. CAMP: Central Atlantic Magmatic Province; CRBG: Columbia River Basalt Group; EMC: Early-Middle Cambrian extinction; F-F: Frasnian-Famennian extinction; end-G: end-Guadalupian extinction; K-Pg: end-Cretaceous extinction; MCO: Miocene Climate Optimum; NAIP: North Atlantic Igneous Province; OAE: oceanic anoxic event; OJP: Ontong Java plateau; PETM: Paleocene-Eocene Thermal Maximum; Pl-To: Pliensbachian-Toarcian boundary event; P-T: end-Permian extinction; T-J: end-Triassic extinction.

Canada, Baffin Island, and Greenland, with sills on Victoria Island, Northwest Territories, and Greenland (Denyszyn et al., 2009). The Natkusiak Volcanics of Victoria Island represent the thickest extrusive member of the Franklin LIP, with a maximum thickness of ~1,100 m (Cox et al., 2015).

Baddeleyite U-Pb ID-TIMS ages from Franklin dikes in Ellesmere Island, Devon Island, and Greenland indicate that the swarm was emplaced from 721 ± 2 Ma to 712 ± 2 Ma (Denyszyn et al., 2009). More recent work has yielded a baddeleyite date for a diabase sill from the Minto Inlier on Victoria Island of 716.33 ± 0.54 Ma

(Macdonald et al., 2010), and a U-Pb CA-ID-TIMS detrital zircon date of 719.47 ± 0.29 Ma for a volcaniclastic unit in the Kikiktat Volcanics in Arctic Alaska, which are interpreted to be connected to the Franklin LIP on the basis of this age overlap, proximity in paleogeography, and petrogenetic similarities (Cox et al., 2015). These dates from the Franklin LIP have been noted for their general synchronicity with the onset of the Sturtian Snowball Earth event, a period of global glaciation preceded by a large negative excursion in $\delta^{13}C$ (Macdonald et al., 2010). The cooling that potentially caused the runaway ice albedo feedback, allowing for these conditions, is hypothesized to be connected to the emplacement of the Franklin LIP (Macdonald et al., 2010). In this model, the equatorial paleolatitude for the Franklin LIP would have maximized CO_2 drawdown through the silicate weathering feedback (Goddéris et al., 2003; Macdonald et al., 2010). Further, the emplacement of the Natkusiak sills into sulfur-rich evaporites of the Shaler Supergroup could have allowed for cooling through injection of sulfate aerosols into the stratosphere (Macdonald & Wordsworth, 2017).

Maclennan et al. (2018) present CA-ID-TIMS zircon ages for the onset of Sturtian glaciation from tuffs underlying the Negash Diamictite of the Tambien Group in Ethiopia at 719.68 ± 0.46 Ma and 719.68 ± 0.56 Ma, as well as a tuff 2 m above the preceding nadir in $\delta^{13}C$ at 735.25 ± 0.25 Ma. Assuming a constant sediment accumulation rate in the basin, they suggest that the base of the diamictite was deposited at 717.1 +0.7/-0.9 Ma. This estimate agrees well with findings from the Coal Creek Inlier in Yukon, Canada, where CA-ID-TIMS zircon dates bracket the onset of glaciation to between 717.43 ± 0.14 Ma and 716.9 ± 0.4 Ma (Macdonald et al., 2010, 2017). The previously mentioned sample from the Kikiktat Volcanics also underlies the Sturtian Hula Hula diamictite, providing another maximum age constraint for glaciation at 719.47 ± 0.29 Ma (Cox et al., 2015), while a volcaniclastic interval within the Ghubrah diamictite in the Huqf Supergroup of Oman provides a minimum age constraint of 711.5 ± 0.3 Ma (Bowring et al., 2007). Collectively, these results indicate a globally synchronous onset for the Sturtian glaciation at the several-million-year level (Maclennan et al., 2018).

High-precision geochronology indicates concurrent onset of the Sturtian glaciation and Franklin sill emplacement on Victoria Island (Fig. 2.2) (Macdonald et al., 2010), although baddeleyite dates suggest Franklin intrusions likely began a few million years earlier elsewhere in the province (Denyszyn et al., 2009). These age constraints leave open the possibility that weathering of the Franklin LIP could have contributed to the cooling climate prior to the Sturtian Snowball Earth (Youbi et al., Chapter 8 this volume), even if it may not have been the primary driver of the event (Park et al., Chapter 7 this volume).

Difficulties in sampling accessibility and preservation of the Franklin LIP result in a paucity of high-precision dates for the Franklin LIP relative to other, more accessible LIPs. While there is decent horizontal coverage across the regional breadth of the LIP, the lack of continuous preserved extrusive sections prohibit a comprehensive vertical sampling strategy, which would be the ideal way in which to assess eruption rates and durations in the province. To date, most ages have been generated from dikes and sills, which lack stratigraphic context and relative order, and it is thus unclear when the bulk of magmatism occurred (Macdonald et al., 2010). Additionally, the total volume emplaced by the Franklin LIP is unknown, which inhibits attempts to model climatic impact. While its equatorial paleolatitude provides a useful condition for maximizing CO_2 drawdown through silicate weathering, this effect may not have been as significant if the volume of the LIP was small.

2.2.2. Kalkarindji LIP and Early-Middle Cambrian Extinction

The Kalkarindji LIP was emplaced in Australia, and is the oldest known Phanerozoic LIP (Glass & Phillips, 2006). Encompassing the Antrim Plateau Volcanics and Table Hill Volcanics, among other units found to have similar geochemistry, the Kalkarindji is characterized by tholeiitic basalt to basaltic andesite dikes, sills, and lava flows emplaced over 2.1 million km^2 across northern and central Australia (Evins et al., 2009), with a minimum estimated volume of 500,000 km^3 (Glass & Phillips, 2006). Individual lava flows range from 20 to 200 m, and the thickest stratigraphic sections of the province expose a cumulative thickness of 1,500 m (Jourdan et al., 2014). However, limited exposure prevents the development of robust stratigraphic division of the province.

U-Pb CA-ID-TIMS and $^{40}Ar/^{39}Ar$ dates from distant regions of the Kalkarindji yield ages overlapping at 511 Ma (Jourdan et al., 2014). Zircons extracted from the Milliwindi dolerite dike in the northern portion of the province were dated through CA-ID-TIMS, and yielded a weighted mean age of 510.67 ± 0.62 Ma ([Z]; MSWD = 2.0, n = 5). Baddeleyites extracted from mafic enclaves, the product of Kalkarindji sills intruding basement rock in the Munro well, were dated with TIMS and yielded a concordant upper intercept crystallization age of 511 ± 5 Ma (MSWD = 1.6). Plagioclase from dolerite sills in the Table Hill Volcanics, in the southern extent of the province, was dated via $^{40}Ar/^{39}Ar$ to 510 ± 4 Ma (MSWD = 0.74); pyroxene extracted from the same sills has been dated with $^{40}Ar/^{39}Ar$ to 506.28 ± 3.40 Ma ([X]; MSWD = 0.64) (Ware & Jourdan, 2018). Most of these ages agree

within uncertainty, obscuring the relative order of emplacement of these units and tentatively suggesting relatively brief emplacement of the province (Jourdan et al., 2014).

The Early-Middle Cambrian (EMC; Series 2-3, Stage 4-5) extinction is the first significant extinction following the Cambrian explosion, with more than 45% of genera going extinct (Jourdan et al., 2014). Reef-building archaeocyaths and a variety of reef-dwelling organisms, including many trilobites suffered most prominently (Zhuravlev & Wood, 1996). The period is marked by oceanic anoxia, a positive excursion in $\delta^{34}S$ (Hough et al., 2006), a negative excursion in $\delta^{13}C$ (Gozalo et al., 2013), and sea-level fall recognized as the Hawke Bay regression, hypothesized to be caused by uplift resulting from a mantle plume (Williams & Gostin, 2000).

The age of the EMC extinction has been bracketed by ID-TIMS U-Pb zircon geochronology on air-abraded zircons from three different ash beds in the Somerset Street Member of the Hanford Brook Formation of New Brunswick, Canada, in the Cambrian Series 2, Stage 4, and dated with ID-TIMS (Landing et al., 1998). The youngest grains from each of these samples were all ~511 Ma, thus the authors prefer a date of 511 ± 1 Ma for the stratigraphic unit, which can be interpreted as a maximum age, though this date should be treated with caution as it was acquired before chemical abrasion was introduced to ID-TIMS (Mattinson, 2005), and without the use of the EARTHTIME spike (Condon et al., 2015). More recently, Harvey et al. (2011) performed CA-ID-TIMS zircon geochronology on an ash bed at the base of the Upper Comley Sandstone Formation in Shropshire, England, in the Cambrian Series 3, Stage 5. The ash was dated to 509.10 ± 0.22/0.56/0.77 Ma, yielding a minimum age for the EMC extinction.

The temporal connection between the eruption of the Kalkarindji LIP and the EMC extinction was noted by Glass and Phillips (2006), and strengthened by the most recent high-precision geochronology of both the LIP and extinction (Harvey et al., 2011; Jourdan et al., 2014). The precise minimum age of the EMC from Harvey et al. (2011) overlaps with the baddeleyite and $^{40}Ar/^{39}Ar$ dates of Jourdan et al., (2014), though it postdates the zircon age obtained by Landing et al. (1998) by 1 Ma. This proximity in time, combined with analysis of volcanic breccias noting the explosive nature of some of the Kalkarindji volcanism, and sulfur concentration measurements from <50 to 1,900 μg/g, leads to the suggestion that the Kalkarindji LIP played a causative role in the EMC extinction (Jourdan et al., 2014).

While there is strong evidence suggesting a temporal correlation between these two events, the resolution of the geochronology cannot discern the relative order of the extinction versus volcanism (Marshall et al., Chapter 19 this volume). There is a paucity of high-precision geochronology samples, which are from disparate regions (i.e., not from a single vertical section). Because all current dates overlap, the duration of Kalkarindji eruptions cannot yet be constrained other than by estimation of maximum and minimum durations based upon the uncertainty on these dates. The limited surface exposure of the LIP also inhibits calculation of volume estimates for the province.

2.2.3. Yakutsk-Vilyui LIP and Frasnian-Famennian (Late Devonian) Mass Extinction

The Yakutsk-Vilyui LIP was emplaced on the northeastern Siberian platform in a triple junction rift system associated with the Late Devonian breakup of the eastern margin of Siberia. Dikes, lava flows, sills, and layered basalt breccia, with some intercalated ashes and tuffs, are found in outcrops on the Lena, Markha, and Viluy Rivers (Ricci et al., 2013). The Viluy rift, the NE/SW-striking branch of the triple junction, is 800 km long and 450 km wide and is bounded by parallel dike swarms on either side that are 700 km in length (Ricci et al., 2013). There is a wide range in estimates for the volume of the Yakutsk-Vilyui LIP. Polyansky et al. (2017) tally the total length of middle Paleozoic mafic dikes in the region, multiplied by thicknesses of 50–250 m, in addition to the volume of basalts and sills calculated from borehole and surface exposure, to estimate a minimum volume for the province of 100,000–215,000 km^3. Meanwhile, others estimate that over 300,000 km^3 erupted from the Viluy rift; if similar volumes were erupted from the other branches of the triple junction, the total volume emplaced by the Yakutsk-Vilyui LIP may have been up to 1 million km^3 (Ricci et al., 2013). The uncertainty in volume estimates may arise from the fact that exposure of the Yakutsk-Vilyui LIP is currently limited due to erosion, the overlying Siberian Traps LIP to the west, and thick Mesozoic sedimentary cover to the east (Ricci et al., 2013).

While there is a lack of high-precision geochronology for the Yakutsk-Vilyui LIP relative to other LIPs, $^{40}Ar/^{39}Ar$ work by Courtillot et al. (2010) provides $^{40}Ar/^{39}Ar$ plateau ages of 372.46 ± 1.4 Ma and 362.36 ± 1.8 Ma (2σ analytical uncertainties, recalculated with FCs = 28.201 Ma; Kuiper et al., 2008). Incorporating these results with other new dates from plagioclase phenocrysts separated from sills and lava flows, Ricci et al. (2013) also identify two separate $^{40}Ar/^{39}Ar$ age groups, at 366.6 ± 3.4 and 379.0 ± 3.4 Ma (2σ total error, recalculated with FCs = 28.201 Ma; Kuiper et al., 2008), although individual ages in each of these groups overlap with individual ages from the other group at the 2σ level.

The Frasnian-Famennian mass extinction, as one of the "Big Five" mass extinctions of the Phanerozoic,

resulted in the disappearance of >75% of marine species, particularly affecting reef systems, stromatoporoids, and benthic and planktonic marine invertebrates. The extinction took place in five pulses over a few Ma in the late Frasnian through early Famennian (McGhee, 2013). After the extinction began, there were two episodes of marine anoxia, known as the Kellwasser events, in the Upper Famennian, and a positive carbon isotope excursion (Joachimski et al., 2002; Joachimski & Buggisch, 1993). Hypotheses for the causal mechanism of the extinction include fluctuating sea level, bolide impact, the development of terrestrial plants (Algeo & Scheckler, 1998), and massive volcanism of the Yakutsk-Vilyui LIP (Racki, 1998; Ricci et al., 2013).

A bentonite horizon in uppermost Frasnian sediments in Steinbruch Schmidt, Germany, located 2.5 m below the Frasnian-Famennian boundary and between the Upper and Lower Kellwasser events, was dated with U-Pb ID-TIMS zircon geochronology to 377.2 ± 1.7 Ma; interpolating between this date and other ID-TIMS ages in the late Famennian led to an estimate of 376.1 ± 1.7 Ma for the Frasnian-Famennian boundary (Kaufmann et al., 2004). However, this date was found to be inconsistent with a Re-Os study that dated the Frasnian-Famennian boundary to 372.4 ± 3.8 Ma (Turgeon et al., 2007) and with a Monte Carlo analysis used in the most recent Geologic Time Scale, which placed the boundary at 372.2 ± 1.6 Ma (Becker et al., 2012). Following this disagreement, Percival et al. (2018) restudied the Steinbruch Schmidt bentonite with modern chemical abrasion U-Pb ID-TIMS zircon geochronology, and obtained a date of 372.360 ± 0.053/0.11/0.41 Ma. This date overlaps with the Re-Os date and with statistically calibrated ages. The prior ID-TIMS date may be incorrect because it predates the introduction of the chemical abrasion technique (Mattinson, 2005), thereby leading to ambiguity in how to interpret a complicated age spectrum that may have resulted from unresolved Pb loss. Several of the younger single crystal dates in that study, interpreted there as having been affected by Pb loss, also overlap with the most recent CA-ID-TIMS date (Kaufmann et al., 2004).

Astronomical tuning of the Kellwasser horizons in a number of stratigraphic sections suggests a time interval of 400–450 ka between the Kellwasser horizons (De Vleeschouwer et al., 2017). With this estimate and assuming a constant sediment accumulation rate, Percival et al. (2018) place the Frasnian-Famennian boundary at 371.86 ± 0.08 Ma, which postdates the $^{40}Ar/^{39}Ar$ age for the Siljan impact crater in Sweden of 377 ± 2 Ma (Reimold et al., 2005).

Given the sparse dates and low precision for Yakutsk-Vilyui LIP geochronology, it is possible that volcanic eruptions were concurrent with the Frasnian-Famennian boundary, and the pulses of extinction before and after the boundary. Alternatively, future high-precision dating of the LIP may find that these events are unrelated. An enrichment of sedimentary Hg has been observed at or near the Frasnian-Famennian boundary in three different sedimentary records, indicating that, if Hg enrichment is a robust proxy-stratigraphic marker of active LIP volcanism (Percival et al., Chapter 11 et al.), there may have been ongoing Yakutsk-Vilyui LIP activity during the Upper Kellwasser horizon (Racki et al., 2018).

2.2.4. Emeishan LIP and End-Guadalupian (Late Permian) Mass Extinction

The Emeishan LIP represents one of the primary eruptions of continental flood basalts on Pangea during the Late Permian. Approximately 300,000 km^3 erupted over 250,000 km^2 of the Yangtze craton (southwest China and northern Vietnam) in eastern Pangea, at roughly equatorial latitude (Shellnutt, 2014). However, the current exposure of the Emeishan LIP likely does not reflect its original extent, as the region has undergone extensive postemplacement deformation due to the collision of the North China block and South China block during the Mesozoic, and the Indo-Eurasian collision during the Cenozoic (Shellnutt et al., 2012). The Emeishan LIP consists of flood basalts, layered mafic-ultramafic intrusions, and silicic plutonic rocks. Ultramafic (picritic) rocks are found in the lower half of the flood basalts, while silicic volcanic rocks (andesite, trachyte, rhyolite, ignimbrite) and basaltic andesites are found in the upper half. The thickness of the LIP ranges from 1 to 5 km in the west of the province to 0.2 to 2.6 km in the east, with an average thickness of 700 m (Shellnutt, 2014).

Geologic, paleontological, and paleomagnetic evidence suggest the Emeishan LIP erupted rapidly. In basalt sequences, few flows have weathered flow tops beneath overlying flows or sediments (Shellnutt, 2014). The majority of Emeishan units have been identified as normal polarity thought to represent a single chron, with a few upper units indicating a reversed polarity, leading to the assessment that the LIP erupted in ≤1–2 Ma (Ali et al., 2002; Zheng et al., 2010), corresponding to the Capit-N normal chron of the Geomagnetic Polarity Timescale (Henderson et al., 2012). The Emeishan LIP has also been the subject of numerous geochronological studies of volcanic and plutonic rocks, yielding more than 50 published $^{40}Ar/^{39}Ar$, U-Pb SHRIMP, U-Pb LA-ICP-MS, and U-Pb ID-TIMS ages, which range from the Capitanian (266 ± 5 Ma) through the early Triassic (246 ± 4 Ma) (Shellnutt et al., 2012) (Fig. 2.3). This seemingly long duration, in conflict with the brief duration suggested by paleomagnetic studies, likely arises from inaccurate geochronologic studies, low precision of analyses, and uncertainty regarding the relationship between volcanic and plutonic rocks. $^{40}Ar/^{39}Ar$ ages range from

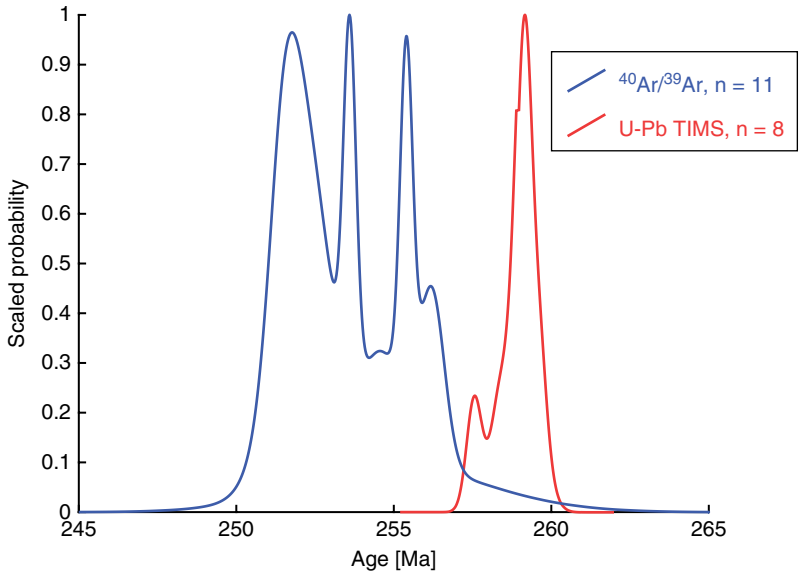

Figure 2.3 Geochronology of the Emeishan LIP, China. Probability density function for $^{40}Ar/^{39}Ar$ and U-Pb ID-TIMS geochronology obtained for the Emeishan LIP, as compiled by Shellnutt (2014).

256.2 ± 0.8 to 251.5 ± 0.9 Ma, suggesting that the Emeishan LIP emplacement extended past the Permian-Triassic boundary, concurrent with onset of Siberian Traps emplacement. Shellnut (2014) interprets these younger ages as erroneous, compromised by open system behavior resulting from postemplacement thermal resetting by regional tectonic events.

Recent high-precision U-Pb zircon CA-ID-TIMS dates have refined understanding of the timing and duration of Emeishan LIP emplacement (Chen & Xu, Chapter 18 this volume). Shellnutt et al. (2012) reported three ages from diabase dikes, ranging between 259.4 ± 0.8 Ma (MSWD = 0.2, n = 7) and 257.6 ± 0.5 Ma (MSWD = 0.5, n = 6), and from four granites between 259.6 ± 0.5 Ma (MSWD = 0.5, n = 5) and 258.4 ± 0.6 Ma (MSWD = 1.8, n = 5), indicating emplacement over ~2 Ma, consistent with age constraints from paleomagnetic data (Ali et al., 2002; Zheng et al., 2010). Shellnutt et al. (2012) also refuted the hypothesis that high-Ti rocks represented the waning phase of volcanism, as the high-Ti diabase dikes seem to have erupted throughout the duration of the Emeishan LIP. Additionally, Zhong et al. (2014) dated a felsic ignimbrite in the uppermost portion of the Emeishan LIP lavas with U-Pb CA-ID-TIMS, reporting 259.1 ± 0.5 Ma (MSWD = 0.7, n = 6) as the termination age for the Emeishan LIP. All of these dates were calibrated with a non-EARTHTIME tracer solution, but only reported analytical uncertainty [X]. Combined, these new data suggest that eruption of the Emeishan LIP may have lasted less than 1 Ma, and that volcanism ended more than 7 Ma before the Permian-Triassic boundary (Ramezani & Bowring, 2017).

The end-Guadalupian mass extinction affected both marine fauna and terrestrial flora and fauna, particularly affecting foraminifera, brachiopods, ammonoids, large bivalves, corals, and plants, though it was far less deadly than the Permian-Triassic mass extinction, which occurred only ~9 Ma later. It is also marked by fluctuations in seawater carbon isotopes and temperatures, and a major sea-level regression (Chen et al., 2011; Ramezani & Bowring, 2017). The age of this event has been constrained through CA-ID-TIMS geochronology in both marine and terrestrial sections. Mundil et al. (2004) dated ash beds in the marine Shangsi section in central China above the Guadalupian-Lopingian boundary to 259.1 ± 1.0 Ma (MSWD = 0.3, n = 6) and 260.8 ± 0.8 Ma (MSWD = 0.8, n = 5), providing a minimum age for the extinction, though obtained without the EARTHTIME tracer. On land, an ash bed in the lower Beaufort Group of the Karoo Basin in South Africa yielded a weighted mean age of 260.259 ± 0.081/0.14 Ma ([X/Y]; MSWD = 1.5, n = 4, EARTHTIME spike) for the top of the *Tapinocephalus* assemblage zone (Day et al., 2015). Between the *Tapinocephalus* assemblage zone and the following *Pristerognathus* assemblage zone, there is a 74%–80% loss of generic richness of all tetrapod fauna, particularly affecting the dinocephalian therapsids (Day et al., 2015).

Prior to publication of high-precision geochronology, the Emeishan LIP was implicated as a potential cause of, or contributor to, the end-Guadalupian mass extinction, as volcanic rocks were interbedded with Permian carbonates that exhibited the extinction (Wignall et al., 2009). The fact that the Emeishan LIP erupted through carbonate-rich sediments lends credence to this proposal, as the

emplacement would have allowed for the degassing of thousands of gigatons of CH_4 and 40,000 Gt of CO_2 (Shellnutt et al., 2012). Ganino and Arndt (2009) calculate that observed dolomite-to-marble host-rock thermal metamorphism would have produced 11–26 times more CO_2 than the degassing of magmatic CO_2 from the intrusion. $\delta^{18}O$ evidence for warming immediately before the Guadalupian-Lopingian boundary may reflect such an influx of CO_2 (Chen et al., 2011). The shorter duration of Emeishan emplacement proposed by Shellnutt et al. (2012) and Zhong et al. (2014) suggests a more intense pulse of degassing of the carbonate-rich country rock that could have caused greater disruption to the biosphere.

The differing levels of precision on ages for Emeishan LIP emplacement and that for the ashes bracketing the end-Guadalupian extinction complicate interpretation of the temporal connection between these events (Fig. 2.2). The most precise constraint on their coincidence is the maximum age of the end-Guadalupian extinction (Day et al., 2015), which suggests that extinction predates the Emeishan LIP (Shellnutt et al., 2012), though the LIP dates are an order of magnitude less precise. This allows for the absence or presence of a causal connection between Emeishan LIP magmatism and extinction. Uncertainties for Emeishan dates were not reported at the level to permit comparison of different tracers used [Y]; taking that systematic uncertainty into account would increase the uncertainty on each of the LIP dates, potentially allowing for greater overlap with the extinction constraint of Day et al. (2015). Some geochemical studies of end-Guadalupian sections from various sections globally indicate little climatic disturbance at the time (Sheldon et al., 2014) or a diagenetic, rather than environmentally controlled carbon isotope excursion (Jost et al., 2014), which complicates the simple hypothesis of the Emeishan LIP causing the end-Guadalupian extinction.

Alternatively, if the extinction occurred closer in time to the minimum, less precise age constraint of Mundil et al. (2004), it may suggest coincidence with Emeishan LIP eruptions. Because the Emeishan dates and that of Mundil et al. (2004) were obtained in the same laboratory with the same tracer solution, these results can be compared considering analytical uncertainty [X] alone. While the Emeishan intrusions described above seem to have been emplaced in ~2 Ma duration around 259 Ma, the difficulty in directly correlating these intrusions with extrusive units does not preclude lavas having been erupted over a different duration. Obtaining ages from lava flows has not yet been possible due to the lack of zircons in basalt flows and thermal resetting affecting $^{40}Ar/^{39}Ar$ geochronology (Shellnutt et al., 2012). Further, the uncertainty in eruptive duration as well as having only a minimum estimate for the volume of the LIP prohibit a robust calculation of effusion rate. Finally, obtaining high-precision dates from other sections capturing the end-Guadalupian extinction would aid in better assessing whether extinction was globally synchronous and contemporaneous with emplacement of the Emeishan LIP.

2.2.5. Siberian Traps LIP and End-Permian Extinction

The late Permian to early Triassic Siberian Traps LIP is the largest volume (~3 million km^3) Phanerozoic continental magmatic province (Burgess & Bowring, 2015) (Fig. 2.4). Following implication of the Siberian Traps as a potential trigger of the end-Permian mass extinction, efforts to date the timing of LIP emplacement focused primarily on the mineralized intrusions of the Noril'sk region, using the $^{40}Ar/^{39}Ar$ or U-Pb geochronometers (Baksi & Farrar, 1991; Campbell et al., 1992; Dalrymple et al., 1995; Kamo et al., 1996; Renne, 1995; Renne & Basu, 1991; Venkatesan et al., 1997). This work roughly constrained the timing of Siberian Traps emplacement from ~245 to 253 Ma (see review in Baksi, 2014). Subsequent $^{40}Ar/^{39}Ar$ on whole rock, plagioclase and biotite separates by Reichow et al. (2002, 2009) increased the overall footprint of Siberian Traps magmatism, and decreased the duration of magmatism to <2 Ma, with the volumetric bulk of emplacement centered around ~250 Ma. Kamo et al. (2003) corroborated this approximate age via U-Pb geochronology on baddeleyite and zircon, suggesting magmatism occurred over an even shorter interval of ~1 Ma, and began immediately prior to 251.7 ± 0.4 Ma (Fig. 2.4). A relatively short duration of "main phase" LIP magmatism is consistent with observations from other LIPs (see other sections of this chapter), however some $^{40}Ar/^{39}Ar$ and U-Pb (SIMS and TIMS) geochronology suggests multiple pulses of Siberian Traps emplacement, and contemporaneous granitic magmatism potentially related to the LIP occurring until ~20 Ma after emplacement of the main volume (Ivanov et al., 2009, 2013 and references therein; Malitch et al., 2012; Paton et al., 2010; Reichow et al., 2016).

Advances in U-Pb ID-TIMS geochronology permitted reinvestigation of the timing and duration of Siberian Traps emplacement, with a focus on resolving the tempo of main-phase magmatism; the relative timing of pyroclastic, intrusive, and effusive extrusive components of LIP emplacement; and the relative timing of LIP emplacement and the end-Permian mass extinction. Application of the U-Pb CA-ID-TIMS protocol to sills, lavas, and pyroclastic rocks from throughout the LIP by Burgess and Bowring, (2015) and Burgess et al. (2017) suggests emplacement of the volumetric majority of the Siberian Traps in three distinct stages, all of which occurred within ~1 Ma. In this framework, the Siberian Traps magmatic activity began just prior to 252.24 ± 0.10 Ma and was

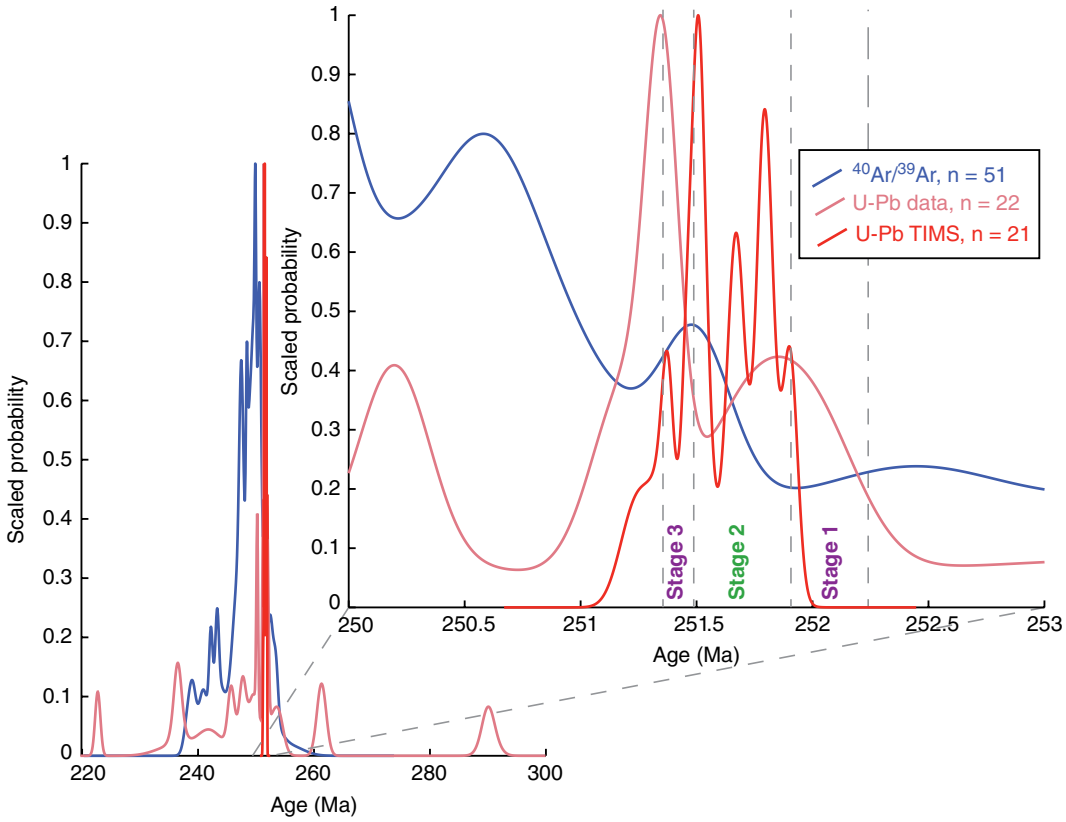

Figure 2.4 Geochronology of the Siberian Traps, Russia. Probability density function for $^{40}Ar/^{39}Ar$ and U-Pb ID-TIMS geochronology obtained for the Siberian Traps. U-Pb TIMS data from Burgess and Bowring (2015); sources for other data are Baksi and Farrar (1991); Basu et al. (1995); Campbell et al. (1992); Dalrymple et al. (1995); Ivanov et al. (2005, 2009, 2013); Kamo et al. (1996, 2003); Malitch et al. (2012, 2010); Paton et al. (2010); Reichow et al. (2002, 2009); Renne (1995); Renne and Basu (1991); Svensen et al. (2009); Venkatesan et al. (1997); Vernikovsky et al. (2003); Walderhaug et al. (2005). The different stages of emplacement from Burgess and Bowring (2015) and Burgess et al. (2017) are labeled.

characterized by initial pyroclastic eruptions followed by lava effusion. During this emplacement stage, ~2/3 of the total volume of the LIP was emplaced (>1 million km^3). Stage 2 began at 251.907 ± 0.067 Ma and was characterized by cessation of extrusion and the onset of widespread sill-complex formation. Intrusive magmatism continued throughout Stage 2 with no apparent hiatus (see also Svensen et al., 2009), with the close of Stage 2 at 251.483 ± 0.088 Ma. Extrusion of lavas resumed after a ~420 ka hiatus, marking the beginning of Stage 3, wherein both extrusive and intrusive magmatism continued until at least 251.354 ± 0.088 Ma, an age defined by the youngest sill dated in the province (Burgess et al., 2017; Burgess & Bowring, 2015). Estimates of this relatively rapid eruption tempo are supported by magnetic secular variation data, which suggest the early large-volume Siberian Traps lavas were emplaced in a few pulses, each lasting between 10 kyr and 100 kyr (Pavlov et al., 2019).

Temporal coincidence and thus a causal relationship between Siberian Traps LIP emplacement and the end-Permian mass extinction has long been postulated (e.g., Rampino & Stothers, 1988), and efforts to understand the timing and duration of extinction and recovery, and to weigh probable trigger and kill mechanisms have progressed concomitantly with advances in radiometric dating. Early work established a broad timeline for extinction, with the Permian-Triassic boundary at ~251 Ma (Bowring et al., 1998; Renne et al., 1995). Subsequent efforts utilizing both $^{40}Ar/^{39}Ar$ and U-Pb data sets result in varied placement of the extinction timing, ranging from ~249 to 253 Ma (Mundil et al., 2001, 2004; Reichow et al., 2009). Following the advent and broad adoption of the chemical abrasion protocol to single-grain zircon U-Pb TIMS geochronology, Shen et al. (2011) placed the P-T boundary at 252.17 ± 0.06 Ma, with an extinction duration of less than 200 kyr based on bracketing zircon U-Pb TIMS dates. Subsequent to this work, further advances in zircon U-Pb TIMS analysis and data reduction protocol (see review in supplement to Burgess et al., 2014) enabled an increase in both accuracy and precision, leading Burgess et al. (2014) to place the Permian-Triassic boundary at 251.902 ± 0.024 Ma, the onset of extinction just after

251.941 ± 0.037 Ma, and cessation prior to 251.880 ± 0.031 Ma, a maximum duration of ~60 kyr. This punctuated extinction interval is corroborated by astrochronologic timescales developed for the interval, which suggest extinction over a maximum of ~80 ka (Wu et al., 2013) or < 40 ka (Li et al., 2016). Employing similar methodology and protocol as Burgess et al. (2014), Baresel et al. (2017a) demonstrate synchrony of the Permian-Triassic boundary within the section dated by Burgess at al. (2014) and at two additional stratigraphic intervals in China, both characterized by much more rapid sediment accumulation rate prior to, and across the extinction interval. This synchrony permits Baresel et al., (2017b) to define a weighted mean Permian-Triassic boundary age of 251.959 ± 0.18 Ma for China, and to suggest that at the resolution of their geochronology (± ~40 ka), the extinction interval and timing of the Permian-Triassic boundary cannot be resolved from one another. Shen et al. (2018) utilize a similar dating protocol to date zircon from one of the two expanded stratigraphic intervals studied by Baresel et al. (2017a). Shen et al. (2018) place the Permian-Triassic boundary at 251.939 ± 0.031 Ma, and more tightly constrain the maximum duration of extinction to ~30 kyr.

As the geochronologic, paleontologic, and paleostratigraphic data sets linking emplacement of the Siberian Traps and the end-Permian extinction have become more accurate, comprehensive, and precise, the plausibility of a causal connection has been affirmed (see review in Burgess et al., 2014; 2017), and has moved far beyond broad temporal coincidence and an assumption of causality. The paleophysiologic selectivity of the extinction (see review in Knoll et al., 2007), evidence for widespread ocean anoxia and geographic selectivity of extinction (e.g., Cui et al., Chapter 14 this volume; Kendall et al., Chapter 13 this volume; Penn et al., 2018), and evidence for rapid global temperature increase (see Black et al., 2018; Bond & Sun, Chapter 3 this volume; Kiehl & Shields, 2005; Sun et al., 2012), all point toward a massive influx of greenhouse gas into the atmosphere system immediately preceding the onset of mass extinction. Currently, general consensus suggests Siberian Traps magmatism likely drove this rapid input of extinction-triggering greenhouse gasses via direct degassing from erupted lavas, and more importantly via metamorphism of sediments contacted by ascending and ponding magmas (e.g., Burgess et al., 2017; Chen & Xu, Chapter 18 this volume; Ganino & Arndt, 2009; Svensen et al., 2009). Using this mechanism and the geochronology and emplacement age model of Burgess and Bowring (2015), Burgess et al. (2017) propose that the initial pulse of Siberian Traps sill emplacement triggered the massive burst of greenhouse gases necessary to drive extinction. Because the ability of a LIP to drive massive environmental change is likely predicated on the tempo of magmatism, with faster emplacement rates more likely to overwhelm environmental buffering capacity, Burgess et al. (2017) suggest the initial pulse of sill emplacement led to sufficiently rapid gas generation. With conservative eruption rates of ~3–4 km^3/yr, emplacement of Siberian Traps lavas may also have played a key role in rapid greenhouse gas generation (Burgess & Bowring, 2015).

2.2.6. Central Atlantic Magmatic Province and End-Triassic Extinction

The Central Atlantic Magmatic Province (CAMP) was erupted and emplaced in association with the initial breakup of Pangea ca. 200 Ma, and has been implicated in the end-Triassic mass extinction event (Fig. 2.5). Due to its association with rifting, the CAMP was highly fragmented and distributed on numerous continents such that its extent and volume have been difficult to estimate (Marzoli et al., 1999; McHone, 2003). The exposed volume of the CAMP is likely <1 x 10^6 km^3, whereas estimates of the total original volume are >2–3 x 10^6 km^3 (Marzoli et al., 2018). Basaltic rocks of the CAMP have been identified in outcrop and drill core from North and South America, west Africa, and southern Europe. The chronology of the CAMP has been the subject of many studies over several decades, but here we focus on studies from the last ~20 y, for which numerous compilations exist. Because of this fragmented record of CAMP emplacement and eruption, it is hard to know how representative the geochronologic record is of the actual eruption and intrusion history, which is important when comparing emplacement timing to the end-Triassic mass extinction. Nonetheless, a combination of geochronological, geochemical and geological work has assembled a framework of global correlations for the magmatic history of the CAMP that serve geologic and biologic events. For example, observations of eruptive stratigraphic sections, where well exposed, record three main eruptive pulses of lavas separated by sedimentary horizons. These pulses are often unique geochemically, and can be correlated between isolated CAMP sections on different continents (Bertrand, 1991; Blackburn et al., 2013; Deenen et al., 2010; Marzoli et al., 2004, 2019; Olsen et al., 2003; Whiteside et al., 2007).

Modern geochronology for the CAMP includes both $^{40}Ar/^{39}Ar$ and U-Pb data. While hundreds of K-Ar and $^{40}Ar/^{39}Ar$ data exist, recent compilations have focused on the most reliable data, typically composed of handpicked plagioclase separates from both intrusive and extrusive units that cover the entirety of known CAMP stratigraphy (Marzoli et al., 2018, 2019). Recent compilations (Marzoli et al., 2018, 2019) contain ~90 step heating plateau dates, each typically with uncertainties of ± 1–2 Ma, that when plotted together range over ~10 Ma, from 204 to 192 Ma

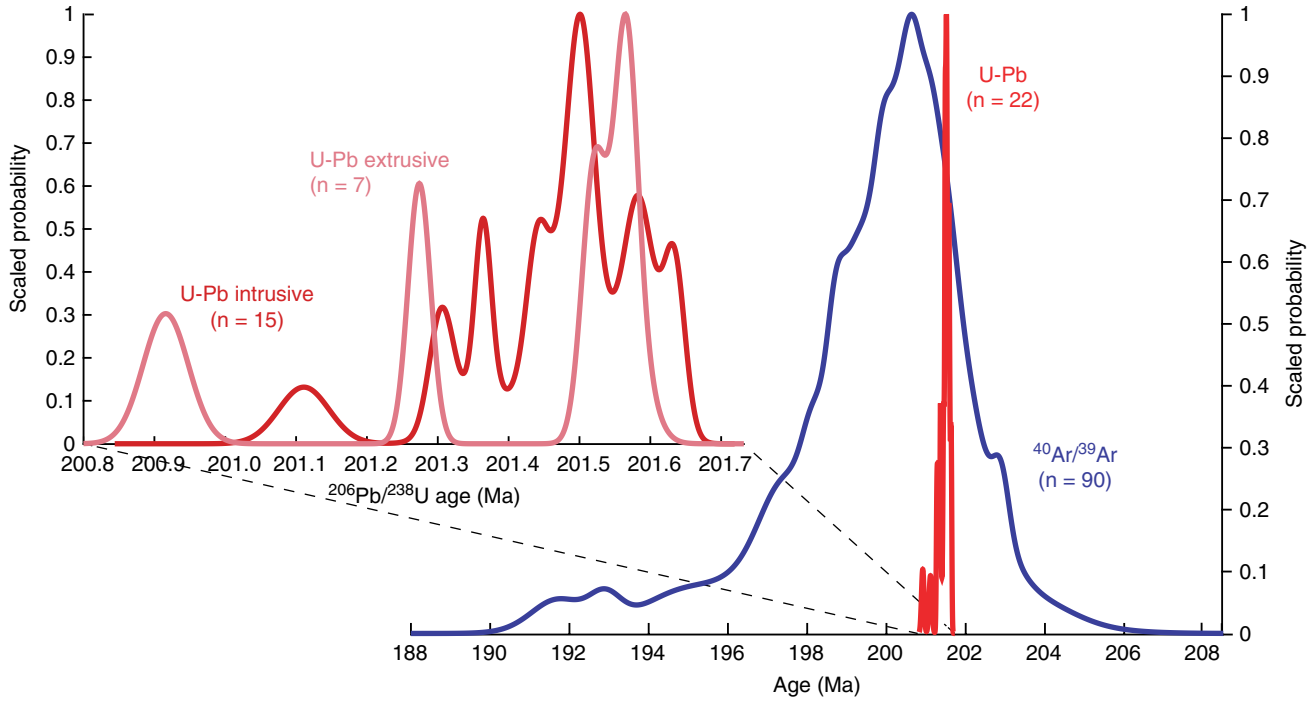

Figure 2.5 Geochronology of the Central Atlantic Magmatic Province (CAMP). Probability density function for $^{40}Ar/^{39}Ar$ and U-Pb ID-TIMS geochronology obtained for the CAMP, as compiled by Marzoli et al. (2018, 2019) with some additional data from Heimdal et al. (2018).

(Fig. 2.5). However most analyses fall within a briefer window of about 1–2 Ma centered around 200 Ma, relative to an age for the Fish Canyon Sanidine neutron fluence monitor from Kuiper et al. (2008) of 28.201 Ma (Jourdan et al., 2009; Knight et al., 2004; Marzoli et al., 2011, 2018, 2019; Nomade et al., 2007). These data form an asymmetric distribution with younger tails that generally correspond to lavas high in the stratigraphy in Morocco, but also include some intrusive rocks (Nomade et al., 2007).

U-Pb geochronology on the CAMP has been carried out primarily on sills and dikes that, because of slow cooling rate and internal differentiation, crystallized zircon (Blackburn et al., 2013; Davies et al., 2017; Dunning & Hodych, 1990; Heimdal et al., 2018; Krogh et al., 1987). However, several thick basaltic lava flows in North America that are also zircon bearing and dated with high precision (Blackburn et al., 2013; Davies et al., 2017; Schoene et al., 2010). A high precision baddeleyite date from the mafic Freetown Layered Complex, Sierra Leone, has been published but these data show large dispersion and are ca. 2 Ma younger than other U-Pb dates, perhaps indicating Pb loss (Callegaro et al., 2017). Other estimates for the timing of the main eruptions from CAMP flows in Morocco and North America are derived from correlating dated sills with flows geochemically (Blackburn et al., 2013). The U-Pb data, similar to the $^{40}Ar/^{39}Ar$ data, show that the CAMP erupted in <1 Ma. However, all the of the U-Pb dates produced so far fall from 201.6 to 200.9 Ma, with precision of ± 20–50 ka. In North American stratigraphic sections, younging upward is maintained and durations of hiatuses between the three main basalt formations are consistent with predictions from cyclostratigraphic analysis of sedimentary interbeds (Blackburn et al., 2013).

The apparent discrepancy in timescales derived from $^{40}Ar/^{39}Ar$ versus U-Pb geochronology likely derives from the relatively larger uncertainties associated with the reported $^{40}Ar/^{39}Ar$ dates. However, excess dispersion in the $^{40}Ar/^{39}Ar$ dates, demonstrated by high MSWDs on weighted means of culled data sets (Jourdan et al., 2009; Marzoli et al., 2018, 2019; Nomade et al., 2007), suggests that either the $^{40}Ar/^{39}Ar$ geochronology has dated rocks that have not been sampled by U-Pb geochronology, or that some $^{40}Ar/^{39}Ar$ dates were affected by open-system behavior, excess Ar, or Ar recoil. Given the larger data set obtained by $^{40}Ar/^{39}Ar$ geochronology, it is possible that younger dates represent a more prolonged lifetime of the CAMP than sampled by U-Pb geochronology. Most of the anomalously young dates (i.e., <198 Ma) are from older studies (Baksi & Archibald, 1997; Deckart et al., 1997; Marzoli et al., 1999; Verati et al., 2005) and have not been redated by U-Pb or $^{40}Ar/^{39}Ar$ geochronology for confirmation. Regardless, these younger dates, if accurate,

likely represent a volumetrically small portion of the CAMP, so it seems likely that the majority of the magmatism fell within a period of <1 Ma between ca. 201.6 and 200.9 Ma (Davies et al., 2017; Marzoli et al., 2018).

The CAMP is implicated in the end-Triassic mass extinction event, and geochronology has both supported and refined that assertion (Marzoli et al., 1999; Pálfy et al., 2000a; Schoene et al., 2010). The extinction event is recognized in both the terrestrial and marine biospheres (Tanner et al., 2004), although the position of the extinction interval is defined based on ammonite biostratigraphy (Guex et al., 2004; Von Hillebrandt et al., 2007). The extinction event has been dated by U-Pb zircon ID-TIMS geochronology in three locations: the Queen Charlotte Islands, western Canada; the Pucara Basin, Peru; and New York Canyon, Nevada, USA. The zircon data from the Queen Charlotte Islands location was complicated, and potentially affected by Pb loss, giving a weighted-mean date of 199.6 ± 0.3 Ma (2σ, [X])(Pálfy et al., 2000a). Data from the Pucara Basin represent the efforts of three studies, with more than a dozen zircon dates spanning the interval from the Norian-Rhaetian boundary to the Haetangian-Sinnemurian boundary (Guex et al., 2012; Schoene et al., 2010; Wotzlaw et al., 2014). The resulting age for the Triassic-Jurassic boundary is 201.36 ± 0.17 Ma, defined as the first occurrence of Jurassic ammonite *Psiloceras spelae*. The onset of the end-Triassic extinction is represented by the last occurrence of Triassic ammonite *Choristoceras crickmayi* and the onset of an initial carbon isotope excursion (Guex et al., 2004; Lindström et al., 2017), which is most closely stratigraphically associated with an ash bed dated at 201.51 ± 0.15 Ma (Schoene et al., 2010; Wotzlaw et al., 2014). These dates are corroborated by a single ash-bed date from Nevada that occurs near the Triassic-Jurassic boundary (Schoene et al., 2010). Another widely cited date for the Triassic-Jurassic extinction comes from the Newark basin, where a palynological turnover event occurs just below the lowermost CAMP basalt, the Orange Mountain Basalt (Whiteside et al., 2007). Using cyclostratigraphy to generate an age model below the basalt, Blackburn et al. (2013) calculate an age of 201.564 ± 0.015 Ma for the extinction event. However, whether or not the palynological event is representative of the global extinction event remains disputed (Cirilli et al., 2009), so we consider the date from the ammonite extinction record in Peru at 201.51 ± 0.15 Ma to be a more conservative and accurate date for the onset of the end-Triassic extinction.

The oldest high-precision U-Pb date of CAMP magmatism comes from an intrusion in west Africa, and is 201.635 ± 0.029 Ma (Davies et al., 2017), likely older than the date of the extinction event from Peru, and ca. 100 ka older than the date from the Newark Basin. In the Newark Basin, the oldest high-precision date from extrusive volcanism associated with the CAMP is that of the North Mountain Basalt and Orange Mountain Basalts (correlated geochemically with Palisades Sill) at 201.566 ± 0.031 / 201.481 ± 0.021 Ma (dates from Blackburn et al., 2013; Schoene et al., 2010) and 201.520 ± 0.034 Ma (Blackburn et al., 2013), respectively. The North Mountain Basalt was recently redated in Davies et al. (2017), and they adopt an age that averages existing data to get 201.498 ± 0.028 Ma. A date from the Amelal Sill in the Argana Basin in Morocco is 201.564 ± 0.054 Ma (Blackburn et al., 2013), which was placed within the intermediate lavas stratigraphically. Marzoli et al. (2019) report an additional date from the Amelal Sill of 201.569 ± 0.042 Ma, but correlate their sample with the stratigraphically lower lavas, implying rapid eruption for the lower and intermediate basalts in Morocco. Thus, it has become increasingly clear that the end-Triassic extinction coincides within tens of ka of the onset of extrusive CAMP volcanism in eastern North America and may postdate the beginning of sill emplacement by up to 100 ka. Underlining this observation is that the timescales of intrusive and extrusive magmas may not coincide (Fig. 2.5), although it is difficult to say at this point because high-precision dates on lavas are not very abundant. Understanding this record and continuing to search for older CAMP magmatic events will help tie down more precisely the timing of the onset of magmatism to the onset of extinction. Furthermore, higher-precision dates that can be tied closely to biostratigraphic and stable isotope data for the extinction interval itself will be key to understanding cause and effect in the end-Triassic biotic crisis (see Whiteside et al., Chapter 12 this volume).

2.2.7. Karoo-Ferrar LIP and Pliensbachian-Toarcian Boundary Event

The Karoo-Ferrar LIP is composed primarily of basaltic lavas, sills, and dikes, and was emplaced in the early Jurassic during breakup of Gondwana (e.g., Elliot, 2013; Elliot & Fleming, 2008; Fleming et al., 1997; Pálfy & Smith, 2000; Svensen et al., 2012). At present, the LIP extends over multiple continents, with the two primary portions of the LIP being the Karoo, which is found in South Africa, and the Ferrar, which crops out predominantly in Antarctica, with volumetrically subordinate intrusive rocks found in Australia, Tasmania, and New Zealand (Elliot & Fleming, 2004, 2008). Volume estimates for the entire province are on the order of 2.5 x 10^6 km^3 (Cox, 1988; Encarnación et al., 1996). This LIP has received considerable attention due to emplacement of the province in broad temporal coincidence with global environmental perturbations in the early Jurassic, near the Pliensbachian-Toarcian boundary (Pl-To), and the possibility that LIP magmatism triggered these

instabilities (e.g., Bergman et al., Chapter 9 this volume; Burgess et al., 2015; Huang & Hesselbo, 2014; Jourdan et al., 2008; Moulin et al., 2017; Sell et al., 2014; Suan et al., 2008; Svensen et al., 2012).

Early efforts to date Karoo-Ferrar magmatism suggested broad synchrony between emplacement of disparate portions of the LIP and a total emplacement duration of >10 Ma (see review in Burgess et al., 2015). For the Karoo, initial work was primarily done via the $^{40}Ar/^{39}Ar$ chronometer, with a total duration of sill and lava emplacement eventually constrained to ~3 Ma including uncertainty on dates (Duncan et al., 1997; Encarnación et al., 1996; Jourdan et al., 2005, 2007, 2008; Moulin et al., 2011). The idea of a protracted emplacement interval for the Karoo has subsequently been revised, with zircon U-Pb TIMS dates suggesting a much narrower emplacement interval of <0.5 Ma starting at ~182.7 Ma (Corfu et al., 2016; Svensen et al., 2012). Further U-Pb TIMS work on zircon and baddeleyite by Sell et al. (2014) indicate that Karoo intrusive magmatism progressed over 2 Ma, however there is some debate as to whether all of these rocks are associated with the main phase of Karoo LIP magmatism, and whether baddeleyite dates were affected by Pb loss (Corfu et al., 2016; Sell et al., 2016). Similarly, a protracted emplacement interval characterized by multiple, shorter-lived episodes of voluminous eruption is supported by K-Ar and $^{40}Ar/^{39}Ar$ work by Moulin et al. (2017). One U-Pb TIMS zircon date by Burgess et al. (2015) falls within the largest-volume pulse defined by Moulin et al. (2017), and is slightly older than, but within uncertainty of the older sample dated by Sell et al. (2014) and emplacement range defined by Svensen et al. (2015). At present, dates characterized by the highest analytical precision suggest emplacement of the Karoo over less than 1 Ma, while less precise but more stratigraphically inclusive K-Ar and $^{40}Ar/^{39}Ar$ dates suggest Karoo emplacement over nearly 10 Ma (Fig. 2.6).

For the Ferrar, initial dating efforts by U-Pb and $^{40}Ar/^{39}Ar$ chronometers constrained emplacement duration to between ~1 and 2 Ma (e.g., Duncan et al., 1997; Encarnación et al., 1996; Fleming et al., 1997; Foland et al., 1993; Heimann et al., 1994; Minor & Mukasa, 1997). Subsequent CA-ID-TIMS U-Pb zircon dates by Burgess et al. (2015) significantly decreased this range, suggesting emplacement over 349 ± 49 kyr, with magmatism starting by 182.779 ± 0.033 Ma and persisting until at least 182.430 ± 0.036 Ma. This duration is consistent

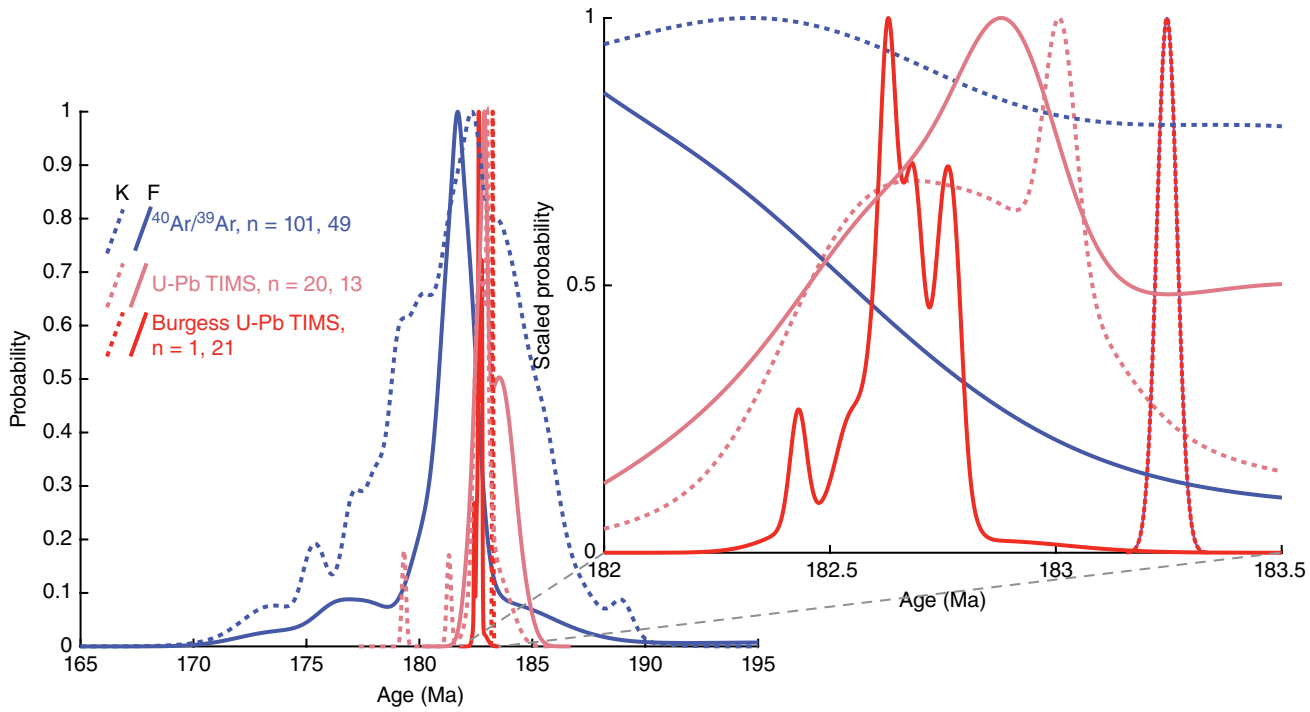

Figure 2.6 Geochronology of the Karoo-Ferrar LIP . Probability density function for $^{40}Ar/^{39}Ar$ and U-Pb ID-TIMS geochronology obtained for the Karoo-Ferrar LIP, highlighting high-precision U-Pb results of Burgess et al. (2017). Sources for other age data are Antonini (1998); Brewer et al. (1996); Duncan et al. (1997); Elliot et al. (1999); Encarnación et al. (1996); Fleming et al. (1997); Foland et al. (1993); Le Gall et al. (2002); Hargraves et al. (1997); Heimann et al. (1994); Ivanov et al. (2017); Jones et al. (2001); Jourdan et al. (2005, 2007, 2008); Minor and Mukasa (1997); Moulin et al. (2017); Riley et al. (2005); Sell et al. (2014); Svensen et al. (2012, 2015); Ware and Jourdan (2018).

with U-Pb ID-TIMS baddeleyite dating of Ferrar rocks from Tasmania by Ivanov et al. (2017), within the bounds of ^{40}Ar-^{39}Ar pyroxene and plagioclase geochronology on Tasmanian dolerites by Ware and Jourdan (2018), and falls within the bounds defined for the Karoo by Sell et al. (2014) and Svensen et al. (2012). Together, these data sets indicate broadly contemporaneous magmatism in what are now two geographically disparate Ferrar provinces. Extending this correlation with the Karoo requires temporal resolution beyond what currently exists for the Karoo. Estimates of average emplacement tempo for the Karoo-Ferrar are similarly precarious due to uncertainty on eruption duration and total province volume, as LIP erosion and concealment by Antarctic ice may bias volume estimates. Based on the range in eruption duration from the Karoo and Ferrar of between 10 Ma and 1 Ma, reasonable estimates for average eruption tempo range from 0.25 to 2.5 km^3/my, with the potential for short-lived (<100 ka) higher flux pulses within the broader LIP emplacement interval.

Broad coincidence between Karoo-Ferrar LIP emplacement and the Pl-To biotic crises and oceanic anoxic event (OAE) has been recognized for decades (e.g., Sepkoski, 1986). Recent work indicates multiple extinction events at this time, with the two most impactful events occurring coincident with the Pl-To boundary and in the early Toarcian (see review in Moulin et al., 2017). This time period is also characterized by multiple large amplitude excursions in the carbon isotope record, evidence for widespread ocean anoxia, global warming and cooling events, and fluctuations in sea level (e.g., Al-Suwaidi et al., 2010; Boulila et al., 2014; Guex et al., 2012; Huang & Hesselbo, 2014; Kendall et al., Chapter 13 this volume; Pálfy et al., 2002; Suan et al., 2008, 2011, and many others). Determining coincidence between Karoo-Ferrar LIP emplacement and environmental perturbations in the early Jurassic requires not only a stratigraphically comprehensive, accurate, and precise age model for LIP emplacement, but also on the Pl-To boundary date, and the timing and tempo of various environmental perturbations. The absolute temporal record of the LIP is in this instance more thoroughly characterized than geochronology of the environmental crises. Accepting the Pl-To boundary age from Pálfy et al. (2000b) of 183.6 +1.7/-1.1 Ma, which is consistent within uncertainty with constraints from Sell et al. (2014), Ferrar emplacement occurs within uncertainty of the boundary date and carbon cycle perturbation and is contemporaneous with the onset of the early Jurassic carbon isotope excursion, extinction, and ocean anoxia (Burgess et al., 2015). A more detailed temporal relationship between Ferrar emplacement and Toarcian perturbations is difficult to ascertain due to large uncertainty in the timing and tempo of these events (e.g., Boulila et al., 2014; Hesselbo et al., 2007; Hesselbo & Pienkowski, 2011). Age uncertainty on the timing and, importantly, tempo of Karoo eruption/emplacement is high relative to that on the Ferrar, which further exacerbates efforts to conclusively link emplacement with environmental perturbation. Recent geochronology efforts do not preclude coincidence, but additional high-precision geochronology with age uncertainty smaller than the duration of events being compared is required to make robust comparison.

2.2.8. Cretaceous Oceanic LIPs and Oceanic Anoxic Events

The Cretaceous is marked by the prevalence of oceanic LIP eruptions and oceanic anoxic events, which appear to be broadly correlative. OAEs were brief episodes of disturbance to the carbon cycle, with enhanced organic carbon burial, evidenced by the widespread deposition of black shales, and positive carbon isotope excursions of 1.5–2‰ (Jenkyns, 2010). They are associated with global warming, sea-level rise, and the drowning of carbonate platforms (Jenkyns, 2010). OAEs appear to have been concurrent with the eruptions of the Cretaceous oceanic flood basalts, which may have provided excess carbon to the ocean that allowed for greater marine productivity, and pCO_2 to the atmosphere, allowing for global warming that accelerated the hydrological cycle, increasing continental weathering and nutrient discharge to the ocean (Ogg et al., 2012). Greater productivity allowed for an increase in organic matter, which placed a greater demand for oxygen in the water column as it was buried, leading to widespread anoxia (Jenkyns, 2010) as the warm global climate did not allow for cold oxygenated bottom water (Schlanger & Jenkyns, 1976; see also Bergman et al., Chapter 9 this volume). Here we will focus on two of the largest Cretaceous oceanic LIPs, Ontong Java Plateau and the Caribbean LIP, because they are connected to the two most widespread OAEs, the Early Aptian OAE1a, and the Cenomanian-Turonian OAE2 (the Selli and Bonarelli events, named for their initial recognition in Italy).

Ontong Java Plateau and OAE1a

The Ontong Java Plateau (OJP) is the largest oceanic large igneous province and largest series of volcanic eruptions in the last 250 Ma, with an estimated volume of 60 million km^3 over an area of 2 million km^2 in the southwestern equatorial Pacific (Courtillot & Renne, 2003). The Greater OJP also includes the minor plateaus of Manahiki, Hikurangi, and South Kerguelen, and is exposed above sea level in the Solomon Islands Arc (Bergman et al., Chapter 9 this volume; Kerr, 2014), and the eastern portion of the plateau is thought to have been emplaced near or at sea level (Chambers et al., 2004).

Given its uniform normal polarity and biostratigraphy, the OJP is thought to have formed in the early Aptian, during the Cretaceous normal polarity superchron (Tarduno et al., 1991). All radioistopic geochronology in the OJP has been performed using the $^{40}Ar/^{39}Ar$ method, primarily on whole-rock samples. Mahoney et al. (1993) report that six whole-rock samples from ODP Site 807 yield eruption ages indistinguishable from one another, with a weighted mean value of 122.3 ± 2.0 Ma (range from 124.7 ± 4.4 Ma to 119.9 ± 5.2 Ma). Age results from Site 289, which was sampled 500 km away, and from the island of Malaita, over 1,600 km away, overlap with this mean value. Further dating from exposed OJP basement on the Solomon Islands yielded ages overlapping with the 122 Ma age group (Tejada et al., 1996, 2002). These early studies also had suggested a second pulse of volcanism at ~90 Ma, given ages obtained from ODP Site 803 (Mahoney et al., 1993) and the island of Sigana (Tejada et al., 1996). However, these younger ages are thought to be affected by argon recoil, given the low potassium content of the rocks and the few plateau heating steps used to obtain the ages, and thus should be interpreted as minimum ages (Chambers et al., 2002). Total fusion ages on plagioclase crystals extracted from OJP basalts sampled at ODP Site 1184, in the eastern salient of the plateau, yield a weighted mean age of 123.5 ± 3.6 Ma, overlapping with the age population obtained elsewhere in the plateau (Chambers et al., 2004).

Though these ages lack the precision of more recent $^{40}Ar/^{39}Ar$ and U-Pb studies on other LIPs, they do suggest that OJP volcanism was occurring simultaneously across a widespread area at ~122 Ma. It cannot yet be assessed whether volcanism occurred on the short timescale of other LIPs in <1 Ma, or if it occurred in the 9 Ma permitted by the range of dates, which would allow calculated emplacement rates to vary over an order of magnitude (Fitton & Godard, 2004). With the current data, there is no apparent geographic age progression, though this may be obscured by the precision of the ages and by the limitations of sampling over only 9 m–2 km of stratigraphy at a given sampling site (Tejada et al., 1996, 2002).

OAE1a, also known as the Selli event, is recognized for its apparent concurrence with the emplacement of the OJP in the early Aptian. It is marked by the deposition of organic-rich black shales in all major ocean basins, and a complex geochemical signature in $\delta^{13}C$, with a negative excursion followed by a major positive excursion (Menegatti et al., 1998). The influx of light carbon causing the negative excursion is thought to result from injection of CO_2 from submarine volcanic outgassing (Larson & Erba, 1999; Tejada et al., 2009), or by the dissociation of methane hydrates (Jahren, 2002). The biostratigraphic record of the event is manifested by first, an increased speciation of calcareous nannofossils, followed by a drastic decrease in the calcification of these fossils as well as of planktonic foraminifera, known as the "nannoconid crisis" (Erba, 1994).

While there are no radiometric ages available for OAE1a, two different astronomical tuning models have attempted to constrain the duration of the event, even though the astronomical solution of Laskar et al. (2004) does not apply in the Cretaceous. Li et al. (2008) correlate the carbon isotope records from Italy, Mexico, and the Iberian shelf to estimate a 1.27 Ma duration for OAE1a, with the initial negative $\delta^{13}C$ excursion occurring over 27–41 ka. Meanwhile, Malinverno et al. (2010) suggest a duration of OAE1a of 1.11 ± 0.11 Ma through astronomical tuning of the Cismon APTICORE borehole in Italy. They suggest that the record be tied to the base of polarity chron M0r, formerly estimated at 121 Ma (Channell et al., 1995), making the timing of OAE1a from 120.21 to 119.11 Ma. However, a review of advances in Early Cretaceous geochronology suggest that the base of chron M0r, which is also the Barremian-Aptian boundary, is conservatively between 123.8 and 121.8 Ma, following U-Pb CA-ID-TIMS and $^{40}Ar/^{39}Ar$ studies (Corfu et al., 2013; He et al., 2008; Midtkandal et al., 2016; Olierook et al., 2019). Thus, the timing of OAE1a is likely to have occurred at least 1 Ma if not a few Ma earlier than previously suggested. This time period would be a fruitful interval to pursue more high-precision radiometric constraints, to better ascertain the timing of this boundary and OAE1a.

The current state of geochronology for OJP and OAE1a allows for correlation of the events, since the ages for OJP overlap with the age assigned to OAE1a at ~120 Ma, though at an order of magnitude lower resolution. Higher-precision ages are required to improve this correlation, and to assess a causal relationship between oceanic LIP volcanism and this global climate event at the same resolution as other events in this chapter. Geochronology of the OJP is hindered by sample availability: there have been only a few ODP cores to drill into OJP basement, and it is exposed above sea level in only a few small islands, inhibiting wide sampling across both area and depth of the province. Furthermore, there is no description of felsic ash beds or gabbroic intervals in the basalts that may potentially yield zircon. Additionally, the low K content of the basalts has limited the precision of $^{40}Ar/^{39}Ar$ dating (Fitton & Godard, 2004). The pCO_2 proxy records suggest that the documented shift to lighter oceanic $^{187}Os/^{186}Os$ isotopes (Bottini et al., 2012; Tejada et al., 2009), reflecting volcanogenic mantle values, was concurrent with the rise in oceanic CO_2, strengthening the connection between OJP emplacement and the carbon cycle perturbation of OAE1a (Bergman et al., Chapter 9 this volume; Naafs et al., 2016).

Caribbean LIP and OAE2

The Caribbean LIP consists of 4.5 million km^3 (Kuroda et al., 2007) of highly faulted basaltic or picritic lavas and sills, layered gabbros, and ultramafic rocks interpreted to be a remnant of an eastern Pacific oceanic plateau that was inserted between North and South America (Bergman et al., Chapter 9 this volume). These rocks were obducted and exposed around the Caribbean margin and the northwestern coast of South America, and exhibit a thickness of 8–20 km (Sinton et al., 1998). With carbonized tree trunks and corals occasionally interbedded with the basalts, parts of the LIP appear to have been emplaced subaerially or in shallow water (Kerr, 2014). The limited presence of interbedded sediments and ash layers in the Caribbean LIP suggests rapid eruptions with few hiatuses (Kerr, 2014).

Like the OJP, most age constraints for the Caribbean LIP are based on whole-rock $^{40}Ar/^{39}Ar$ dates, constrained by biostratigraphic ages of surrounding sediments, which indicate that much of the LIP was emplaced before the Coniacian (89.8–86.3 Ma; Ogg et al., 2012). These dates similarly suffer from low precision as most of the rocks sampled were tholeiitic, with low K_2O content (Sinton et al., 1998; Snow et al., 2005). The primary pulse of Caribbean LIP volcanism seems to have occurred between 92 and 88 Ma (ranging from 92.0 ± 9.6 to 87.9 ± 4.2 Ma), as evidenced by dates from outcrops on Haiti, Colombia, Costa Rica, Curacao, as well as from DSDP cores sampling the Venezuelan basin (Kerr et al., 2003; Sinton et al., 1998). More recent whole-rock $^{40}Ar/^{39}Ar$ dating has yielded a weighted mean of four dates of 93.96 ± 0.38 Ma for the Dumisseau Formation in Haiti, and 92.75 ± 0.46 Ma for a sample from Curacao (Snow et al., 2005). These dates suggest that volcanism was broadly synchronous across the region over a short period of time, potentially 1–2 Ma. A second set of ages from basalts in Columbia, a sill in Curacao, volcanics in Haiti, and from DSDP Site 152 reveal a younger phase of volcanism from 76 to 72 Ma, which is as extensive in area as the first phase, but is likely less voluminous, and may be related to extension as the plateau was emplaced in its current location (Sinton et al., 1998).

OAE2 was first recognized as a 1-m-thick package of laminated black shale with total organic carbon content >30% in the Umbria-Marche region of Italy (Schlanger & Jenkyns, 1976). The black shale has been found across the globe, most prominently in pelagic Atlantic settings, the Caribbean, and Alpine-Mediterranean areas, and to a lesser extent in north Africa and Asia (Jenkyns, 2010). This global distribution suggests a widespread reducing environment occurring in the context of a major sea-level transgression, higher global temperatures with elevated pCO_2, and a positive carbon isotope excursion of 4–5‰, reflecting increased rates of productivity and organic carbon burial (Jenkyns, 2010). The timing of this event, overlapping the Cenomanian-Turonian boundary, is also coincident with an extinction event in which 26% of known genera were lost, particularly affecting more than half of ammonoid and brachiopod genera (Kerr, 2014). Oceanic LIP volcanism has been implicated as a potential cause of OAE2 because of this loss in deep marine biota, the geochemical signature of black shales resembling oceanic plateau, and the increase in productivity related to a greater flux of nutrients provided by volcanism (Kerr, 2014).

Sedimentary sections containing the records of OAE2 have been astronomically tuned to suggest a range of possible durations of the event: 1.8 Ma for the Bonarelli level in central Italy, with the event beginning at 94.21 or 93.72 Ma (Mitchell et al., 2008), 430–445 ka for the Wunstorf section in northern Germany (Voigt et al., 2008), 600 ka for the Greenhorn Formation in the western USA (Meyers et al., 2001; Sageman et al., 2006). A recent high-precision U-Pb zircon geochronology study of bentonites bracketing OAE2 in the Yezo Group of Japan has refined the timing and duration of the event, which begins at 94.436 ± 0.093/0.14 Ma ([X/Z], MSWD = 0.8, n = 5), and ends at 93.920 ± 0.031/0.11 Ma ([X/Z], MSWD = 2, n = 3) (Du Vivier et al., 2015). This age model yields a duration of 392–640 ka, in broad agreement with prior astrochronological constraints. The age model's timing for OAE2 also overlaps with the Cenomanian-Turonian Boundary age of 93.90 +0.07/-0.09 Ma, (± 0.15 Ma) [X/Z], which was derived from intercalibrated $^{40}Ar/^{39}Ar$, U-Pb, and astrochronology of the Western Interior Seaway (Meyers et al., 2012).

Given its observed temporal coincidence, the Caribbean LIP has frequently been implicated as one of the causes of OAE2, though other LIPs, such as the High Arctic LIP (Polteau et al., 2016) and the flood basalt volcanism from the rifting of Madagascar (Storey et al., 1995; Turgeon & Creaser, 2008) have also been implicated as possible causes (Bergman et al., Chapter 9 this volume; Kendall et al., Chapter 13 this volume). However, high-precision geochronology studies of these LIPs will be required to better understand this connection now that the occurrence of OAE2 is well constrained to ~94 Ma (Fig. 2.2). With uncertainty on the order of a few million years, many of the ages used to suggest a first main phase of Caribbean volcanism at 92–88 Ma overlap with the OAE2 zircon ages (Kerr et al., 2003; Sinton et al., 1998; Du Vivier et al., 2015), including the higher-precision $^{40}Ar/^{39}Ar$ dates from the Dumisseau Formation (Snow et al., 2005). While it is also possible that the main phase of the Caribbean LIP eruption could have postdated OAE2 entirely, and may in fact align better with the Turonian-Coniacian boundary (Ogg et al., 2012), a variety of osmium isotope records suggest that a large mag-

matic pulse triggered the onset of OAE2 (Turgeon & Creaser, 2008; Du Vivier et al., 2014). While the Caribbean LIP suffers from its fragmentary, fault-bounded nature, complicating sampling across its full vertical stratigraphy and horizontal extent, higher-precision ages would allow for a better understanding of its timing, duration, effusion rate, and connection to OAE2.

2.2.9. Deccan Traps and End-Cretaceous Extinction

In the late Cretaceous at ca. 90 Ma, the Indian subcontinent rifted from Madagascar, marking the initial drift of India toward Eurasia, an event that culminated in the Himalayan Orogeny (Besse & Courtillot, 1988; Raval & Veeraswamy, 2003). The impingement of the Reunion plume under the western Indian margin occurred ca. 66 Ma, which resulted in the eruption of the Deccan Traps flood basalt province. As outlined below, the timing of the Deccan Traps corresponds well with the end-Cretaceous mass extinction event, though whether it played a role in that disaster remains heavily debated due to the simultaneous occurrence of the Chicxulub bolide impact and the evidence that the impact coincided with the potentially very rapid extinction of marine organisms (Keller et al., 2012; Schulte et al., 2010).

The Deccan Traps covers ~500,000 km^2 of western India, with estimated volumes ranging from 1–2 million km^3 (Jay & Widdowson, 2008; Richards et al., 2015; Self et al., 2008). Large uncertainties in the total volume derive from both the portion of the Deccan that is eroded and also from the amount of basaltic magma that is currently below sea level on the continental shelf off the west coast of India. However, by comparison to other flood basalts, the stratigraphy of the Deccan Traps is well exposed along the western margin of the 1,000 m elevation Deccan plateau, called the Western Ghats, where deep erosion down to the coastal plain has resulted in outstanding exposure of the volcanic stratigraphy. As a result, geological, paleomagnetic, and geochemical studies conducted over several decades have generated a very well-characterized stratigraphy of the Deccan Traps relative to many other flood basalt provinces (Beane et al., 1986; Chenet et al., 2007, 2008, 2009; Khadri et al., 1988; Subbarao et al., 2000).

The stratigraphy of the Deccan Traps has been divided into 12 formations within three subgroups that can be well correlated over ~80,000 km^2 surrounding the Western Ghats. The stratigraphy becomes less certain toward the east, south, and north, though geochemical and paleomagnetic data have been used to correlate with the Western Ghats (Courtillot et al., 2000; Jay & Widdowson, 2008; Schöbel et al., 2014; Self et al., 2008; Shrivastava & Pattanayak, 2002). As one spectacular example, basalt flows exposed in quarries on the southeast coast of India are thought to have traveled thousands of kilometers within the Krishna-Godavari paleo river valley from the Western Ghats into the Indian Ocean. Paleomagnetic, geochemical, and chronologic data support an affiliation with the Deccan Traps, though exact correlations have yet to be confirmed (Keller et al., 2008; Knight et al., 2003; Self et al., 2008). While these peripheral flows are important for understanding of the overall evolution of the Deccan Traps, they are volumetrically less significant and therefore perhaps less important for understanding the paleoclimatic implications of the Deccan eruptions.

Because portions of the Deccan Traps are interstratified with sediments containing late Cretaceous flora and fauna, they have been long known to potentially overlap with the end-Cretaceous mass extinction (McLean, 1985). K-Ar, ^{40}Ar/^{39}Ar, Re-Os geochronology and paleomagnetic data were gathered over several decades (Allègre et al., 1999; Baksi, 1994; Chenet et al., 2007; Courtillot et al., 1986, 1988, 2000; Duncan & Pyle, 1988; Hofmann et al., 2000; Hooper et al., 2010; Knight et al., 2003; Pande, 2002; Venkatesan et al., 1993), which confirmed that the majority of the eruptions occurred during chron C29r (now known to be between ca. 66.3 and 65.6 Ma), but beginning and finishing during normal polarity (Chenet et al., 2009; Courtillot et al., 2000) (Fig. 2.7). Chron 29r contains the end-Cretaceous mass extinction and the Cretaceous-Paleogene boundary, which has been defined as the timing of the Chicxulub impact (see review in Smit, 1999). However, uncertainties of ± 1–2 Ma or more on the dates for the Deccan Traps prevented a high-resolution correlation of the Deccan Traps with the Chicxulub impact and the biotic crisis. Additionally, the age uncertainties when combined with paleomagnetic data led several authors to conclude that an early pulse of volcanism as old as 68 Ma predated the main phase in the western Ghats sections (Chenet et al., 2007) indicating a total duration of volcanism to be several millions of years.

Two recent ongoing efforts using ^{40}Ar/^{39}Ar and U-Pb geochronology have established a much higher resolution timeline for the eruption of the Deccan Traps. The ^{40}Ar/^{39}Ar geochronology has focused on multigrain plagioclase separates from Deccan basalt flows (Renne et al., 2015; Sprain et al., 2019), whereas the U-Pb geochronology is based on dating single zircons from volcanic ash interstratified with the basalts (Schoene et al., 2015, 2019). Both data sets show that over 90% of the Deccan Traps erupted between ~66.3 and 65.6 Ma, and therefore do not support a prolonged eruption over millions of years in the Western Ghats. Neither of the studies have dated the C30n portion of the Deccan Traps nor the topmost formations, so the total duration cannot yet be calculated. However, U-Pb geochronology of the same outcrop originally reported to be 67–68 Ma (Chenet et al., 2007) and of transitional polarity was shown to

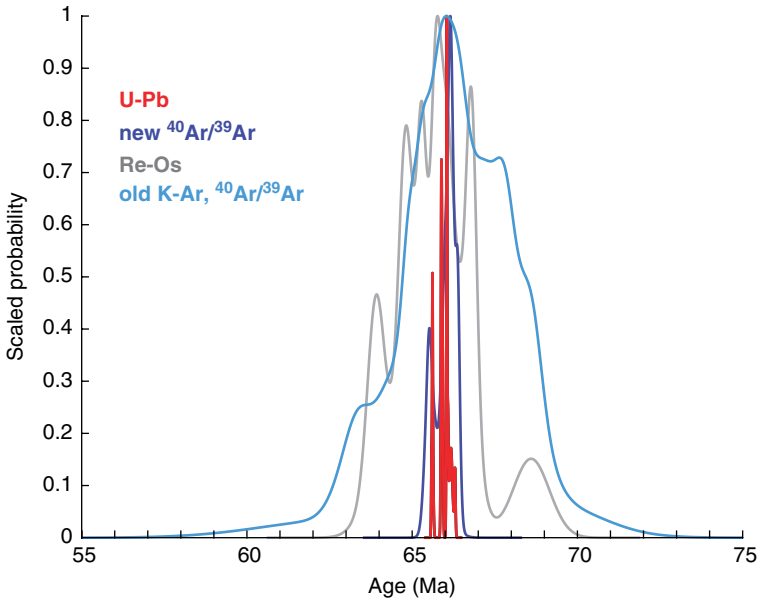

Figure 2.7 Geochronology of the Deccan Traps, India. Probability density function for Re-Os, $^{40}Ar/^{39}Ar$, and U-Pb ID-TIMS geochronology obtained for the Deccan Traps. U-Pb data are from Schoene et al. (2019); new $^{40}Ar/^{39}Ar$ data are from Sprain et al. (2019); Re-Os data are from Allègre et al. (1999); and old K-Ar and $^{40}Ar/^{39}Ar$ are from Baksi (1994), Chenet et al. (2007), Courtillot et al. (1986, 1988, 2000), Duncan and Pyle (1988), Hofmann et al. (2000), Hooper et al. (2010), Knight et al. (2003), Pande (2002), Venkatesan et al. (1993).

represent the C30n-C29r transition at ca. 66.3 Ma (Schoene et al., 2015) supporting a short duration.

Both the recent $^{40}Ar/^{39}Ar$ and U-Pb data sets (Renne et al., 2015; Schoene et al., 2015, 2019; Sprain et al., 2019) have excellent coverage of the entire Deccan stratigraphy and reveal good agreement between the two methods, but a direct comparison of absolute ages remains difficult. This is because of systematic uncertainties between the $^{40}Ar/^{39}Ar$ to U-Pb dating methods that arise from the decay constants and physical constants of both the ^{238}U and ^{40}K decay schemes (Min et al., 2000; Renne et al., 1998a, 2010; Schoene et al., 2006), which are discussed in the dating methods section, 2.2.1. Given these uncertainties, we refrain from comparing the $^{40}Ar/^{39}Ar$ and U-Pb data at better than the 200 kyr level, but instead focus on the data sets and calculated eruption rates internally and compare to geochronology from the same system for assessing their temporal relation to the Chicxulub impact.

Because of the spectacular exposure and preservation of the Deccan Traps in the western Ghats, the $^{40}Ar/^{39}Ar$ and U-Pb data sets can be combined with models for the relative volumes of each formation (Richards et al., 2015) and used to calculate volumetric eruption rates for the flood basalts. Doing so with the U-Pb data set reveals that the Deccan Traps erupted in four major pulses, separated by relative lulls in volcanism of up to 100 ka (Fig. 2.8). The $^{40}Ar/^{39}Ar$ data set, in contrast, shows roughly constant eruption rates over the entirety of the Deccan Traps.

However, the comparably large uncertainties associated with the $^{40}Ar/^{39}Ar$ data set make it impossible to test the presence of pulses identified by the U-Pb data set. A challenge facing both dating methods in calculating eruption rates is the large uncertainties in the volume models for the flood basalt, in addition to the unknown volume or age of basalts located offshore to the west of the Indian margin. Furthermore, the intrusive component of the Deccan Traps is poorly exposed, compared with other LIPs, and thus difficult to compare with the eruption record. As a result, estimating volatile release associated with the Deccan Traps remains a challenge.

The end-Cretaceous mass extinction has not been directly dated. Terrestrial records have low stratigraphic resolution, making it difficult to pinpoint an extinction horizon, and no geochronology has been published from marine records. However, ejecta material from the Chicxulub impact has been well dated by both U-Pb and $^{40}Ar/^{39}Ar$ geochronology. Given the stratigraphic correspondence between the impact ejecta and the peak marine extinction, these dates may also calibrate the timing of the extinction. U-Pb dates on impact ejecta come from zircon geochronology of ash beds bracketing Chicxulub ejecta in the Denver Basin, Colorado (Clyde et al., 2016); the $^{40}Ar/^{39}Ar$ date comes from both sanidine extracted from ash beds bracketing Chicxulub ejecta in Hells Creek, Montana, and on glassy tektites defining the Cretaceous-Paleogene boundary from both Haiti and Columbia

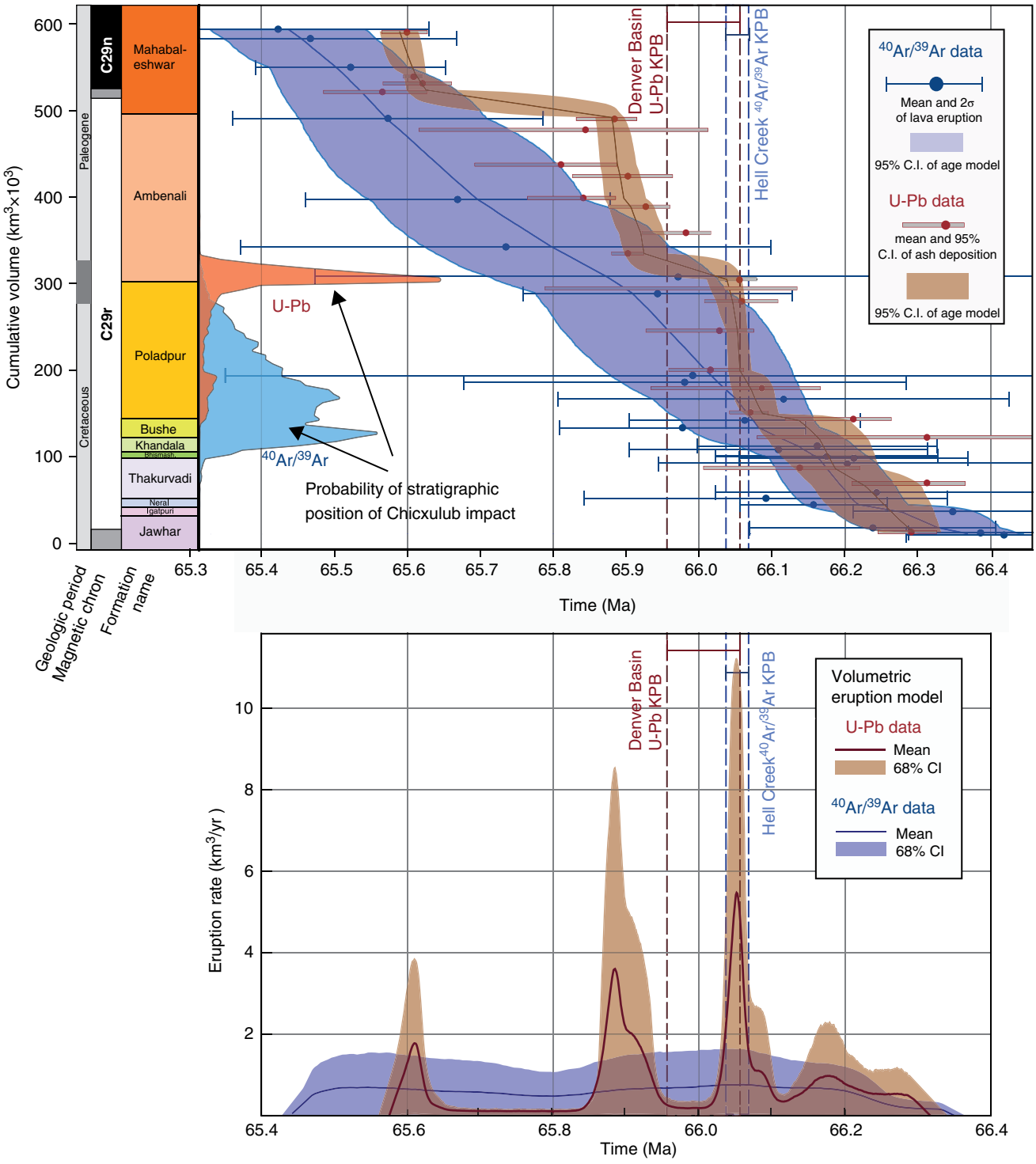

Figure 2.8 High-precision geochronology from the Deccan Traps, India. Compilation of recently published $^{40}Ar/^{39}Ar$ and U-Pb data sets (Sprain et al., 2019; Schoene et al., 2019), compared using the same Bayesian techniques for generating an eruptive age model from each data set (Schoene et al., 2020). Upper plot shows the age of stratigraphic units versus the cumulative volume of basalt, using the volume model of Richards et al. (2015). Lower plot shows the corresponding volumetric eruptive rate. Methods are outlined in Schoene et al. (2019). As an output of the same model, the probabilistic position of the Chicxulub impact within the Deccan Traps for each data set is shown, using the Chicxulub U-Pb date from Clyde et al. (2016) and the $^{40}Ar/^{39}Ar$ date from Sprain et al. (2018), compared with the age model derived from each method.

(Renne et al., 2013, 2018; Sprain et al., 2018). Both U-Pb and $^{40}Ar/^{39}Ar$ data sets show that the Deccan Traps began several hundred thousand years before the Chicxulub impact and continued for a similar duration afterward. It has been hypothesized that seismic energy from the impact itself may have influenced the eruption of the Deccan Traps, for example by leading to an increase in eruption rates (Renne et al., 2015; Richards et al., 2015). While the $^{40}Ar/^{39}Ar$ data set cannot rule this model out (Sprain et al., 2019), the U-Pb data set shows a pulse of eruptions likely beginning before the impact and a decrease afterward, suggesting the Chicxulub impact and Deccan Traps were completely independent of one another (Schoene et al., 2019).

There remains much to learn about what the effect of the Deccan Traps may have been on the end-Cretaceous mass extinction event. Several data sets have argued for a role for Deccan Traps in late Maastrichtian ecological changes, such as a warming and cooling event evidenced by oxygen isotopes records in foraminifera (Barnet et al., 2017; Li & Keller, 1998; Tobin et al., 2012) and fossil leaf evolution (Wilf et al., 2003), evidence for biologic disturbance in the lead-up to the Chicxulub impact (Henehan et al., 2016; Petersen et al., 2016; Punekar et al., 2014; Wilson, 2014; Wilson et al., 2014), and a significant change in silicate weathering documented by seawater Os isotopes (Ravizza & VonderHaar, 2012; Robinson et al., 2009). The pulse of Deccan volcanism identified in the U-Pb data set that begins within tens of ka before the Chicxulub impact may hint at a closer temporal link between volcanism and the main extinction event. However, environmental, climate, and biologic records within this timeframe do not paint a clear picture as to what the effect of volcanism was. Some evidence of a hyperthermal event prior to the Chicxulub impact in Elles, Tunisia, has been suggested (Thibault et al., 2016), but corroborating records are scarce. A better understanding of the contribution of the Deccan Traps to the end-Cretaceous mass extinction and recovery period will require continued stratigraphic work generating very high resolution biotic and proxy records, geochronology from marine sections, as well as continued geochronology on the Deccan Traps to test recently established eruptive histories, including the intrusive history.

2.2.10. North Atlantic Igneous Province and Paleocene-Eocene Thermal Maximum

The North Atlantic Igneous Province (NAIP) initiated when the proto-Icelandic plume impinged on the base of Greenland (Larsen et al., 1999; Richards et al., 1989). Magmatism initiated as a result ca. 61–62 Ma in what is now West and East Greenland, Baffin Island, the Faeroe Islands, and throughout the British Isles (Saunders, 2016). Magmatism continued during rifting of east Greenland and Europe, where inferred plume magmatism is superimposed on midocean ridge magmatism of the mid-Atlantic ridge, forming thickened crust ridges leading toward Iceland (Saunders, 2016; Saunders et al., 1997). In addition to the exposed basalt stratigraphy associated with the NAIP, abundant submarine sills have been imaged seismically along the continental margins (so-called seaward dipping reflectors; White et al., 1987), some of which have been dated from drill core and shown to be synchronous with the NAIP (Svensen et al., 2010). Given the fragmentary nature of the NAIP and the abundance of submerged intrusive rocks, the volume of the NAIP has been difficult to determine. An estimate of pre-erosion volume for extrusive rocks of ~1.8 million km^3 is often cited (Eldholm & Grue, 1994), and estimates for the total magmatic volume including intrusive rocks range between 5 and 10 million km^3 (Eldholm & Grue, 1994; White et al., 1987). Despite potentially being one of the largest LIPs, there is no mass extinction associated with the NAIP. However, geochronology suggests that peak magma production rates may have coincided with the Paleocene-Eocene boundary and the associated hyperthermal event (the PETM). Testing this correlation requires high-precision geochronology on both basalts, intrusive rocks, and sedimentary sections that contain the PETM.

Published geochronology for the NAIP includes data from the $^{40}Ar/^{39}Ar$, K-Ar, U-Pb, Re-Os, and Rb-Sr methods. In a recent comprehensive review of existing geochronology, Wilkinson et al. (2017) rejected the vast majority of these dates based on criteria including poor data quality, incomplete data reporting, dubious interpretations, ambiguous data handing, and questionable sample quality. Their resulting database focuses on subaerial sampling localities and includes between ~80 and 120 $^{40}Ar/^{39}Ar$ and U-Pb dates; the number of acceptable dates depends predominantly on whether groundmass, glass, or whole-rock data were included for $^{40}Ar/^{39}Ar$ data (Fig. 2.9a). Our summary here focuses on their more restrictive database that contains only pure mineral separates, given that whole-rock, groundmass, and glass $^{40}Ar/^{40}Ar$ dates are too often inaccurate (see other sections of this chapter).

The majority of dates within the subset are $^{40}Ar/^{39}Ar$ dates from a handful of studies on basalts and gabbros from West Greenland, East Greenland, the Faeroe Islands, and the British Isles (Fig. 2.9b). Both intrusive and extrusive samples have been dated, and some studies (Larsen et al., 2014, 2016; Storey et al., 2007b) focus on sampling from known stratigraphic sections in order to make regional correlations and estimate volumetric eruption rates. Modern ID-TIMS U-Pb geochronology for the NAIP is sparse. Eight dates have been published,

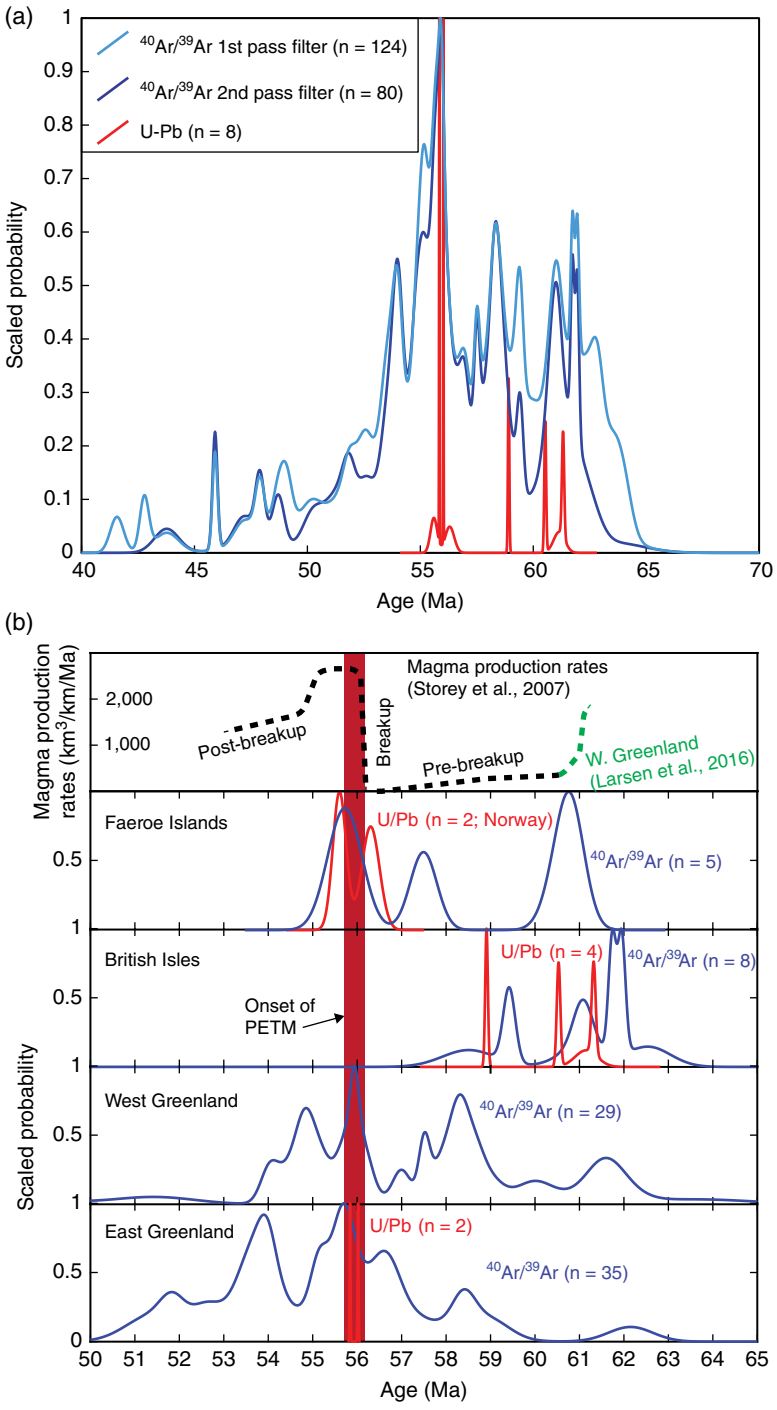

Figure 2.9 Geochronology of the North Atlantic Igneous Province (NAIP). Probability density function for $^{40}Ar/^{39}Ar$ and U-Pb ID-TIMS geochronology obtained for the NAIP, as compiled by Wilkinson et al. (2017). The first pass filter of Wilkinson et al. (2017) eliminated dates in the NAG-TEC database adversely affected by poor data quality, incomplete data reporting, dubious interpretations, ambiguous data handling, and questionable sample quality. The second pass filter removes whole-rock, groundmass, and glass $^{40}Ar/^{39}Ar$ dates, leaving only dates from pure mineral separates.

from the British Isles (Chambers et al., 2005; Hamilton et al., 1998) and from submarine cores off the coast of Norway (Svensen et al., 2010). One study of the Skaergaard intrusion in East Greenland was not included in the compilation of Wilkinson et al. (2017) in which construction of the mafic complex was estimated to be between 56.02 ± 0.02 and 55.84 ± 0.02 Ma (Wotzlaw et al., 2012).

The results show that magmatism began in the early Paleocene and continued well beyond the Paleocene-Eocene boundary. These geochronologic data have led to the hypothesis that the NAIP was erupted and intruded in two main phases, one that predates the initial breakup of Greenland, North America, and Europe ca. 63–61 Ma, and a second beginning ca. 56 Ma (Larsen et al., 2014, 2016; Storey et al., 2007a, 2007b). Wilkinson et al. (2017) argue that, given their full compilation of available geochronology, this gap in magmatism is less significant. However, assessing changes in the rates of magmatism that may define different phases requires robust volumetric estimates of eruption rates, which are difficult to calculate given the fragmentary preservation of the NAIP. In an attempt to reconcile this, Storey et al. (2007a, 2007b) combined stratigraphically resolved $^{40}Ar/^{39}Ar$ geochronology from eastern Greenland with estimates of volumes of each formation to calculate an order of magnitude increase in eruption rates that defines the onset of the second phase of magmatism ca. 56 Ma. In a similar effort in western Greenland, Larsen et al. (2016) also calculate higher eruption rates in the prebreakup phase prior to ca. 61 Ma.

The most severe hyperthermal event in the Cenozoic, the Paleocene-Eocene Thermal Maximum (PETM), may overlap with the onset of the second phase of NAIP magmatism. The PETM is marked globally in marine and terrestrial stratigraphic records. It is recorded by both a negative $\delta^{13}C$ anomaly of carbonate and organic carbon of several permill, and also a negative $\delta^{18}O$ anomaly in foraminifera that indicates a warming of seawater of 3–4°C (Cui et al., 2011; Zachos et al., 2001, 2005; see also Bond & Sun, Chapter 3 this volume). The duration of the PETM has been estimated to be either 170 ka or 220 ka, by cyclostratigraphy on astronomically tuned sediments (Röhl et al., 2007) and extraterrestrial ^{3}He accumulation (Murphy et al., 2010), respectively. The absolute timing of the onset of the PETM has been calibrated through a combination of U-Pb and $^{40}Ar/^{39}Ar$ geochronology on volcanic ash beds and cyclostratigraphic estimation of the time between the onset and stratigraphic position of the ash bed (Charles et al., 2011; Jaramillo et al., 2010; Storey et al., 2007a; Westerhold et al., 2009). These result in a range of estimates spanning 500 ka between ca. 55.7 and 56.2 Ma, despite reported uncertainties on the geochronology of 100 ka or better. The uncertainties in these estimates derive from both the uncertainties in standard ages used for $^{40}Ar/^{39}Ar$ dates, the interpretation of the U-Pb zircon data, and the assumptions inherent in cyclostratigraphy, for example that observed cyclicity is caused by Milankovitch cycles and that there are no hiatuses.

There is agreement that the PETM was likely driven by delivery of a large amount of isotopically light carbon to the ocean-atmosphere system, but the source and isotopic composition of that carbon remain debated. Possible sources include methane hydrate dissociation (Dickens et al., 1995), organic carbon volatilization through contact with NAIP sills (Svensen et al., 2004, 2010), weathering of exposed organic-rich epicontinental seaways (Higgins & Schrag, 2006), and mantle carbon derived directly from NAIP magmatism (Gutjahr et al., 2017). It is difficult to reconcile the negative carbon isotope shift of the PETM with mantle carbon extracted from the NAIP, thus explaining the attraction to methane hydrate or organic carbon volatilization. However, Gutjahr et al. (2017) argue based on the pH of seawater derived from boron isotope measurements combined with carbon isotope mass balance that volcanic/mantle carbon was an important source of CO_2 for the driving the PETM (see also Babila & Foster, Chapter 17 this volume). In order to resolve this issue, more stratigraphically linked, high-precision geochronology is necessary from the NAIP to calculate eruption rates during the breakup phase of the magmatism. Also, the differences in estimates for the onset of the PETM need to be resolved (Charles et al., 2011), likely through a combination of geochronology and potentially cyclostratigraphy in sections that record the PETM. It is unlikely that cyclostratigraphic estimates for the timing of the PETM alone will have the accuracy to resolve this question (Westerhold et al., 2012).

2.2.11. Columbia River Basalt Group and Miocene Climate Optimum

The Columbia River Basalt Group (CRBG), the youngest, smallest, and best-preserved continental flood basalt, erupted 210,000 km^3 of lava over Washington, Oregon, and Idaho, USA from ~17–6 Ma. Due to its accessibility, it has been the subject of numerous stratigraphic, paleomagnetic, geochemical, mapping, and geochronological studies, providing an unparalleled level of detail for LIP researchers. The province has been divided into five formations (Steens Basalt, 15.3% of total volume; Imnaha Basalt, 5.3%; Grande Ronde Basalt, 72.3%; Wanapum Basalt, 5.9%; and Saddle Mountains Basalt, 1.2%), and each of these has been subdivided into 2–24 stratigraphic members based on mineralogy, geochemistry, and paleomagnetic signature. Volume estimates exist for each member, consisting of 1–20 tholeiitic basalt to basaltic andesite lava flows (Reidel, 2015).

For decades, K-Ar and $^{40}Ar/^{39}Ar$ geochronology techniques have been used in order to assess the timing and duration of CRBG volcanism. However, large uncertainties (>1 Ma) in these analyses, with ages overlapping despite known stratigraphic order, have precluded the development of an unambiguous chronology. The most recent review of $^{40}Ar/^{39}Ar$ dates for the basalts (Fig. 2.10) suggests an age model of Steens Basalt erupting from 16.9–16.7 Ma, the Imnaha Basalt from 16.7–16.0 Ma, the Grande Ronde Basalt from 16.0–15.6 Ma, the Wanapum Basalt from 15.6–15.0 Ma, and the Saddle Mountains Basalt in small events between 15 and 6 Ma (Barry et al., 2013). This age model yields several inconsistencies with the Geomagnetic Polarity Timescale (GPTS) (Hilgen et al., 2012). For example, the universally normally magnetized Imnaha Basalt would have erupted during an interval with two complete magnetic field reversals, while the Grande Ronde Basalt, which does exhibit two complete reversals, would have erupted during a reversed chron.

Recent high-precision geochronological studies using both $^{40}Ar/^{39}Ar$ and U-Pb methods have provided a reassessment of the CRBG age model. Since plagioclase phenocrysts extracted from basalt contain low concentrations of K_2O, and basaltic groundmass can be easily altered, Mahood and Benson (2017) performed $^{40}Ar/^{39}Ar$ geochronology on feldspar phenocrysts extracted from rhyolitic and trachytic tuffs intercalated with and below the Steens Basalt. Improving on the precision of prior studies by an order of magnitude, the oldest tuff in their study of the Main Scarp section of the southern Pueblo Mountains is dated at 16.699 ± 0.028 Ma, and the youngest tuff is 16.601 ± 0.048 Ma. Twenty-four lava flows comprising 230 m of section were emplaced between the tuffs, allowing for the calculation of an average eruption rate of 2.4 m/ka (1.3–11 ka at 95% confidence interval). With these constraints, they estimate that the Steens Basalt erupted from ~16.75–16.54 Ma, and that the Steens Mountain geomagnetic reversal occurred at 16.602 ± 0.028 Ma (all dates recalculated with Fish Canyon Sanidine age of 28.201 (Kuiper et al., 2008) and expressed with 2σ model error).

A similar approach was undertaken by Kasbohm and Schoene (2018), who extracted zircons from silicic ash beds interbedded throughout the CRBG stratigraphy and dated them with U-Pb geochronology through CA-ID-TIMS. Zircon ages show that 95% of the eruptive volume was emplaced in 758 ± 66 ka, 2.4 times faster than previous estimates (Camp, 2013), between 16.653 ± 0.063 Ma in the lower Steens Basalt, and 15.895 ± 0.019 Ma in the upper Wanapum Basalt. Zircon dating in the Steens Basalt gives good agreement with the results of Mahood and Benson (2017). The volume estimates for CRBG stratigraphic members allow the calculation of an average effusion rate of 0.334 ± 0.042 km^3/year for the Steens, Imnaha, and Grande Ronde Basalts; volcanism slows during the emplacement of the Wanapum Basalt, to a rate of 0.055 ± 0.014 km^3/year. The samples also indicate at least one effusive pulse of volcanism; the Wapshilla Ridge Member, which makes up 20% of the total CRBG

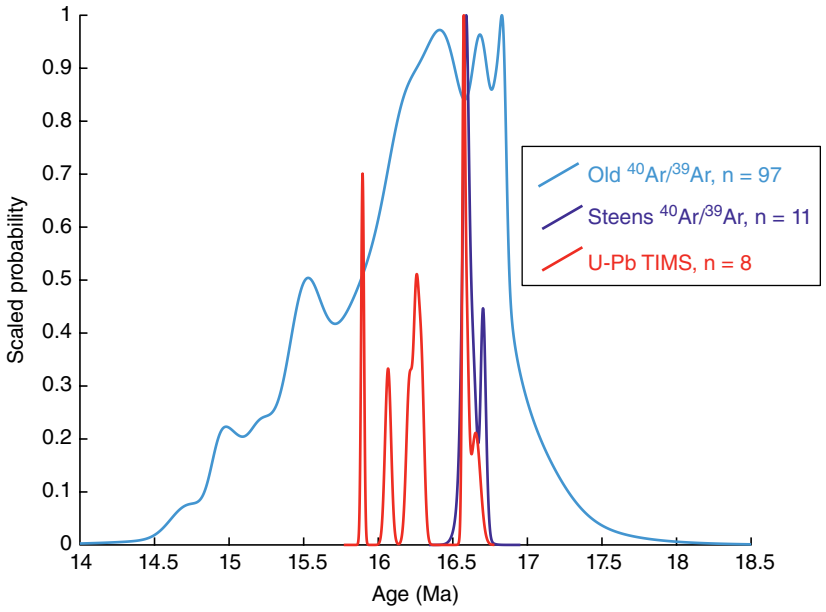

Figure 2.10 Geochronology of the Columbia River Basalt Group (CRBG). Probability density function for $^{40}Ar/^{39}Ar$ and U-Pb ID-TIMS geochronology obtained for the CRBG, comparing the compilation of $^{40}Ar/^{39}Ar$ dates by Barry et al. (2013) with age constraints on the Steens Basalt (Mahood & Benson, 2017) and CRBG zircon geochronology (Kasbohm & Schoene, 2018). Dates for Saddle Mountains Basalt are omitted.

volume, was emplaced at an average rate of 1.18 km^3/year, though the dates for the top and bottom of the member overlap with ~30 ka precision, permitting extremely rapid eruption.

A connection between the emplacement of the CRBG and the ~17–15 Ma Miocene Climate Optimum (MCO) has long been suggested (Hodell & Woodruff, 1994; see also discussion by Babila & Foster, Chapter 17 this volume). This interval was marked by elevated high-latitude sea surface temperatures 4–6°C above background (Shevenell et al., 2004), with a benthic $\delta^{18}O$ minimum, a benthic $\delta^{13}C$ maximum, and an inferred reduction in high-latitude ice sheet extent (Armstrong McKay et al., 2014). Vertebrates migrated poleward as temperatures warmed, with increased species originations (Böhme, 2003). A variety of pCO_2 proxy records, including stomata (Kürschner et al., 2008), alkenone (Zhang et al., 2013), and $\delta^{11}B$ (Foster et al., 2012) proxies indicate a possible doubling of atmospheric CO_2 levels to >400 ppm concurrent with the warming. CRBG volcanism has been suggested as the source of the CO_2 that led to this warming, and the prior age model for volcanism (Barry et al., 2013) offered a reasonable temporal overlap for these events.

However, there are no radiometric dates calibrating the timing and duration of the MCO, inhibiting an assessment of its connection to the CRBG, particularly in light of new high-precision age models for flood volcanism. The early and middle Miocene has proven to be the most difficult interval of the Neogene for establishing precise independent chronologies in the marine sediments that exhibit the MCO due to problems obtaining undisturbed stratigraphic sections that yield reliable magnetostratigraphy, biostratigraphy, astronomical tuning, and radiometric ages (Hilgen et al., 2012). All Miocene timescales depend in some way on correlation with the GPTS, for which there are currently several proposals. The most recent, Geologic Time Scale 2012 (Hilgen et al., 2012), notes that the interval from 17 to 14 Ma is the only portion of the Neogene GPTS that is not calibrated by astronomical tuning of a core with reliable magnetostratigraphy. Instead, this interval was calibrated by seafloor anomaly profiles of the Antarctic and Australian plates, and assuming a relatively constant spreading rate to give a 23.03 Ma age for the Oligocene-Miocene boundary. Proxy records of the MCO use a variety of age models that yield conflicting accounts of the timing of the event, inhibiting the ability to compare its timing to that of CRBG eruptions (Foster et al., 2012; Holbourn et al., 2007, 2015).

In the absence of radiometric ages for the MCO, one way forward, as suggested by Kasbohm and Schoene (2018), may be to focus on MCO records with reliable magnetostratigraphy. By integrating U-Pb zircon dates into the magnetostratigraphic framework of the CRBG, Kasbohm and Schoene (2018) suggest four absolute age constraints on the ages of magnetic field reversals concurrent with CRBG eruption. These absolute ages differ from all prior calibrations of the GPTS, indicating that prior GPTS age models may be in error. However, isotopic records of the MCO that also yielded magnetostratigraphy may be aligned with the proposed GPTS recalibration, and compared with the zircon-derived age model for CRBG eruptions. At Sites 1090 (Billups et al., 2004; Channell et al., 2003) and U1335 (Kochhann et al., 2016), the decline in benthic $\delta^{18}O$, a proxy for deep-ocean temperature, occurs in chron C5Cr, which is the same chron in which CRBG eruptions began with the lower Steens Basalt, and reach a nadir during chrons C5Cn.3n–C5Cn.1r, during which time the Grande Ronde Basalt was erupting. The astronomically tuned record from U1335 suggests that the decline in $\delta^{18}O$ may have begun 100–200 ka before the onset of Steens eruptions. This offset may be explained by the onset of cryptic degassing of CO_2 as magma migrated through CRBG dike swarms (Armstrong McKay et al., 2014), or it may suggest that these events are unrelated. Further work improving age models for the MCO is required in order to determine its relationship to the CRBG.

Regardless of adjustments to individual proxy records that may occur through refining MCO age models, global proxy data (Zachos et al., 2008) indicate that the MCO continued for ~1 Ma after the termination of all but the smallest CRBG eruptions by 15.895 ± 0.019 Ma (Kasbohm & Schoene, 2018). A continuation of warm temperatures following the cessation of volcanism may be explained by the long response time of the silicate weathering feedback, which may occur on 200–500 ka timescales (Stolper et al., 2016), allowing for volcanogenic CO_2 drawdown over 1 Ma. Alternatively, the CRBG may not be the primary driver for the MCO. Other explanations include changing dynamics of the East Antarctic Ice Sheet (Foster et al., 2012) and changes in global oceanic circulation (Holbourn et al., 2014).

2.3. DISCUSSION

Our review of high-precision geochronology of LIPs and their corresponding environmental perturbations permits new insights to be gained toward understanding the temporal overlap of these events (Fig. 2.2), and potential patterns across these LIP/event couplets in three different areas: (1) the duration and dynamics of LIP magmatism; (2) correlation of LIP magmatism with mass extinctions and environmental change; and (3) challenges and future opportunities in geochronology to better assess how LIPs disrupt the Earth system.

2.3.1. Duration and Dynamics of LIP Magmatism

Continued improvement in the accuracy and precision of both U-Pb and $^{40}Ar/^{39}Ar$ geochronometers and their widespread application to LIP rocks have progressively narrowed estimates for the total duration of LIP emplacement in most cases (Figs. 2.3–2.9). In particular, $^{40}Ar/^{39}Ar$ and K-Ar data sets published before ca. 2010 seemed to indicate eruption durations of at least several Ma for most LIPs, whereas recent refinements, predominantly by U-Pb geochronology, have drastically shortened that duration to <1 Ma. This pattern of decreasing emplacement duration as age accuracy and precision increase applies to the Emeishan LIP, Siberian Traps, CAMP, Karoo-Ferrar, Deccan Traps, and CRBG. Improved LIP age models also agree with magneto- and cyclostratigraphic timescales, as demonstrated by new age models for the CAMP, Deccan Traps, and CRBG (Blackburn et al., 2013; Kasbohm & Schoene, 2018; Schoene et al., 2015), which yield ages for magnetic field reversals in the basalt stratigraphy that are largely concordant with reversal ages suggested by astronomical tuning (Kochhann et al., 2016; Westerhold et al., 2008), and, in the case of the CRBG, yield better agreement with reversal ages proposed by the Geologic Time Scale 2012 (Hilgen et al., 2012) than the most recent $^{40}Ar/^{39}Ar$ age model (Barry et al., 2013). While these LIPs are sourced from a variety of geodynamic processes (related to mantle plumes, continental rifting, or upwelling related to subduction), they seem to have been emplaced in a characteristically brief timeframe, placing constraints on how long voluminous eruptions can be sustained.

One notable exception to the <1 Ma emplacement duration is the NAIP (Fig. 2.9), which shows magmatism extending over several million years. The changing geographic locus of emplacement may result from the movement of the North American and Eurasian plates over the hotspot thought to supply magma, and/or a varying contribution of mid-ocean ridge magmatism to erupted volume. Meanwhile, the other LIPs described in this chapter lack sufficient high-precision geochronology to sufficiently resolve emplacement duration at the ~1 Ma level.

In addition to a better understanding of overall emplacement duration, better dates have led to a more complete knowledge of the relative timing of intrusive and extrusive magmatism. For those LIPs with sufficiently high-precision geochronology and comprehensive sample coverage to resolve the timing of intrusion and extrusion (Siberian Traps, CAMP, Ferrar LIP, and NAIP), all permutations are seen, indicating that there is no characteristic pattern for the order of intrusive and extrusive emplacement of LIPs. For example, in the Siberian Traps, "Stage 1" extrusive magmatism is followed by "Stage 2" intrusion, which is followed by contemporaneous intrusion and extrusion in "Stage 3" (Burgess et al., 2017). For the CAMP, while further sampling may reveal new insights, currently geochronology is consistent with intrusion slightly predating extrusive magmatism, although both are ongoing through most of the LIP's duration (Davies et al., 2017; Fig. 2.5). In the Ferrar, weighted mean ages for sills are mostly older than the dates for lavas, though there is considerable overlap among individual zircon analyses from lavas and sills (Burgess et al., 2015). In the case of the NAIP, the highest-precision dates indicate contemporaneous extrusive and intrusive magmatism throughout the relatively long duration of emplacement. However, U-Pb dates, which have been instrumental in refining the timelines of other LIPs, are still scarce in the NAIP. For the Franklin and Kalkarindji LIPs, high-precision dates have been obtained only from intrusive units (Cox et al., 2015; Jourdan et al., 2014; Macdonald et al., 2010), while in the Deccan Traps and CRBG, high-precision age constraints have been provided only for lava flows (Kasbohm & Schoene, 2018; Mahood & Benson, 2017; Schoene et al., 2015, 2019; Sprain et al., 2019). For the remaining LIPs, both intrusive and extrusive rocks have been dated, but these dates lack the precision necessary to discern the relative order of emplacement style.

Continued improvement in radiometric dating accuracy and precision has also led to hypotheses regarding eruptive pulses within the overall LIP emplacement duration. These pulses are manifested as short periods of high-tempo volcanism punctuating periods of relative quiescence and have been documented via U-Pb geochronology in the Siberian Traps, CAMP, Deccan Traps, and CRBG. The CAMP age model of Blackburn et al. (2013) suggests CAMP emplacement in three discrete pulses over ~700 kyr emplacement duration, with the astrochronologically determined timing and duration of hiatuses (totaling ~600 ka) supported by U-Pb zircon dates. Similarly, Schoene et al. (2019) propose Deccan Traps emplacement occurred in four high-output pulses, with durations ranging from 50 to 200 ka, while Kasbohm and Schoene (2018) suggest that the emplacement of the Wapshilla Ridge Member of the CRBG, which makes up 20% of the total LIP volume, likely occurred over tens of ka. In the Siberian Traps, a study of magnetic secular variation suggests that a large portion of magma was emplaced in as little as ~10 ka, though this estimate does not take into account the length of hiatuses (Pavlov et al., 2019). Models for pulsed eruptions of LIPs need to be tested with additional geochronology from a broader area to test whether the apparent hiatuses are simply changes in depositional locations or eruptive center migration. This is a challenge given the large geographic distribution of LIPs and also variable preservation.

2.3.2. Correlation Of LIP Magmatism With Environmental Change and Biotic Extinctions

While a broad temporal overlap of LIPs and environmental perturbations was once sufficient to hypothesize a causal relationship (e.g., Courtillot & Renne, 2003), progressively higher precision geochronology of LIPs and their corresponding crises has enabled a more detailed interrogation of this hypothesis. In Figure 2.2, we present the relative timing (zero is set as the age or midpoint timing of environmental event) and total duration of each event, incorporating the most recent geochronology (with 2σ uncertainty). This visualization shows the progress made in assessing the relative timing of these events and the plausibility of a causal connection, as well as fruitful areas to pursue future work. While all of the pairs of events show temporal overlap, for many, uncertain age constraints on at least one of the events hinders the assessment of the possible effects of LIP emplacement. A minority of pairs have high-precision age constraints for both events: Siberian Traps/end-Permian Extinction, CAMP/end-Triassic Extinction, Deccan Traps/end-Cretaceous Extinction, and the CRBG/MCO. The CRBG and MCO show the as-yet unique relationship of the climate event apparently beginning before LIP volcanism, though it is necessary to obtain absolute age constraints on the MCO in addition to its current astronomical calibration. If the MCO were shown to begin before CRBG emplacement, it would suggest that either other processes, such as changing ocean circulation patterns and fluctuations in the East Antarctic Ice Sheet, were more important in driving the MCO (Foster et al., 2012; Holbourn et al., 2014), or that cryptic degassing of the CRBG affected climate prior to the start of extrusive volcanism (Kasbohm & Schoene, 2018). Efforts to find evidence for cryptic degassing in other LIPs are described in the following section and could be applied to the CRBG.

For the other three couplets (Siberian Traps, CAMP, and Deccan), geochronology suggests emplacement beginning ~100–300 ka prior to the onset of corresponding extinction. For the Siberian Traps, Svensen et al. (2009) propose that the most lethal aspect of the LIP was widespread sill emplacement into an organic-rich sedimentary basin, and Burgess et al. (2017) observe that the end-Permian extinction coincides with the beginning of emplacement Stage 2, dominated by sill emplacement. For the CAMP, the timing of the first intrusive emplacement in western Africa and sill emplacement into an organic-rich basin in Brazil also overlaps with the end-Triassic Extinction (Davies et al., 2017; Heimdal et al., 2018). In the Deccan Traps, Schoene et al. (2019) resolve the largest pulse of Deccan volcanism immediately before the end-Cretaceous mass extinction, suggesting that the LIP may have played a role, along with the Chicxulub impact, in creating catastrophic conditions for the biosphere. The Deccan Traps emplacement and the K-Pg event do not adhere to the model of Burgess et al. (2017), which argues that the emplacement of sills into a volatile-rich sedimentary basin makes a LIP deadly, rather than voluminous extrusive volcanism or dike emplacement. A significant volume of intrusive rocks have not been described, and the rocks through which the Deccan was emplaced are not obviously volatile-rich relative to those of the Siberian Traps, leading Burgess et al. (2017) to suggest that the Chicxulub impact would have played an equal if not greater role in causing the extinction as Deccan emplacement. Alternatively, the pronounced increase in Deccan effusion rate just prior to extinction (Schoene et al., 2019) would have been accompanied by more rapid loading of deadly gases into the atmosphere, potentially creating high-stress conditions immediately prior to the Chicxulub impact.

Broadly, Figure 2.2 and the information reviewed above allow LIP–environmental crisis couplets to be divided into three groups: (1) LIPs connected to mass extinctions (Kalkarindji, Yakutsk-Vilyui, Emeishan, Siberian, CAMP, Deccan); (2) LIPs associated with oceanic anoxic events (Karoo-Ferrar, OJP, Caribbean LIP); and (3) LIPs related to global climate perturbations without mass extinction or oceanic anoxic events (Franklin, NAIP, CRBG). With existing data sets, it is premature to develop a single general model describing why certain LIPs drive specific environmental feedbacks. For example, LIP size doesn't seem a uniquely deadly trait, as the largest LIP, OJP, was not the most deadly to the biosphere, though its underwater emplacement seems to have disrupted ocean chemistry (Naafs et al., 2016). Nor is duration a unique indicator of deadliness, as the CRBG is of comparable life span to the Siberian Traps, CAMP, and Deccan Traps, but is not related to a mass extinction, though it is disputed whether the Deccan Traps played a role in the end-Cretaceous extinction. In every case, the duration of LIP volcanism continues beyond the age of the extinction, indicating that the simple presence of magmatic activity is insufficient to create lasting climatic distress; other aspects of LIP emplacement, such as effusion rate or emplacement style, are likely to drive the short-lived perturbations. While the Franklin LIP's original location in the tropics is hypothesized to be a necessary condition for the onset of the Sturtian Snowball Earth through CO_2 drawdown via silicate weathering (Goddéris et al., 2003; Macdonald et al., 2010; Youbi et al., Chapter 8 this volume), this mechanism does not explain why larger LIPs that were emplaced at the equator (Kalkarindji LIP, CAMP, Caribbean LIP, Deccan Traps) did not also cause similarly dramatic global cooling events (Park et al., Chapter 7 this volume). It is likely that the effect a LIP had on the climate and biosphere is at least partly a reflection of the weaknesses inherited in that particular climate or ecosystem state, which have yet to be fully

characterized. Further high-precision geochronology in conjunction with development of paleoclimate and biostratigraphic records, and a better understanding of the causes, isotopic composition, and quantity of volatile release (Mather & Schmidt, Chapter 4 this volume), will be necessary to improve our understanding of the temporal connection between LIPs and their corresponding environmental catastrophes.

2.4. CHALLENGES AND FUTURE OPPORTUNITIES

Geological limitations to improving LIP geochronology occur on macroscopic and microscopic scales. At the macroscopic scale, there is a limit to stratigraphically comprehensive sample collection due to access (particularly for oceanic LIPs), and in some cases, to erosive or depositional processes, which may eliminate much of the LIP stratigraphy from the rock record. At the microscopic scale, obtaining precise geochronology depends on finding the necessary minerals. $^{40}Ar/^{39}Ar$ studies require unaltered minerals, and even when ideal minerals are isolated, can still be hindered by a lack of radiogenic parent isotope and therefore low precision. While U-Pb ID-TIMS zircon studies yield ages with greater precision, they can only be applied to LIPs from which zircons can be extracted from gabbroic segregations or interbedded ashes. A promising approach to improving the precision of $^{40}Ar/^{39}Ar$ geochronology of LIPs may also lie in targeting interbedded ash deposits that contain K-feldspar, which can yield much higher precision than plagioclase (Mahood & Benson, 2017), though it may be prone to similar issues of pre-eruptive residence time as seen in zircon geochronology of ashes (Andersen et al., 2017).

For many LIPs, these geological limitations have impeded the calculation of magmatic volumes and the creation of a detailed timeline for eruptions across the original horizontal extent of the LIP and the vertical stratigraphy of eruptions. For example, the limited exposure and relatively low-precision ages of the Kalkarindji LIP make it difficult to ascertain the overall duration of volcanism and the total volume emplaced; current geochronology permits this LIP to have erupted rapidly for over ~10 Ma (Fig. 2.2). Well-established stratigraphies based on geochemistry and magnetic polarity of the basalts have been constructed for only a minority of LIPs (e.g., Siberian Traps, CAMP, Deccan Traps, CRBG), as both widespread exposure and somewhat complete vertical sections remain for these events. Without this detail, however, it is difficult to assess volumetric eruptive rates, which may be as important as overall emplacement volume to the environmental impact of LIPs.

Geological limitations may also affect the age calibration of environmental events, as radiometric dating of these events would require volcanic ash deposition in the middle of the sedimentary successions in which they are recorded, which is rarely the case. Future geochronological studies of environmental crises would also benefit from a horizontal approach, which would assess the synchroneity of an event across different geographic locations (e.g., Baresel et al., 2017a, 2017b; Schoene et al., 2010), as well as a vertical approach, which would provide a greater number of dates constraining not only an extinction horizon, but also any biogeochemical or paleoecological changes that occur before or after that horizon (e.g., Maclennan et al., 2018; Shen et al., 2018; Du Vivier et al., 2015). When radiometric dating cannot be used to constrain the timing of environmental events, astronomical tuning methods may be effectively used to obtain age models, specifically in the Cenozoic for events like the MCO (Kochhann et al., 2016). Improving assessments of the timing, duration, and synchrony of these events at a global scale will yield not only greater insights into their connection to LIP emplacement, but also better temporal constraints to calibrate future versions of the Geologic Time Scale.

Overcoming analytical limitations will also be necessary to provide more detailed assessments of the timescales of LIP eruption and environmental change. Even with methodological advances yielding U-Pb zircon ages with precision to better than ± 0.1%, this resolution is inadequate to address the relative order of LIPs and climatic perturbations that are several hundred Ma old. For younger LIPs, such as the Deccan Traps and CRBG, with geochronological uncertainty on the order of 10–30 ka, a more nuanced account of LIP eruptions can be generated, which indicates rapid pulses of voluminous eruptions and periods of relatively slow, or quiescent eruptions (Kasbohm & Schoene, 2018; Schoene et al., 2019). If analytical limits to absolute precision for eruption and emplacement dates can be overcome, it might be possible to observe such pulsed volcanism in older LIPs.

With new high-precision geochronology improving age constraints on both LIP emplacement and environmental perturbations, demonstrating a simple age overlap for event couplets is insufficient to assess whether or not LIPs play a causative role in these events. Instead, it becomes essential to consider the timing and timescales of different climatic effects of LIPs that may not be recorded in the rock record, such as volatile, aerosol, and particulate release, acid rain, and ozone depletion, and how these are temporally related to intrusive and extrusive LIP emplacement. The effects of ozone depletion from Cl_2, acid rain, and cooling due to sulfate aerosols occur on the timescales of months to years (Wignall, 2001), far below both the analytical precision of today's most precise radiometric ages and the typical temporal resolution of the rock record. The environmental effects of CO_2 release, evident on 10 ka–100 ka timescales (Wignall, 2001) may be more easily captured by pCO_2

proxy records and compared to LIP emplacement age models with 10 ka–100 ka resolution. With this resolution already obtained, these age models provide crucial temporal constraints for researchers seeking to model the environmental effects of LIP volcanism.

To constrain the timing of CO_2 liberation from LIPs, it may be possible to date rocks that show geological evidence for degassing. For example, Svensen et al. (2010) performed U-Pb zircon geochronology on NAIP sills sampled in drill cores offshore Norway, which contained contact aureoles indicative of violent gas release from organic-rich host sediments, as well as a connection to hydrothermal vent complexes; these ages thereby constrain the timing of degassing. Obtaining ages for other intrusive units in contact with metamorphosed organic-rich sediments, for which studies have modeled the amount of CO_2 and methane released (Aarnes et al., 2011; Ganino & Arndt, 2009), would be a fruitful target for future geochronology. Stratigraphic proxy records, such as Hg concentration in sediments (Percival et al., Chapter 11 this volume) and osmium isotope records (Bottini et al., 2012; Dickson et al., Chapter 10 this volume; Tejada et al., 2009; Turgeon & Creaser, 2008; Du Vivier et al., 2014), are proving to be promising for identifying volcanic episodes in sedimentary basins that are distant from LIPs.

The goal of this review was to show how high-precision geochronology has progressively reinforced and refined temporal correlations between LIP emplacement and global environmental perturbations, and to seek out patterns in LIP eruption that may suggest when and how LIPs directly trigger these perturbations. The relative efficacy of various LIP characteristics (area, volume, effusion rate, host rock composition) in driving situational change is dependent on a number of factors, paramount of which is accurately knowing the timing and duration of both events to a level of precision on par or better than the durations of the events themselves. As discussed, this has been and continues to be a main goal of the broader geochronologic community. Without accurate and precise dates and rates, the detailed role of LIPs in driving environmental change, and why some LIPs are more deadly than others, will remain frustratingly opaque.

ACKNOWLEDGMENTS

We thank Richard Ernst for inviting our participation in this volume and for great editorial support and extreme patience as we prepared this manuscript. Constructive reviews by Lawrence Percival, Josh Davies, and Mark Stelten improved the quality of the manuscript. We would also like to thank Sam Bowring, who as a leader in the field of geochronology worked tirelessly to push the accuracy and precision of geochronometers to new levels. His work, embraced by the LIP and mass extinction research communities, has led to unprecedented clarity on when and how volcanism and environmental change are linked, and has, as a result, begged questions of incredible detail and nuance that future workers endeavor to answer. We owe Sam a great debt of gratitude for the leadership and mentorship he has shown us. The benefits of his work to the broader community striving to understand links between the geosphere and biosphere are immeasurable. Any use of trade, firm, or product names is for descriptive purposes only and does not imply endorsement by the U.S. Government.

REFERENCES

Aarnes, I., Svensen, H. H., Polteau, S., & Planke, S. (2011). Contact metamorphic devolatilization of shales in the Karoo Basin, South Africa, and the effects of multiple sill intrusions. *Chemical Geology*. https://doi.org/10.1016/j.chemgeo.2010.12.007

Algeo, T. J., & Scheckler, S. E. (1998). Terrestrial-marine teleconnections in the Devonian: Links between the evolution of land plants, weathering processes, and marine anoxic events. *Philosophical Transactions of the Royal Society of London. Series B: Biological Sciences*, *353*(1365), 113–130. https://doi.org/10.1098/rstb.1998.0195

Ali, J. R., Thompson, G. M., Song, X., & Wang, Y. (2002). Emeishan basalts (SW China) and the "end-Guadalupian" crisis: magnetobiostratigraphic constraints. *Journal of the Geological Society*. https://doi.org/10.1144/0016-764901086

Allègre, C. J., Birck, J. L., Capmas, F., & Courtillot, V. E. (1999). Age of the Deccan traps using ^{187}Re-^{187}Os systematics. *Earth and Planetary Science Letters*, *170*(3), 197–204. https://doi.org/10.1016/S0012-821X(99)00110-7

Al-Suwaidi, A. H., Angelozzi, G. N., Baudin, F., Damborenea, S. E., Hesselbo, S. P., Jenkyns, H. C., et al. (2010). First record of the Early Toarcian oceanic anoxic event from the Southern Hemisphere, Neuquén Basin, Argentina. *Journal of the Geological Society*, *167*(4), 633–636. https://doi.org/10.1144/0016-76492010-025

Andersen, N. L., Jicha, B. R., Singer, B. S., & Hildreth, W. (2017). Incremental heating of Bishop Tuff sanidine reveals preeruptive radiogenic Ar and rapid remobilization from cold storage. *Proceedings of the National Academy of Sciences of the United States of America*, *114*(47), 12407–12412. https://doi.org/10.1073/pnas.1709581114

Antonini, P. (1998). A late episode of Ferrar magmatism? Geochemistry and preliminary ^{40}Ar/^{39}Ar results of high Fe (SPCT) tholeiites from Southern Victoria Land, Antarctica. *Mineralogical Magazine*, *62A*(1), 63–64. https://doi.org/10.1180/minmag.1998.62a.1.33

Armstrong McKay, D. I., Tyrrell, T., Wilson, P. A., & Foster, G. L. (2014). Estimating the impact of the cryptic degassing of Large Igneous Provinces: A mid-Miocene case-study. *Earth and Planetary Science Letters*, *403*, 254–262. https://doi.org/10.1016/j.epsl.2014.06.040

Baksi, A. K. (1994). Geochronological studies on whole-rock basalts, Deccan Traps, India: evaluation of the timing of

volcanism relative to the K-T boundary. *Earth and Planetary Science Letters*, *121*(1–2), 43–56. https://doi.org/10.1016/0012-821X(94)90030-2

Baksi, A. K. (2014). $^{40}Ar/^{39}Ar$ ages of flood basalt provinces in Russia and China and their possible link to global faunal extinction events: A cautionary tale regarding alteration and loss of $^{40}Ar^*$. *Journal of Asian Earth Sciences.* https://doi.org/10.1016/j.jseaes.2013.07.029

Baksi, A. K., & Archibald, D. A. (1997). Mesozoic igneous activity in the Maranhão province, northern Brazil: $^{40}Ar/^{39}Ar$ evidence for separate episodes of basaltic magmatism. *Earth and Planetary Science Letters*, *151*(3–4), 139–153.

Baksi, A. K., & Farrar, E. (1991). $^{40}Ar/^{39}Ar$ dating of the Siberian Traps, USSR: Evaluation of the ages of the two major extinction events relative to episodes of flood-basalt volcanism in the USSR and the Deccan Traps, *India. Geology.* https://doi.org/10.1130/0091-7613(1991)019<0461:ADOTST>2.3.CO

Baresel, B., Bucher, H., Bagherpour, B., Brosse, M., Guodun, K., & Schaltegger, U. (2017b). Timing of global regression and microbial bloom linked with the Permian-Triassic boundary mass extinction: Implications for driving mechanisms. *Scientific Reports*, *7*(43630), 1–8. https://doi.org/10.1038/srep43630

Baresel, B., D'Abzac, F. X., Bucher, H., & Schaltegger, U. (2017a). High-precision time-space correlation through coupled apatite and zircon tephrochronology: An example from the Permian-Triassic boundary in South China. *Geology*, *45*(1), 83–86. https://doi.org/10.1130/G38181.1

Barnet, J. S. K., Littler, K., Kroon, D., Leng, M. J., Westerhold, T., Röhl, U., & Zachos, J. C. (2017). A new high-resolution chronology for the late Maastrichtian warming event: Establishing robust temporal links with the onset of Deccan volcanism. *Geology*, *46*(2), 147–150. https://doi.org/10.1130/G39771.1

Barry, T. L., Kelley, S. P., Camp, V. E., Self, S., Jarboe, N. A., & Duncan, R. A. (2013). Eruption chronology of the Columbia River Basalt Group. *Geological Society of America Special Paper*, *497*, 45–66. https://doi.org/10.1130/2013.2497(02).

Basu, A. R., Poreda, R. J., Renne, P. R., Teichmann, F., Vasiliev, Y. R., Sobolev, N. V., et al. (1995). High ^{3}He plume origin and temporal-spatial evolution of the Siberian flood basalts. *Science*, *269*(5225), 822–825. https://doi.org/10.1126/science.269.5225.822

Beane, J. E., Turner, C. A., Hooper, P. R., Subbarao, K. V., & Walsh, J. N. (1986). Stratigraphy, composition and form of the Deccan basalts, Western Ghats, India. *Bulletin of Volcanology*, *48*(1), 61–83. https://doi.org/10.1007/BF01073513

Becker, T. R., Gradstein, F. M., & Hammer, Ø. (2012). The Devonian Period. In *The Geologic Time Scale 2012*. https://doi.org/10.1016/B978-0-444-59425-9.00022-6

Bertrand, H. (1991). The Mesozoic Tholeiitic Province of northwest Africa: A volcano-tectonic record of the early opening of central Atlantic. In *Magmatism in extensional structural settings* (pp. 147–188). Berlin, Heidelberg: Springer Berlin Heidelberg. https://doi.org/10.1007/978-3-642-73966-8_7

Besse, J., & Courtillot, V. E. (1988). Paleogeographic maps of the continents bordering the Indian Ocean since the Early Jurassic. *Journal of Geophysical Research: Solid Earth*, *93*(B10), 11791–11808. https://doi.org/10.1029/JB093iB10p11791

Billups, K., Pälike, H., Channell, J. E. T., Zachos, J. C., & Shackleton, N. J. (2004). Astronomic calibration of the late Oligocene through early Miocene geomagnetic polarity time scale. *Earth and Planetary Science Letters*, *224*(1–2), 33–44. https://doi.org/10.1016/j.epsl.2004.05.004

Black, B. A., & Manga, M. (2017). Volatiles and the tempo of flood basalt magmatism. *Earth and Planetary Science Letters*, *458*, 130–140. https://doi.org/10.1016/J.EPSL.2016.09.035

Black, B. A., Neely, R. R., Lamarque, J. F., Elkins-Tanton, L. T., Kiehl, J. T., Shields, C. A., et al. (2018). Systemic swings in end-Permian climate from Siberian Traps carbon and sulfur outgassing. *Nature Geoscience.* https://doi.org/10.1038/s41561-018-0261-y

Blackburn, T. J., Olsen, P. E., Bowring, S. A., McLean, N. M., Kent, D. V., Puffer, J. H., et al. (2013). Zircon U-Pb geochronology links the end-Triassic extinction with the Central Atlantic magmatic province. *Science.* https://doi.org/10.1126/science.1234204

Böhme, M. (2003). The Miocene Climatic Optimum: Evidence from ectothermic vertebrates of central Europe. *Palaeogeography, Palaeoclimatology, Palaeoecology*, *195*(3–4), 389–401. https://doi.org/10.1016/S0031-0182(03)00367-5

Bottini, C., Cohen, A. S., Erba, E., Jenkyns, H. C., & Coe, A. L. (2012). Osmium-isotope evidence for volcanism, weathering, and ocean mixing during the early Aptian OAE 1a. *Geology*, *40*(7), 583–586. https://doi.org/10.1130/G33140.1

Boulila, S., Galbrun, B., Huret, E., Hinnov, L. A., Rouget, I., Gardin, S., & Bartolini, A. (2014). Astronomical calibration of the Toarcian stage: Implications for sequence stratigraphy and duration of the early Toarcian OAE. *Earth and Planetary Science Letters*, *386*, 98–111. https://doi.org/10.1016/j.epsl.2013.10.047

Bowring, W. A., Grotzinger, J. P., Condon, D. J., Ramezani, J., Newall, M. J., & Allen, P. A. (2007). Geochronologic constraints on the chronostratigraphic framework of the Neoproterozoic Huqf Supergroup, Sultanate of Oman. *American Journal of Science 307*(10), 1097–1145. doi: 10.275;10.2007.01

Bowring, J. F., McLean, N. M., & Bowring, S. A. (2011). Engineering cyber infrastructure for U-Pb geochronology: Tripoli and U-Pb-Redux. *Geochemistry, Geophysics, Geosystems*, *12*(6). https://doi.org/10.1029/2010GC003479

Bowring, S. A., Erwin, D. H., Jin, Y. G., Martin, M. W., Davidek, K. L., & Wang, W. (1998). U/Pb zircon geochronology and tempo of the end-Permian mass extinction. *Science.* https://doi.org/10.1126/science.280.5366.1039

Brewer, T. S., Rex, D., Guise, P. G., & Hawkesworth, C. J. (1996). Geochronology of the Mesozoic tholeiitic magmatism in Antarctica: implications for the development of the failed Weddell Sea rift system. *Geological Society Special Publication*, *108*, 45–61. https://doi.org/10.1144/GSL.SP.1996.108.01.04

Bryan, S. E., & Ferrari, L. (2013). Large igneous provinces and silicic large igneous provinces: Progress in our understanding over the last 25 years. *Bulletin of the Geological Society of America.* https://doi.org/10.1130/B30820.1

Buck, C. E., Kenworthy, J. B., Litton, C. D., & Smith, A. F. M. (1991). Combining archaeological and radiocarbon information:

A Bayesian approach to calibration. *Antiquity*, *65*(249), 808–821. https://doi.org/10.1017/S0003598X00080534

Burgess, S. D., & Bowring, S. A. (2015). High-precision geochronology confirms voluminous magmatism before, during, and after Earth's most severe extinction. *Science Advances*, *1*(7), e1500470–e1500470. https://doi.org/10.1126/sciadv.1500470

Burgess, S. D., Bowring, S. A., & Shen, S. (2014). High-precision timeline for Earth's most severe extinction. *Proceedings of the National Academy of Sciences of the United States of America*, *111*(9), 3316–21. https://doi.org/10.1073/pnas.1317692111

Burgess, S. D., Bowring, S. A., Fleming, T. H., & Elliot, D. H. (2015). High-precision geochronology links the Ferrar large igneous province with early-Jurassic ocean anoxia and biotic crisis. *Earth and Planetary Science Letters*, *415*, 90–99. https://doi.org/10.1016/j.epsl.2015.01.037

Burgess, S. D., Muirhead, J. D., & Bowring, S. A. (2017). Initial pulse of Siberian Traps sills as the trigger of the end-Permian mass extinction. *Nature Communications*, *8*(1), 164. https://doi.org/10.1038/s41467-017-00083-9

Callegaro, S., Marzoli, A., Bertrand, H., Blichert-Toft, J., Reisberg, L., Cavazzini, G., et al. (2017). Geochemical constraints provided by the Freetown Layered Complex (Sierra Leone) on the origin of high-ti tholeiitic CAMP magmas. *Journal of Petrology*, *58*(9), 1811–1840. https://doi.org/10.1093/petrology/egx073

Camp, V. E. (2013). Origin of Columbia River basalt: Passive rise of shallow mantle, or active upwelling of a deep-mantle plume? *Geological Society of America Special Paper*, *497*, 181–199. https://doi.org/10.1130/2013.2497(07).

Campbell, I. H., Czamanske, G. K., Fedorenko, V. A., Hill, R. I., & Stepanov, V. (1992). Synchronism of the Siberian Traps and the Permian-Triassic boundary. *Science*, *258*(5089), 1760–173. https://doi.org/10.1126/science.258.5089.1760

Chambers, L. M., Pringle, M. S., & Fitton, J. G. (2002). Age and duration of magmatism on the Ontong Java plateau: ^{40}Ar-^{39}Ar results from ODP Leg 192. In *American Geophysical Union Fall Meeting Abstracts* (pp. V71B–1271).

Chambers, L. M., Pringle, M. S., & Fitton, J. G. (2004). Phreatomagmatic eruptions on the Ontong Java plateau: An Aptian ^{40}Ar/^{39}Ar age for volcaniclastic rocks at ODP Site 1184. *Geological Society Special Publication*, *229*, 325–331. https://doi.org/10.1144/GSL.SP.2004.229.01.18

Chambers, L. M., Pringle, M. S., & Parrish, R. R. (2005). Rapid formation of the Small Isles Tertiary centre constrained by precise ^{40}Ar/^{39}Ar and U-Pb ages. *Lithos*, *79*, 367–384.

Channell, J. E. T., Erba, E., Nakanishi, M., & Tamaki, K. (1995). Late Jurassic-early Cretaceous time scales and oceanic magnetic anomaly block models. *Geochronology, Time Scales and Global Stratigraphic Correlation*.

Channell, J. E. T., Galeotti, S., Martin, E. E., Billups, K., Scher, H. D., & Stoner, J. S. (2003). Eocene to Miocene magnetostratigraphy, biostratigraphy, and chemostratigraphy at ODP site 1090 (sub-Antarctic South Atlantic). *Bulletin of the Geological Society of America*, *115*(5), 607–623. https://doi.org/10.1130/0016-7606(2003)115<0607:ETMMBA>2.0.CO;2

Charles, A. J., Condon, D. J., Harding, I. C., Pälike, H., Marshall, J. E. A., Cui, Y., et al. (2011). Constraints on the numerical age of the Paleocene-Eocene boundary. *Geochemistry, Geophysics, Geosystems, 12*(6). https://doi.org/10.1029/2010GC003426

Charlier, B., & Zellmer, G. (2000). Some remarks on U-Th mineral ages from igneous rocks with prolonged cystallisation histories. *Earth and Planetary Science Letters*, *183*(3–4), 457–469. https://doi.org/10.1016/S0012-821X(00)00298-3

Chen, B., Joachimski, M. M., Sun, Y., Shen, S., & Lai, X. (2011). Carbon and conodont apatite oxygen isotope records of Guadalupian-Lopingian boundary sections: Climatic or sea-level signal? *Palaeogeography, Palaeoclimatology, Palaeoecology*, *311*(3–4), 145–153. https://doi.org/10.1016/j.palaeo.2011.08.016

Chenet, A.-L., Courtillot, V. E., Fluteau, F. F., Gérard, M., Quidelleur, X., Khadri, S. F. R., et al. (2009). Determination of rapid Deccan eruptions across the Cretaceous-Tertiary boundary using paleomagnetic secular variation: 2. Constraints from analysis of eight new sections and synthesis for a 3,500-m-thick composite section. *Journal of Geophysical Research: Solid Earth*, *114*(6). https://doi.org/10.1029/2008JB005644

Chenet, A.-L., Fluteau, F. F., Courtillot, V. E., Gérard, M., & Subbarao, K. V. (2008). Determination of rapid Deccan eruptions across the Cretaceous-Tertiary boundary using paleomagnetic secular variation: Results from a 1,200-m-thick section in the Mahabaleshwar escarpment. *Journal of Geophysical Research*, *113*(B4). https://doi.org/10.1029/2006jb004635

Chenet, A.-L., Quidelleur, X., Fluteau, F. F., Courtillot, V. E., & Bajpai, S. (2007). ^{40}K-^{40}Ar dating of the main Deccan large igneous province: Further evidence of KTB age and short duration. *Earth and Planetary Science Letters*, *263*(1–2), 1–15. https://doi.org/10.1016/j.epsl.2007.07.011

Cirilli, S., Marzoli, A., Tanner, L. H., Bertrand, H., Buratti, N., Jourdan, F., et al. (2009). Latest Triassic onset of the Central Atlantic Magmatic Province (CAMP) volcanism in the Fundy basin (Nova Scotia): New stratigraphic constraints. *Earth and Planetary Science Letters*, *286*(3–4), 514–525. https://doi.org/10.1016/j.epsl.2009.07.021

Clyde, W. C., Ramezani, J., Johnson, K. R., Bowring, S. A., & Jones, M. M. (2016). Direct high-precision U-Pb geochronology of the end-Cretaceous extinction and calibration of Paleocene astronomical timescales. *Earth and Planetary Science Letters*, *452*, 272–280. https://doi.org/10.1016/j.epsl.2016.07.041

Condon, D. J., Schoene, B., McLean, N. M., Bowring, S. A., & Parrish, R. R. (2015). Metrology and traceability of U-Pb isotope dilution geochronology (EARTHTIME Tracer Calibration Part I). *Geochimica et Cosmochimica Acta*, *164*, 464–480. https://doi.org/10.1016/j.gca.2015.05.026

Corfu, F., Polteau, S., Planke, S., Faleide, J. I., Svensen, H. H., Zayoncheck, A., & Stolbov, N. (2013). U-Pb geochronology of Cretaceous magmatism on Svalbard and Franz Josef Land, Barents Sea Large Igneous Province. *Geological Magazine*, *150(*6), 1127–1135. https://doi.org/10.1017/S0016756813000162

Corfu, F., Svensen, H. H., & Mazzini, A. (2016). Comment to paper: Evaluating the temporal link between the Karoo LIP

and climatic-biologic events of the Toarcian Stage with high-precision U-Pb geochronology by Bryan Sell, Maria Ovtcharova, Jean Guex, Annachiara Bartolini, Fred Jourdan, Jorge E. Spangen. *Earth and Planetary Science Letters*, *434*, 349–352. https://doi.org/10.1016/j.epsl.2015.07.010

Courtillot, V. E., & Renne, P. R. (2003). On the ages of flood basalt events. *Comptes Rendus Geoscience*, *335*(1), 113–140. https://doi.org/10.1016/S1631-0713(03)00006-3

Courtillot, V. E., Besse, J., Vandamme, D., Montigny, R., Jaeger, J.-J., & Cappetta, H. (1986). Deccan flood basalts at the Cretaceous/Tertiary boundary? *Earth and Planetary Science Letters*, *80*(3–4), 361–374. https://doi.org/http://dx.doi.org/10.1016/0012-821X(86)90118-4

Courtillot, V. E., Feraud, G., Maluski, H., Vandamme, D., Moreau, M. G., & Besse, J. (1988). Deccan flood basalts and the Cretaceous/Tertiary boundary. *Nature*, *333*(6176), 843–846. Retrieved from http://dx.doi.org/10.1038/333843a0

Courtillot, V. E., Gallet, Y., Rocchia, R., Féraud, G., Robin, E., Hofmann, C., et al. (2000). Cosmic markers, 40Ar/39Ar dating and paleomagnetism of the KT sections in the Anjar Area of the Deccan large igneous province. *Earth and Planetary Science Letters*, *182*(2), 137–156. https://doi.org/10.1016/S0012-821X(00)00238-7

Courtillot, V. E., Kravchinsky, V. A., Quidelleur, X., Renne, P. R., & Gladkochub, D. P. (2010). Preliminary dating of the Viluy traps (Eastern Siberia): Eruption at the time of Late Devonian extinction events? *Earth and Planetary Science Letters*, *300(*3–4), 239–245. https://doi.org/10.1016/j.epsl.2010.09.045

Cox, G. M., Strauss, J. V., Halverson, G. P., Schmitz, M. D., McClelland, W. C., Stevenson, R. S., & Macdonald, F. A. (2015). Kikiktat volcanics of Arctic Alaska: Melting of harzburgitic mantle associated with the Franklin large igneous province. *Lithosphere.* https://doi.org/10.1130/L435.1

Cox, K. G. (1988). *The Karoo Province*. *Springer, Dordrecht.* https://doi.org/10.1007/978-94-015-7805-9_7

Cui, Y., Kump, L. R., Ridgwell, A. J., Charles, A. J., Junium, C. K., Diefendorf, A. F., et al. (2011). Slow release of fossil carbon during the Palaeocene-Eocene Thermal Maximum. *Nature Geoscience*, *4*(7), 481–485. https://doi.org/10.1038/ngeo1179

Dalrymple, G. B., Czamanske, G. K., Fedorenko, V. A., Simonov, O. N., Lanphere, M. A., & Likhachev, A. P. (1995). A reconnaissance $^{40}Ar^{39}Ar$ geochronologic study of ore-bearing and related rocks, Siberian Russia. *Geochimica et Cosmochimica Acta*, *59*(10), 2071–2083. https://doi.org/10.1016/0016-7037(95)00127-1

Davies, J. H. F. L., Marzoli, A., Bertrand, H., Youbi, N., Ernesto, M., & Schaltegger, U. (2017). End-Triassic mass extinction started by intrusive CAMP activity. *Nature Communications*, *8*, 15596. https://doi.org/10.1038/ncomms15596

Davis, D. W., Krogh, T. E., & Williams, I. S. (2003). Historical development of zircon geochronology. *Reviews in Mineralogy and Geochemistry*, *53*(1), 145–181. https://doi.org/10.2113/0530145

Davydov, V. I., Crowley, J. L., Schmitz, M. D., & Poletaev, V. I. (2010). High-precision U-Pb zircon age calibration of the global Carboniferous time scale and Milankovitch band cyclicity in the Donets basin, eastern Ukraine. *Geochemistry, Geophysics, Geosystems*, *11*(2). https://doi.org/10.1029/2009GC002736

Day, M. O., Ramezani, J., Bowring, S. A., Sadler, P. M., Erwin, D. H., Abdala, F., & Rubidge, B. S. (2015). When and how did the terrestrial mid-Permian mass extinction occur? Evidence from the tetrapod record of the Karoo Basin, South Africa. *Proceedings of the Royal Society B: Biological Sciences.* https://doi.org/10.1098/rspb.2015.0834

Deckart, K., Féraud, G., & Bertrand, H. (1997). Age of Jurassic continental tholeiites of French Guyana, Surinam and Guinea: Implications for the initial opening of the Central Atlantic Ocean. *Earth and Planetary Science Letters*, *150*(3–4), 205–220. https://doi.org/10.1016/S0012-821X(97)00102-7

Deenen, M. H. L., Ruhl, M., Bonis, N. R., Krijgsman, W., Kürschner, W. M., Reitsma, M., & van Bergen, M. J. (2010). A new chronology for the end-Triassic mass extinction. *Earth and Planetary Science Letters.* https://doi.org/10.1016/j.epsl.2010.01.003

Denyszyn, S. W., Halls, H. C., Davis, D. W., & Evans, D. A. D. (2009). Paleomagnetism and U-Pb geochronology of Franklin dykes in High Arctic Canada and Greenland: A revised age and paleomagnetic pole constraining block rotations in the Nares Strait region. *Canadian Journal of Earth Sciences*. https://doi.org/10.1139/E09-042

De Vleeschouwer, D., & Parnell, A. C. (2014). Reducing timescale uncertainty for the Devonian by integrating astrochronology and Bayesian statistics. *Geology*, *42*(6), 491–494. https://doi.org/10.1130/G35618.1

De Vleeschouwer, D., Da Silva, A. C., Sinnesael, M., Chen, D., Day, J. E., Whalen, M. T., et al. (2017). Timing and pacing of the Late Devonian mass extinction event regulated by eccentricity and obliquity. *Nature Communications.* https://doi.org/10.1038/s41467-017-02407-1

Dickens, G. R., O'Neil, J. R., Rea, D. K., & Owen, R. M. (1995). Dissociation of oceanic methane hydrate as a cause of the carbon isotope excursion at the end of the Paleocene. *Paleoceanography and Paleoclimatology*, *10*(6), 965–971. https://doi.org/10.1029/95PA02087

Duncan, R. A., & Pyle, D. G. (1988). Rapid eruption of the Deccan flood basalts at the Cretaceous/Tertiary boundary. *Nature*, *333*(6176), 841–843. Retrieved from http://dx.doi.org/10.1038/333841a0

Duncan, R. A., Hooper, P. R., Rehacek, J., Marsh, J. S., & Duncan, A. R. (1997). The timing and duration of the Karoo igneous event, southern Gondwana. *Journal of Geophysical Research: Solid Earth*, *102*(B8), 18127–18138. https://doi.org/10.1029/97JB00972

Dunning, G. R., & Hodych, J. P. (1990). U/Pb zircon and baddeleyite ages for the Palisades and Gettysburg sills of the northeastern United States: Implications for the age of the Triassic/Jurassic boundary. *Geology*, *18*(8), 795–798. https://doi.org/10.1130/0091-7613(1990)018<0795:UPZABA>2.3.CO;2

Du Vivier, A. D. C., Selby, D., Condon, D. J., Takashima, R., & Nishi, H. (2015). Pacific $^{187}Os/^{188}Os$ isotope chemistry and U-Pb geochronology: Synchroneity of global Os isotope change across OAE 2. *Earth and Planetary Science Letters.* https://doi.org/10.1016/j.epsl.2015.07.020

Du Vivier, A. D. C., Selby, D., Sageman, B. B., Jarvis, I., Gröcke, D. R., & Voigt, S. (2014). Marine $^{187}Os/^{188}Os$ isotope stratigraphy reveals the interaction of volcanism and ocean circulation during Oceanic Anoxic Event 2. *Earth and Planetary Science Letters*, *389*, 23–33. https://doi.org/10.1016/j.epsl.2013.12.024

Eldholm, O., & Grue, K. (1994). North Atlantic volcanic margins: Dimensions and production rates. *Journal of Geophysical Research: Solid Earth*, *99*(B2), 2955–2968. https://doi.org/10.1029/93JB02879

Elliot, D. H. (2013). The geological and tectonic evolution of the Transantarctic Mountains: A review. *Geological Society, London, Special Publications*, *381*(1), 7–35. https://doi.org/10.1144/SP381.14

Elliot, D. H., & Fleming, T. H. (2004). Occurrence and dispersal of magmas in the Jurassic Ferrar large igneous province, Antarctica. *Gondwana Research*, *7*(1), 223–227. https://doi.org/10.1016/S1342-937X(05)70322-1

Elliot, D. H., & Fleming, T. H. (2008). Physical volcanology and geological relationships of the Jurassic Ferrar Large Igneous Province, Antarctica. *Journal of Volcanology and Geothermal Research*, *172*(1–2), 20–37. https://doi.org/10.1016/j.jvolgeores.2006.02.016

Elliot, D. H., Felming, T. H., Kyle, P. R., & Foland, K. A. (1999). Long-distance transport of magmas in the Jurassic Ferrar Large Igneous Province, Antarctica. *Earth and Planetary Science Letters*, *167*(1–2), 89–104. https://doi.org/10.1016/S0012-821X(99)0023-0

Encarnación, J., Fleming, T. H., Elliot, D. H., & Eales, H. V. (1996). Synchronous emplacement of Ferrar and Karoo dolerites and the early breakup of Gondwana. *Geology*, *24*(6), 535. https://doi.org/10.1130/0091-7613(1996)024<0535:SEOFAK>2.3.CO;2

Erba, E. (1994). Nannofossils and superplumes: The Early Aptian "nannoconid crisis." *Paleoceanography*, *9*(3), 483–501. https://doi.org/10.1029/94PA00258

Ernst, R. E. (2014). *Large Igneous Provinces*. Cambridge University Press. https://doi.org/10.1017/CBO9781139025300

Ernst, R. E., & Youbi, N. (2017). How large igneous provinces affect global climate, sometimes cause mass extinctions, and represent natural markers in the geological record. *Palaeogeography, Palaeoclimatology, Palaeoecology*, *478*, 30–52.

Evins, L. Z., Jourdan, F., & Phillips, D. (2009). The Cambrian Kalkarindji Large Igneous Province: Extent and characteristics based on new $^{40}Ar/^{39}Ar$ and geochemical data. *Lithos*. https://doi.org/10.1016/j.lithos.2009.01.014

Fitton, J. G., & Godard, M. (2004). Origin and evolution of magmas on the Ontong Java plateau. *Geological Society, London, Special Publications*, *229*(1), 151–178. https://doi.org/10.1144/GSL.SP.2004.229.01.10

Fleming, T. H., Heimann, A., Foland, K. A., & Elliot, D. H. (1997). $^{40}Ar/^{39}Ar$ geochronology of Ferrar Dolerite sills from the Transantarctic Mountains, Antarctica: Implications for the age and origin of the Ferrar magmatic province. *Geological Society of America Bulletin*, 109. https://doi.org/10.1130/0016-7606(1997)109<0533:AAGOFD>2.3.CO;2

Foland, K. A., Fleming, T. H., Heimann, A., & Elliot, D. H. (1993). Potassium-argon dating of fine-grained basalts with massive Ar loss: Application of the $^{40}Ar^{39}Ar$ technique to plagioclase and glass from the Kirkpatrick Basalt, Antarctica. *Chemical Geology*, *107*(1–2), 173–190. https://doi.org/10.1016/0009-2541(93)90109-V

Foster, G. L., Lear, C. H., & Rae, J. W. B. (2012). The evolution of pCO_2, ice volume and climate during the middle Miocene. *Earth and Planetary Science Letters*, *341–344*, 243–254. https://doi.org/10.1016/j.epsl.2012.06.007

Fraser, G. L., Pattison, D. R. M., & Heaman, L. M. (2004). Age of the Ballachulish and Glencoe igneous complexes (Scottish Highlands), and paragenesis of zircon, monazite and baddeleyite in the Ballachulish Aureole. *Journal of the Geological Society*, *161*(3), 447–462. https://doi.org/10.1144/0016-764903-018

Ganino, C., & Arndt, N. T. (2009). Climate changes caused by degassing of sediments during the emplacement of large igneous provinces. *Geology*. https://doi.org/10.1130/G25325A.1

Generød, M., Chew, D. M., Smethurst, M. A., Troll, V. R., Corfu, F., Meade, F., & Prestvik, T. (2011). Geochronology of the Tardree Rhyolite Complex, Northern Ireland: Implications for zircon fission track studies, the North Atlantic Igneous Province and the age of the Fish Canyon sanidine standard. *Chemical Geology, 286*(3–4), 224–228. https:// doi.org/10.1016/jchemgeo.2011.05.007

Glass, L. M., & Phillips, D. (2006). The Kalkarindji continental flood basalt province: A new Cambrian large igneous province in Australia with possible links to faunal extinctions. *Geology*. https://doi.org/10.1130/G22122.1

Goddéris, Y., Donnadieu, Y., Nédélec, A., Dupré, B., Dessert, C., Grard, A., et al. (2003). The Sturtian "snowball" glaciation: Fire and ice. *Earth and Planetary Science Letters*. https://doi.org/10.1016/S0012-821X(03)00197-3

Gozalo, R., Álvarez, M. E. D., Vintaned, J. A. G., Zhuravlev, A. Y., Bauluz, B., Subías, I., et al. (2013). Proposal of a reference section and point for the Cambrian Series 2-3 boundary in the Mediterranean subprovince in Murero (NE Spain) and its intercontinental correlation. *Geological Journal*. https://doi.org/10.1002/gj.1330

Guex, J., Bartolini, A., Atudorei, V., & Taylor, D. (2004). High-resolution ammonite and carbon isotope stratigraphy across the Triassic-Jurassic boundary at New York Canyon (Nevada). *Earth and Planetary Science Letters*, *225*(1–2), 29–41. https://doi.org/10.1016/j.epsl.2004.06.006

Guex, J., Schoene, B., Bartolini, A., Spangenberg, J. E., Schaltegger, U., O'Dogherty, L., et al. (2012). Geochronological constraints on post-extinction recovery of the ammonoids and carbon cycle perturbations during the Early Jurassic. *Palaeogeography, Palaeoclimatology, Palaeoecology*, *346–347*(0), 1–11.

Gutjahr, M., Ridgwell, A. J., Sexton, P. F., Anagnostou, E., Pearson, P. N., Pälike, H., et al. (2017). Very large release of mostly volcanic carbon during the Palaeocene-Eocene Thermal Maximum. *Nature*, *548*(7669), 573. https://doi.org/10.1038/nature23646

Hamilton, M. A., Pearson, D. G., Thompson, R. N., Kelley, S. P., & Emeleus, C. H. (1998). Rapid eruption of Skye lavas inferred from precise U-Pb and Ar-Ar dating of the Rum and Cuillin plutonic complexes. *Nature*, *394*(6690), 260–263. https://doi.org/10.1038/28361

Hargraves, R. B., Rehacek, J., & Hooper, P. R. (1997). Paleomagnetism of the Karoo igneous rocks in southern Africa. *South African Journal of Geology*, *100*(2), 195–212.

Harvey, T. H. P., Williams, M., Condon, D. J., Wilby, P. R., Siveter, D. J., Rushton, A. W. A., et al. (2011). A refined chronology for the Cambrian succession of southern Britain. *Journal of the Geological Society*. https://doi.org/10.1144/0016-76492010-031

Haslett, J., & Parnell, A. C. (2008). A simple monotone process with application to radiocarbon-dated depth chronologies. *Journal of the Royal Statistical Society. Series C: Applied Statistics*, *57*(4), 399–418. https://doi.org/10.1111/j.1467-9876.2008.00623.x

He, H., Pan, Y., Tauxe, L., Qin, H., & Zhu, R. (2008). Toward age determination of the M0r (Barremian-Aptian boundary) of the Early Cretaceous. *Physics of the Earth and Planetary Interiors*, *169*(1–4), 41–48. https://doi.org/10.1016/J.PEPI.2008.07.014

Heaman, L. M., & LeCheminant, A. N. (1993). Paragenesis and U-Pb systematics of baddeleyite (ZrO2). *Chemical Geology*, *110*(1–3), 95–126. https://doi.org/10.1016/0009-2541(93)90249-I

Heimann, A., Fleming, T. H., Elliot, D. H., & Foland, K. A. (1994). A short interval of Jurassic continental flood basalt volcanism in Antarctica as demonstrated by $^{40}Ar^{39}Ar$ geochronology. *Earth and Planetary Science Letters*, *121*, 19–41. https://doi.org/10.1016/0012-821X(94)90029-9

Heimdal, T. H., Svensen, H. H., Ramezani, J., Iyer, K., Pereira, E., Rodrigues, R., et al. (2018). Large-scale sill emplacement in Brazil as a trigger for the end-Triassic crisis. *Scientific Reports*, *8*(1), 141. https://doi.org/10.1038/s41598-017-18629-8

Henderson, C. M., Davydov, V. I., Wardlaw, B. R., Gradstein, F. M., & Hammer, Ø. (2012). *Chapter 24: The Permian Period. The geologic time scale*. https://doi.org/10.1016/B978-0-444-59425-9.00024-X

Henehan, M. J., Hull, P. M., Penman, D. E., Rae, J. W. B., & Schmidt, D. N. (2016). Biogeochemical significance of pelagic ecosystem function: An end-Cretaceous case study. *Philosophical Transactions of the Royal Society B*, *371*(1694), 20150510. https://doi.org/10.1098/rstb.2015.0510

Hesselbo, S. P., & Pienkowski, G. (2011). Stepwise atmospheric carbon-isotope excursion during the Toarcian Oceanic Anoxic Event (Early Jurassic, Polish basin). *Earth and Planetary Science Letters*, *301*(1–2), 365–372. https://doi.org/10.1016/j.epsl.2010.11.021

Hesselbo, S. P., Jenkyns, H. C., Duarte, L. V., & Oliveira, L. C. V. (2007). Carbon-isotope record of the Early Jurassic (Toarcian) Oceanic Anoxic Event from fossil wood and marine carbonate (Lusitanian basin, Portugal). *Earth and Planetary Science Letters*, *253*(3–4), 455–470. https://doi.org/10.1016/j.epsl.2006.11.009

Higgins, J. A., & Schrag, D. P. (2006). Beyond methane: Towards a theory for the Paleocene-Eocene thermal maximum. *Earth and Planetary Science Letters*, *245*(3–4), 523–537. https://doi.org/10.1016/j.epsl.2006.03.009

Hilgen, F. J., Lourens, L. J., Van Dam, J. A., Beu, A. G., Boyes, A. F., Cooper, R. A., et al. (2012). *Chapter 29: The Neogene Period. The geologic time scale* 2012. https://doi.org/10.1016/B978-0-444-59425-9.00029-9

Hodell, D. A., & Woodruff, F. (1994). Variations in the strontium isotopic ratio of seawater during the Miocene: Stratigraphic and geochemical implications. *Paleoceanography*, *9*(3), 405–426. https://doi.org/10.1029/94PA00292

Hofmann, C., Féraud, G., & Courtillot, V. E. (2000). $^{40}Ar/^{39}Ar$ dating of mineral separates and whole rocks from the Western Ghats lava pile: Further constraints on duration and age of the Deccan traps. *Earth and Planetary Science Letters*, *180*(1–2), 13–27. https://doi.org/http://dx.doi.org/10.1016/S0012-821X(00)00159-X

Holbourn, A., Kuhnt, W., Kochhann, K. G. D., Andersen, N., & Sebastian Meier, K. J. (2015). Global perturbation of the carbon cycle at the onset of the Miocene Climatic Optimum. *Geology*, *43*(2), 123–126. https://doi.org/10.1130/G36317.1

Holbourn, A., Kuhnt, W., Lyle, M., Schneider, L., Romero, O., & Andersen, N. (2014). Middle Miocene climate cooling linked to intensification of eastern equatorial Pacific upwelling. *Geology*, *42*(1), 19–22. https://doi.org/10.1130/G34890.1

Holbourn, A., Kuhnt, W., Schulz, M., Flores, J. A., & Andersen, N. (2007). Orbitally paced climate evolution during the middle Miocene "Monterey" carbon-isotope excursion. *Earth and Planetary Science Letters*. https://doi.org/10.1016/j.epsl.2007.07.026

Hooper, P. R., Widdowson, M., & Kelley, S. P. (2010). Tectonic setting and timing of the final Deccan flood basalt eruptions. *Geology*, *38*(9), 839–842. https://doi.org/10.1130/g31072.1

Hough, M. L., Shields, G. A., Evins, L. Z., Strauss, H., Henderson, R. A., & Mackenzie, S. (2006). A major sulphur isotope event at c. 510 Ma: A possible anoxia-extinction-volcanism connection during the Early-Middle Cambrian transition? *Terra Nova*. https://doi.org/10.1111/j.1365-3121.2006.00687.x

Huang, C., & Hesselbo, S. P. (2014). Pacing of the Toarcian Oceanic Anoxic Event (Early Jurassic) from astronomical correlation of marine sections. *Gondwana Research*, *25*(4), 1348–1356. https://doi.org/10.1016/j.gr.2013.06.023

Ivanov, A. V, He, H., Yan, L., Ryabov, V. V, Shevko, A. Y., Palesskii, S. V, & Nikolaeva, I. V. (2013). Siberian Traps large igneous province: Evidence for two flood basalt pulses around the Permo-Triassic boundary and in the Middle Triassic, and contemporaneous granitic magmatism. *Earth-Science Reviews*. https://doi.org/10.1016/j.earscirev.2013.04.001

Ivanov, A. V, He, H., Yang, L., Nikolaeva, I. V, & Palesskii, S. V. (2009). $^{40}Ar/^{39}Ar$ dating of intrusive magmatism in the Angara-Taseevskaya syncline and its implication for duration of magmatism of the Siberian traps. *Journal of Asian Earth Sciences*. https://doi.org/10.1016/j.jseaes.2008.11.006

Ivanov, A. V, Meffre, S., Thompson, J., Corfu, F., Kamenetsky, V. S., Kamenetsky, M. B., & Demonterova, E. I. (2017). Timing and genesis of the Karoo-Ferrar large igneous province: New high precision U-Pb data for Tasmania confirm short duration of the major magmatic pulse. *Chemical Geology*, *455*, 32–43. https://doi.org/10.1016/j.chemgeo.2016.10.008

Ivanov, A. V., Rasskazov, S. V., Feoktistov, G. D., He, H., & Boven, A. (2005). $^{40}Ar/^{39}Ar$ dating of Usol'skii sill in the south-eastern Siberian Traps Large Igneous Province: Evidence for long-lived magmatism. *Terra Nova*, *17*(3), 203–208. https://doi.org/10.1111/j.1365-3121.2004.00588.x

Jaffey, A. H., Flynn, K. F., Glendenin, L. E., Bentley, W. C., & Essling, A. M. (1971). Precision measurement of half-lives and specific activities of ^{235}U and ^{238}U. *Physical Review C*, *4*(5), 1889–1906. https://doi.org/10.1103/PhysRevC.4.1889

Jahren, A. H. (2002). The biogeochemical consequences of the mid-Cretaceous superplume. *Journal of Geodynamics*. https://doi.org/10.1016/S0264-3707(02)00020-0

Jaramillo, C., Ochoa, D., Contreras, L., Pagani, M., Carvajal-Ortiz, H., Pratt, L. M., et al. (2010). Effects of rapid global warming at the Paleocene-Eocene boundary on neotropical vegetation. *Science*, *330*(6006), 957. https://doi.org/10.1126/science.1193833

Jay, A. E., & Widdowson, M. (2008). Stratigraphy, structure and volcanology of the SE Deccan continental flood basalt province: implications for eruptive extent and volumes. *Journal of the Geological Society*, *165*(1), 177–188. https://doi.org/10.1144/0016-76492006-062

Jenkyns, H. C. (2010). Geochemistry of oceanic anoxic events. *Geochemistry, Geophysics, Geosystems*, 11(3). https://doi.org/10.1029/2009GC002788

Jicha, B. R., Singer, B. S., & Sobol, P. (2016). Re-evaluation of the ages of ^{40}Ar/^{39}Ar sanidine standards and supereruptions in the western U.S. using a Noblesse multi-collector mass spectrometer. *Chemical Geology*, *431*, 54–66. https://doi.org/10.1016/J.CHEMGEO.2016.03.024

Joachimski, M. M., & Buggisch, W. (1993). Anoxic events in the late Frasnian: Causes of the Frasnian-Famennian faunal crisis? *Geology*, *21*(8), 675–678. https://doi.org/10.1130/0091-7613(1993)021<0675:AEITLF>2.3.CO;2

Joachimski, M. M., Pancost, R. D., Freeman, K. H., Ostertag-Henning, C., & Buggisch, W. (2002). Carbon isotope geochemistry of the Frasnian-Famennian transition. *Palaeogeography, Palaeoclimatology, Palaeoecology*, *181*(1–3), 91–109. https://doi.org/10.1016/S0031-0182(01)00474-6

Jones, D. L., Duncan, R. A., Briden, J. C., Randall, D. E., & Macniocaill, C. (2001). Age of the Batoka basalts, northern ZImbabwe, and the duration of Karoo Large Igneous Province magmatism. *Geochemistry, Geophysics, Geosystems*, *2*(2). https://doi.org/10.1029/2000GC000110

Jost, A. B., Mundil, R., He, B., Brown, S. T., Altiner, D., Sun, Y., et al. (2014). Constraining the cause of the end-Guadalupian extinction with coupled records of carbon and calcium isotopes. *Earth and Planetary Science Letters*. https://doi.org/10.1016/j.epsl.2014.04.014

Jourdan, F., Féraud, G., Bertrand, H., Kampunzu, A. B., Tshoso, G., Watkeys, M. K., & Le Gall, B. (2005). Karoo large igneous province: Brevity, origin, and relation to mass extinction questioned by new ^{40}Ar/^{39}Ar age data. *Geology*, *33*(9), 745. https://doi.org/10.1130/G21632.1

Jourdan, F., Féraud, G., Bertrand, H., Watkeys, M. K., & Renne, P. R. (2007). Distinct brief major events in the Karoo large igneous province clarified by new ^{40}Ar/^{39}Ar ages on the Lesotho basalts. *Lithos*, *98*(1–4), 195–209. https://doi.org/10.1016/j.lithos.2007.03.002

Jourdan, F., Féraud, G., Bertrand, H., Watkeys, M. K., & Renne, P. R. (2008). The ^{40}Ar/^{39}Ar ages of the sill complex of the Karoo large igneous province: Implications for the Pliensbachian-Toarcian climate change. *Geochemistry, Geophysics, Geosystems*, 9(6). https://doi.org/10.1029/2008GC001994

Jourdan, F., Hodges, K., Sell, B., Schaltegger, U., Wingate, M. T. D., Evins, L. Z., et al. (2014). High-precision dating of the Kalkarindji large igneous province, Australia, and synchrony with the Early-Middle Cambrian (Stage 4-5) extinction. *Geology*. https://doi.org/10.1130/G35434.1

Jourdan, F., Marzoli, A., Bertrand, H., Cirilli, S., Tanner, L. H., Kontak, D. J., et al. (2009). ^{40}Ar/^{39}Ar ages of CAMP in North America: Implications for the Triassic-Jurassic boundary and the ^{40}K decay constant bias. *Lithos*, *110*(1–4), 167–180. https://doi.org/10.1016/j.lithos.2008.12.011

Kamo, S. L., Czamanske, G. K., & Krogh, T. E. (1996). A minimum U-Pb age for Siberian flood-basalt volcanism. *Geochimica et Cosmochimica Acta*. https://doi.org/10.1016/0016-7037(96)00173-1

Kamo, S. L., Czamanske, G. K., Amelin, Y., Fedorenko, V. A., Davis, D. W., & Trofimov, V. R. (2003). Rapid eruption of Siberian flood-volcanic rocks and evidence for coincidence with the Permian-Triassic boundary and mass extinction at 251 Ma. *Earth and Planetary Science Letters*, *214*(1–2), 75–91. https://doi.org/10.1016/S0012-821X(03)00347-9

Kamo, S. L., Gower, C. F., & Krogh, T. E. (1989). Birthdate for the lapetus Ocean? A precise U-Pb zircon and baddeleyite age for the Long Range dikes, southeast Labrador. *Geology*, *17*(7), 602. https://doi.org/10.1130/0091-7613(1989)017<0602:BFTLOA>2.3.CO;2

Kasbohm, J. J., & Schoene, B. (2018). Rapid eruption of the Columbia River flood basalt and correlation with the mid-Miocene climate optimum. *Science Advances*, *4*(9), 1–8. https://doi.org/10.1126/sciadv.aat8223

Kaufmann, B., Trapp, E., & Mezger, K. (2004). The numerical age of the Upper Frasnian (Upper Devonian) Kellwasser horizons: A new U-Pb zircon date from Steinbruch Schmidt (Kellerwald, Germany). *The Journal of Geology*. https://doi.org/10.1086/421077

Keller, C. B., Schoene, B., & Samperton, K. M. (2018). A stochastic sampling approach to zircon eruption age interpretation. *Geochemical Perspectives Letters*, 31–35. https://doi.org/10.7185/geochemlet.1826

Keller, G., Adatte, T., Bhowmick, P. K., Upadhyay, H., Dave, A., Reddy, A. N., & Jaiprakash, B. C. (2012). Nature and timing of extinctions in Cretaceous-Tertiary planktic foraminifera preserved in Deccan intertrappean sediments of the Krishna–Godavari Basin, India. *Earth and Planetary Science Letters*, *341–344*, 211–221. https://doi.org/10.1016/j.epsl.2012.06.021

Keller, G., Adatte, T., Gardin, S., Bartolini, A., & Bajpai, S. (2008). Main Deccan volcanism phase ends near the K-T boundary: Evidence from the Krishna-Godavari basin, SE India. *Earth and Planetary Science Letters*, *268*(3–4), 293–311. https://doi.org/10.1016/j.epsl.2008.01.015

Kerr, A. C. (2014). *Oceanic plateaus*. *Treatise on geochemistry* (2nd ed.). Elsevier Ltd. https://doi.org/10.1016/B978-0-08-095975-7.00320-X

Kerr, A. C., White, R. V., Thompson, P. M. E., Tarney, J., & Saunders, A. D. (2003). No Oceanic plateau, no Caribbean plate? The seminal role of an oceanic plateau in Caribbean plate evolution. *AAPG Memoir*, *79*, 23–26.

Khadri, S. F. R., Subbarao, K. V., Hooper, P. R., & Walsh, J. N. (1988). Stratigraphy of Thakurvadi formation, western

Deccan basalt province, India. In *M-10 Deccan flood basalts* (pp. 281–304). Geological Society of India.

Kiehl, J. T., & Shields, C. A. (2005). Climate simulation of the latest Permian: Implications for mass extinction. *Geology*. https://doi.org/10.1130/G21654.1

Knight, K. B., Nomade, S., Renne, P. R., Marzoli, A., Bertrand, H., & Youbi, N. (2004). The Central Atlantic Magmatic Province at the Triassic-Jurassic boundary: paleomagnetic and $^{40}Ar/^{39}Ar$ evidence from Morocco for brief, episodic volcanism. *Earthand Planetary Science Leters*, *228*(1–2), 143–160. https://doi.org/10.1016/j.epsl.2004.09.022

Knight, K. B., Renne, P. R., Halkett, A., & White, N. (2003). $^{40}Ar/^{39}Ar$ dating of the Rajahmundry Traps, Eastern India and their relationship to the Deccan Traps. *Earth and Planetary Science Letters*, *208*(1–2), 85–99. https://doi.org/10.1016/s0012-821x(02)01154-8

Knoll, A. H., Bambach, R. K., Payne, J. L., Pruss, S., & Fischer, W. W. (2007). Paleophysiology and end-Permian mass extinction. *Earth and Planetary Science Letters*. https://doi.org/10.1016/j.epsl.2007.02.018

Kochhann, K. G. D., Holbourn, A., Kuhnt, W., Channell, J. E. T., Lyle, M., Shackford, J. K., et al. (2016). Eccentricity pacing of eastern equatorial Pacific carbonate dissolution cycles during the Miocene Climatic Optimum. *Paleoceanography*, *31*(9), 1176–1192. https://doi.org/10.1002/2016PA002988

Krogh, T. E. (1973). A low-contamination method for hydrothermal decomposition of zircon and extraction of U and Pb for isotopic age determinations. *Geochimica et Cosmochimica Acta*, *37*(3), 485–494. https://doi.org/10.1016/0016-7037(73)90213-5

Krogh, T. E., Corfu, F., Davis, D. W., Dunning, G. R., Heaman, L. M., Kamo, S. L., et al. (1987). Precise U-Pb isotopic ages of diabase dykes and mafic to ultramafic rocks using trace amounts of baddeleyite and zircon. In H. C. Halls & W. F. Fahrig (Eds.), *Mafic dike swarms*, *34,* 147–152. Geological Association of Canada, Special Paper.

Kuiper, K. F., Deino, A. L., Hilgen, F. J., Krijgsman, W., Renne, P. R., & Wijbrans, J. R. (2008). Synchronizing rock clocks of earth history. *Science*, *320*(5875), 500–504. https://doi.org/10.1126/science.1154339

Kuroda, J., Ogawa, N. O., Tanimizu, M., Coffin, M. F., Tokuyama, H., Kitazato, H., & Ohkouchi, N. (2007). Contemporaneous massive subaerial volcanism and late Cretaceous Oceanic Anoxic Event 2. *Earth and Planetary Science Letters*, *256*(1–2), 211–223. https://doi.org/10.1016/J.EPSL.2007.01.027

Kürschner, W. M., Kvacek, Z., & Dilcher, D. L. (2008). The impact of Miocene atmospheric carbon dioxide fluctuations on climate and the evolution of terrestrial ecosystems. *Proceedings of the National Academy of Sciences*, *105*(2), 449–453. https://doi.org/10.1073/pnas.0708588105

Landing, E., Bowring, S. A., Davidek, K. L., Westrop, S. R., Geyer, G., & Heldmaier, W. (1998). Duration of the Early Cambrian: U-Pb ages of volcanic ashes from Avalon and Gondwana. *Canadian Journal of Earth Sciences*. https://doi.org/10.1139/e97-107

Larsen, L. M., Pedersen, A. K., Tegner, C., & Duncan, R. A. (2014). Eocene to Miocene igneous activity in NE Greenland: Northward younging of magmatism along the East Greenland margin. *Journal of the Geological Society*, *171*(4), 539–553. https://doi.org/10.1144/jgs2013-118

Larsen, L. M., Pedersen, A. K., Tegner, C., Duncan, R. A., Hald, N., & Larsen, J. G. (2016). Age of Tertiary volcanic rocks on the West Greenland continental margin: Volcanic evolution and event correlation to other parts of the North Atlantic Igneous Province. *Geological Magazine*, *153*(3), 487–511. https://doi.org/10.1017/S0016756815000515

Larsen, T. B., Yuen, D. A., & Storey, M. (1999). Ultrafast mantle plumes and implications for flood basalt volcanism in the northern Atlantic region. *Tectonophysics*, *311*(1–4), 31–43. https://doi.org/10.1016/S0040-1951(99)00163-8

Larson, R. L., & Erba, E. (1999). Onset of the mid-Cretaceous greenhouse in the Barremian-Aptian: Igneous events and the biological, sedimentary, and geochemical responses. *Paleoceanography*, *14*(6), 663–678. https://doi.org/10.1029/1999PA900040

Laskar, J., Robutel, P., Joutel, F., Gastineau, M., Correia, A. C. M., & Levrard, B. (2004). A long-term numerical solution for the insolation quantities of the Earth. *Astronomy and Astrophysics*, *428*(1), 261–285. https://doi.org/10.1051/0004-6361:20041335

Le Gall, B., Tshoso, G., Jourdan, F., Féraud, G., Bertrand, H., Tiercelen, J. J., et al. (2002). $^{40}Ar/^{39}Ar$ geochronology and structural data from the giant Okavango and related mafic dyke swarms, Karoo Igneous province, northern Botswana. *Earth and Planetary Science Letters*, *202*(3–4), 595–606. https://doi.org/10.1016/S0012-821X(02)00763-X

Li, L., & Keller, G. (1998). Abrupt deep-sea warming at the end of the Cretaceous. *Geology*, *26*(11), 995–998. https://doi.org/10.1130/0091-7613(1998)026<0995:ADSWAT>2.3.CO;2

Li, M., Ogg, J. G., Zhang, Y., Huang, C., Hinnov, L. A., Chen, Z. Q., & Zou, Z. (2016). Astronomical tuning of the end-Permian extinction and the Early Triassic Epoch of south China and Germany. *Earth and Planetary Science Letters*, *441*, 10–25. https://doi.org/10.1016/j.epsl.2016.02.017

Li, Y. X., Bralower, T. J., Montañez, I. P., Osleger, D. A., Arthur, M. A., Bice, D. M., et al. (2008). Toward an orbital chronology for the early Aptian Oceanic Anoxic Event (OAE1a, ~120 Ma). *Earth and Planetary Science Letters*. https://doi.org/10.1016/j.epsl.2008.03.055

Lindström, S., van de Schootbrugge, B., Hansen, K. H., Pedersen, G. K., Alsen, P., Thibault, N., et al. (2017). A new correlation of Triassic-Jurassic boundary successions in NW Europe, Nevada and Peru, and the Central Atlantic Magmatic Province: A time-line for the end-Triassic mass extinction. *Palaeogeography, Palaeoclimatology, Palaeoecology*, *478*, 80–102. https://doi.org/10.1016/j.palaeo.2016.12.025

Macdonald, F. A., & Wordsworth, R. (2017). Initiation of Snowball Earth with volcanic sulfur aerosol emissions. *Geophysical Research Letters*. https://doi.org/10.1002/2016GL072335

Macdonald, F. A., Schmitz, M. D., Crowley, J. L., Roots, C. F., Jones, D. S., Maloof, A. C., et al. (2010). Calibrating the Cryogenian. *Science*. https://doi.org/10.1126/science.1183325

Macdonald, F. A., Schmitz, M. D., Strauss, J. V., Halverson, G. P., Gibson, T. M., Eyster, A., et al. (2017). Cryogenian of Yukon. *Precambrian Research*. https://doi.org/10.1016/j.precamres.2017.08.015

Maclennan, S., Park, Y., Swanson-Hysell, N., Maloof, A. C., Schoene, B., Gebreslassie, M., et al. (2018). The arc of the Snowball: U-Pb dates constrain the Islay anomaly and the initiation of the Sturtian glaciation. *Geology.* https://doi.org/10.1130/G40171.1

Mahoney, J. J., Storey, M., Duncan, R. A., Spencer, K. J., & Pringle, M. S. (1993). Geochemistry and geochronology of Leg 130 basement lavas: Nature and origin of the Ontong Java plateau. *Proceedings of the Ocean Drilling Program, Scientific Results, 130,* 3–22.

Mahood, G. A., & Benson, T. R. (2017). Using $^{40}Ar/^{39}Ar$ ages of intercalated silicic tuffs to date flood basalts: Precise ages for Steens Basalt Member of the Columbia River Basalt Group. *Earth and Planetary Science Letters*, *459*, 340–351. https://doi.org/10.1016/j.epsl.2016.11.038

Malinverno, A., Erba, E., & Herbert, T. (2010). Orbital tuning as an inverse problem: Chronology of the early Aptian oceanic anoxic event 1a (Selli Level) in the Cismon APTICORE. *Paleoceanography* (25:PA2203), 1–16. doi: 10.1029/2009PA001769

Malitch, K. N., Badanina, I. Y., Belousova, E. A., & Tuganova, E. V. (2012). Results of U-Pb dating of zircon and baddeleyite from the Noril'sk-1 ultramafic-mafic intrusion (Russia). *Russian Geology and Geophysics.* https://doi.org/10.1016/j.rgg.2011.12.010

Malitch, K. N., Belousova, E. A., Griffin, W., Badanina, I. Y., Pearson, N. J., Presnyakov, S. L., et al. (2010). Magmatic evolution of the ultramafic-mafic Kharaelakh intrusion (Siberian Craton, Russia): Insights from trace-element, U-Pb and Hf-isotope data on zircon. *Contributions to Mineralogy and Petrology*, *159*(6), 753–768. https://doi.org/10.1007/s00410-009-0452-z

Marzoli, A., Bertrand, H., Knight, K. B., Cirilli, S., Buratti, N., Vérati, C., et al. (2004). Synchrony of the Central Atlantic magmatic province and the Triassic-Jurassic boundary climatic and biotic crisis. *Geology.* https://doi.org/10.1130/G20652.1

Marzoli, A., Bertrand, H., Youbi, N., Callegaro, S., Merle, R. E., Reisberg, L., et al. (2019). The Central Atlantic Magmatic Province (CAMP) in Morocco. *Journal of Petrology*, *60*(5), 945–996. https://doi.org/10.1093/petrology/egz021

Marzoli, A., Callegaro, S., Dal Corso, J., Davies, J. H. F. L., Chiaradia, M., Youbi, N., et al. (2018). The Central Atlantic Magmatic Province (CAMP): A review. In *The Late Triassic world* (pp. 91–125). Springer.

Marzoli, A., Jourdan, F., Puffer, J. H., Cuppone, T., Tanner, L. H., Weems, R. E., et al. (2011). Timing and duration of the Central Atlantic magmatic province in the Newark and Culpeper basins, eastern USA. *Lithos*, *122*(3–4), 175–188. https://doi.org/10.1016/j.lithos.2010.12.013

Marzoli, A., Renne, P. R., Piccirillo, E. M., Ernesto, M., Bellieni, G., & De Min, A. (1999). Extensive 200-million-year-old continental flood basalts of the Central Atlantic Magmatic Province. *Science*, *284*, 616–618. https://doi.org/10.1126/science.284.5414.616

Mattinson, J. M. (2005). Zircon U-Pb chemical abrasion ("CA-TIMS") method: Combined annealing and multi-step partial dissolution analysis for improved precision and accuracy of zircon ages. *Chemical Geology*, *220*(1–2), 47–66. https://doi.org/10.1016/j.chemgeo.2005.03.011

McGhee, G. R. (2013). The first catastrophe and retreat. In *When the invasion of land failed: The legacy of the Devonian extinctions* (pp. 99–158). Columbia University Press. https://doi.org/10.7312/mcgh16056

McHone, J. G. (2003). Volatile emissions from Central Atlantic Magmatic Province basalts: Mass assumptions and environmental consequences. In W. E. Hames, J. G. McHone, P. R. Renne, & C. R. Ruppel (Eds.), *The Central Atlantic Magmatic Province: Insights from fragments of Pangea* (pp. 241–254), Geophysical Monograph *136*. Washington: American Geophyiscal Union.

McLean, D. M. (1985). Deccan Traps mantle degassing in the terminal Cretaceous marine extinctions. *Cretaceous Research*, *6*(3), 235–259.

McLean, N. M., Bowring, J. F., & Bowring, S. A. (2011). An algorithm for U-Pb isotope dilution data reduction and uncertainty propagation. *Geochemistry, Geophysics, Geosystems*, 12(6). https://doi.org/10.1029/2010GC003478

McLean, N. M., Condon, D. J., Schoene, B., & Bowring, S. A. (2015). Evaluating uncertainties in the calibration of isotopic reference materials and multi-element isotopic tracers (EARTHTIME Tracer Calibration Part II). *Geochimica et Cosmochimica Acta*, *164*, 481–501. https://doi.org/10.1016/j.gca.2015.02.040

Menegatti, A. P., Weissert, H., Brown, R. S., Tyson, R. V., Farrimond, P., Strasser, A., & Caron, M. (1998). High-resolution $\delta^{13}C$ stratigraphy through the Early Aptian "Livello selli" of the Alpine tethys. *Paleoceanography*, *13*(5), 530–545. https://doi.org/10.1029/98PA01793

Meyers, S. R., Sageman, B. B., & Hinnov, L. A. (2001). Integrated quantitative stratigraphy of the Cenomanian-Turonian Bridge Creek Limestone Member using evolutive harmonic analysis and stratigraphic modeling. *Journal of Sedimentary Research.* https://doi.org/10.1306/012401710628

Meyers, S. R., Siewert, S. E., Singer, B. S., Sageman, B. B., Condon, D. J., Obradovich, J. D., et al. (2012). Intercalibration of radioisotopic and astrochronologic time scales for the Cenomanian-Turonian boundary interval, Western Interior Basin, USA. *Geology*, *40*(1), 7–10. https://doi.org/10.1130/G32261.1

Michard-Vitrac, A., Lancelot, J., Allègre, C. J., & Moorbath, S. (1977). U-Pb ages on single zircons from the Early Precambrian rocks of West Greenland and the Minnesota River valley. *Earth and Planetary Science Letters*, *35*(3), 449–453. https://doi.org/10.1016/0012-821X(77)90077-2

Midtkandal, I., Svensen, H. H., Planke, S., Corfu, F., Polteau, S., Torsvik, T. H., et al. (2016). The Aptian (Early Cretaceous) oceanic anoxic event (OAE1a) in Svalbard, Barents Sea, and the absolute age of the Barremian-Aptian boundary. *Palaeogeography, Palaeoclimatology, Palaeoecology*, *463*, 126–135. https://doi.org/10.1016/J.PALAEO.2016.09.023

Min, K., Mundil, R., Renne, P. R., & Ludwig, K. R. (2000). A test for systematic errors in $^{40}Ar/^{39}Ar$ geochronology through comparison with U-Pb analysis of a 1.1 Ga rhyolite. *Geochimica et Cosmochimica Acta*, *64*, 73–98. https://doi.org/10.1016/S0016-7037(99)00204-5

Minor, D. R., & Mukasa, S. B. (1997). Zircon U-Pb and hornblende ^{40}Ar-^{39}Ar ages for the Dufek layered mafic intrusion, Antarctica: Implications for the age of the Ferrar large igneous province. *Geochimica et Cosmochimica Acta*, *61*(12), 2497–2504. https://doi.org/10.1016/S0016-7037(97)00098-7

Mitchell, R. N., Bice, D. M., Montanari, A., Cleaveland, L. C., Christianson, K. T., Coccioni, R., & Hinnov, L. A. (2008). Oceanic anoxic cycles? Orbital prelude to the Bonarelli Level (OAE 2). *Earth and Planetary Science Letters*. https://doi.org/10.1016/j.epsl.2007.11.026

Moulin, M., Fluteau, F. F., Courtillot, V. E., Marsh, J. S., Delpech, G., Quidelleur, X., & Gérard, M. (2017). Eruptive history of the Karoo lava flows and their impact on early Jurassic environmental change. *Journal of Geophysical Research: Solid Earth*, *122*(2), 738–772. https://doi.org/10.1002/2016JB013354

Moulin, M., Fluteau, F. F., Courtillot, V. E., Marsh, J. S., Delpech, G., Quidelleur, X., et al. (2011). An attempt to constrain the age, duration, and eruptive history of the Karoo flood basalt: Naude's Nek section (South Africa). *Journal of Geophysical Research: Solid Earth*, *116*(B7), 2300–2327. https://doi.org/10.1029/2011JB008210

Mundil, R., Ludwig, K. R., Metcalfe, I., & Renne, P. R. (2004). Age and timing of the Permian mass extinctions: U/Pb dating of closed-system zircons. *Science*. https://doi.org/10.1126/science.1101012

Mundil, R., Metcalfe, I., Ludwig, K. R., Renne, P. R., Oberli, F., & Nicoll, R. S. (2001). Timing of the Permian-Triassic biotic crisis: Implications from new zircon U/Pb age data (and their limitations). *Earth and Planetary Science Letters*. https://doi.org/10.1016/S0012-821X(01)00274-6

Murphy, B. H., Farley, K. A., & Zachos, J. C. (2010). An extraterrestrial ^{3}He-based timescale for the Paleocene-Eocene thermal maximum (PETM) from Walvis Ridge, IODP Site 1266. *Geochimica et Cosmochimica Acta*, *74*(17), 5098–5108. https://doi.org/10.1016/j.gca.2010.03.039

Naafs, B. D. A., Castro, J. M., De Gea, G. A., Quijano, M. L., Schmidt, D. N., & Pancost, R. D. (2016). Gradual and sustained carbon dioxide release during Aptian Oceanic Anoxic Event 1a. *Nature Geoscience*, *9*(2), 135–139. https://doi.org/10.1038/ngeo2627

Nomade, S., Knight, K. B., Beutel, E., Renne, P. R., Verati, C., Féraud, G., et al. (2007). Chronology of the Central Atlantic Magmatic Province: Implications for the central Atlantic rifting processes and the Triassic-Jurassic biotic crisis. *Palaeogeography, Palaeoclimatology, Palaeoecology*, *244*(1–4), 326–344. https://doi.org/10.1016/j.palaeo.2006.06.034

Ogg, J. G., Hinnov, L. A., & Huang, C. (2012). *Chapter 27: Cretaceous*. *The geologic time scale*. https://doi.org/10.1016/B978-0-444-59425-9.00027-5

Olierook, H. K. H., Jourdan, F., & Merle, R. E. (2019). Age of the Barremian–Aptian boundary and onset of the Cretaceous Normal Superchron. *Earth-Science Reviews*, *197*(102906), 1–22. https://doi.org/10.1016/j.earscirev.2019.102906

Olsen, P. E., Kent, D. V., Et-Touhami, M., & Puffer, J. H. (2003). Cyclo-, magneto-, and bio-stratigraphic constraints on the duration of the CAMP event and its relationship to the Triassic-Jurassic boundary. In W. E. Hames, J. G. McHone, P. R. Renne, & C. R. Ruppel (Eds.), *The Central Atlantic Magmatic Province: Insights from fragments of Pangea*. American Geophysical Union, Geophysical Monograph. https://doi.org/10.1029/136GM02

Pálfy, J., & Smith, P. L. (2000). Synchrony between Early Jurassic extinction, oceanic anoxic event, and the Karoo-Ferrar flood basalt volcanism. *Geology*, *28*(8), 745–747. https://doi.org/10.1130/0091-7613(2000)28%3C747:SBEJEO%3E2.0.CO

Pálfy, J., Mortensen, J. K., Carter, E. S., Smith, P. L., Friedman, R. M., & Tipper, H. W. (2000a). Timing the end-Triassic mass extinction: First on land, then in the sea? *Geology*, *28*(1), 39–42. https://doi.org/10.1130/0091-7613(2000)28<39:TTEMEF>2.0.CO;2

Pálfy, J., Smith, P. L., & Mortensen, J. K. (2000b). A U-Pb and ^{40}Ar/^{39}Ar time scale for the Jurassic. *Canadian Journal of Earth Sciences*, *37*, 923–944. https://doi.org/10.1139/e00-002

Pálfy, J., Smith, P. L., & Mortensen, J. K. (2002). Dating the end-Triassic and Early Jurassic mass extinctions, correlative large igneous provinces, and isotopic events. In *Special Paper 356: Catastrophic events and mass extinctions: Impacts and beyond* (pp. 523–532). Geological Society of America. https://doi.org/10.1130/0-8137-2356-6.523

Pande, K. (2002). Age and duration of the Deccan Traps, India: A review of radiometric and paleomagnetic constraints. *Proceedings-Indian Academy of Sciences Earth and Planetary Sciences*, *111*(2), 115–124.

Parrish, R. R. (1987). An improved micro-capsule for zircon dissolution in U-Pb geochronology. *Chemical Geology: Isotope Geoscience Section*, *66*(1–2), 99–102. https://doi.org/10.1016/0168-9622(87)90032-7

Parsons-Davis, T., Wimpenny, J., Keller, C. B., Thomas, K., Samperton, K. M., Renne, P. R., et al. (2018). New measurement of the ^{238}U decay constant with inductively coupled plasma mass spectrometry. *Journal of Radioanalytical and Nuclear Chemistry*, *318*(1), 711–721. https://doi.org/10.1007/s10967-018-6148-y

Paton, M. T., Ivanov, A. V., Fiorentini, M. L., McNaughton, N. J., Mudrovska, I., Reznitskii, L. Z., & Demonterova, E. I. (2010). Late Permian and Early Triassic magmatic pulses in the Angara-Taseeva syncline, Southern Siberian Traps and their possible influence on the environment. *Russian Geology and Geophysics*. https://doi.org/10.1016/j.rgg.2010.08.009

Pavlov, V. E., Fluteau, F. F., Latyshev, A. V, Fetisova, A. M., Elkins-Tanton, L. T., Black, B. A., et al. (2019). Geomagnetic secular variations at the Permian-Triassic Boundary and pulsed magmatism during eruption of the Siberian Traps. *Geochemistry, Geophysics, Geosystems*, *20*(2). https://doi.org/10.1029/2018GC007950

Penn, J. L., Deutsch, C., Payne, J. L., & Sperling, E. A. (2018). Temperature-dependent hypoxia explains biogeography and severity of end-Permian marine mass extinction. *Science*. https://doi.org/10.1126/science.aat1327

Percival, L. M. E., Davies, J. H. F. L., Schaltegger, U., De Vleeschouwer, D., Da Silva, A. C., & Föllmi, K. B. (2018). Precisely dating the Frasnian-Famennian boundary: Implications for the cause of the Late Devonian mass extinction. *Scientific Reports*. https://doi.org/10.1038/s41598-018-27847-7

Petersen, S. V, Dutton, A., & Lohmann, K. C. (2016). End-Cretaceous extinction in Antarctica linked to both Deccan volcanism and meteorite impact via climate change. *Nature Communications*, *7:12079*. https://doi.org/10.1038/ncomms12079

Polteau, S., Hendriks, B. W. H., Planke, S., Ganerød, M., Corfu, F., Faleide, J. I., et al. (2016). The Early Cretaceous Barents Sea Sill Complex: Distribution, ^{40}Ar/^{39}Ar geochronology, and implications for carbon gas formation. *Palaeogeography,*

Palaeoclimatology, Palaeoecology, *441*, 83–95. https://doi.org/10.1016/j.palaeo.2015.07.007

Polyansky, O. P., Prokopiev, A. V., Koroleva, O. V., Tomshin, M. D., Reverdatto, V. V., Selyatitsky, A. Y., et al. (2017). Temporal correlation between dyke swarms and crustal extension in the middle Palaeozoic Vilyui rift basin, Siberian platform. *Lithos*, *282–283*, 45–64. https://doi.org/10.1016/j.lithos.2017.02.020

Punekar, J., Mateo, P., & Keller, G. (2014). Effects of Deccan volcanism on paleoenvironment and planktic foraminifera: A global survey. *Geological Society of America Special Paper*, *505*, 91. https://doi.org/10.1130/2014.2505(04)

Racki, G. (1998). Frasnian-Famennian biotic crisis: Undervalued tectonic control? *Palaeogeography, Palaeoclimatology, Palaeoecology*. https://doi.org/10.1016/S0031-0182(98)00059-5

Racki, G., Rakociński, M., Marynowski, L., & Wignall, P. B. (2018). Mercury enrichments and the Frasnian-Famennian biotic crisis: A volcanic trigger proved? *Geology*, *46*(6), 543–546. https://doi.org/10.1130/G40233.1

Ramezani, J., & Bowring, S. A. (2017). Advances in numerical calibration of the Permian timescale based on radioisotopic geochronology. *Geological Society, London, Special Publications*. https://doi.org/10.1144/sp450.17

Ramezani, J., Schmitz, M. D., Davydov, V. I., Bowring, S. A., Snyder, W. S., & Northrup, C. J. (2007). High-precision U-Pb zircon age constraints on the Carboniferous-Permian boundary in the southern Urals stratotype. *Earth and Planetary Science Letters*, *256*(1–2), 244–257. https://doi.org/10.1016/j.epsl.2007.01.032

Rampino, M. R., & Stothers, R. B. (1988). Flood basalt volcanism during the past 250 million years. *Science*. https://doi.org/10.1126/science.241.4866.663

Raval, U., & Veeraswamy, K. (2003). India-Madagascar separation: Breakup along a pre-existing mobile belt and chipping of the craton. *Gondwana Research*, *6*(3), 467–485. https://doi.org/10.1016/S1342-937X(05)70999-0

Ravizza, G., & VonderHaar, D. (2012). A geochemical clock in earliest Paleogene pelagic carbonates based on the impact-induced Os isotope excursion at the Cretaceous-Paleogene boundary. *Paleoceanography and Paleoclimatology, 27*(3). https://doi.org/10.1029/2012PA002301

Reichow, M. K., Pringle, M. S., Al'Mukhamedov, A. I., Allen, M. B., Andreichev, V. L., Buslov, M. M., et al. (2009). The timing and extent of the eruption of the Siberian Traps large igneous province: Implications for the end-Permian environmental crisis. *Earth and Planetary Science Letters*. https://doi.org/10.1016/j.epsl.2008.09.030

Reichow, M. K., Saunders, A. D., Scott, R. A., Millar, I. L., Barfod, D., Pringle, M. S., et al. (2016). Petrogenesis and timing of mafic magmatism, South Taimyr, Arctic Siberia: A northerly continuation of the Siberian Traps? *Lithos*. https://doi.org/10.1016/j.lithos.2016.01.018

Reichow, M. K., Saunders, A. D., White, R. V., Pringle, M. S., Al'Mukhamedov, A. I., Medvedev, A. I., & Kirda, N. P. (2002). $^{40}Ar/^{39}Ar$ dates from the West Siberian basin: Siberian flood basalt province doubled. *Science*. https://doi.org/10.1126/science.1071671

Reidel, S. P. (2015). The Columbia River Basalt Group: a flood basalt province in the Pacific Northwest, USA. *Geoscience Canada*, *42*, 151–168. https://doi.org/10.1007/s13398-014-0173-7.2

Reimold, W. U., Kelley, S. P., Sherlock, S. C., Henkel, H., & Koeberl, C. (2005). Laser argon dating of melt breccias from the Siljan impact structure, Sweden: Implications for a possible relationship to Late Devonian extinction events. *Meteoritics and Planetary Science*. https://doi.org/10.1111/j.1945-5100.2005.tb00965.x

Reiners, P. W., Carlson, R. W., Renne, P. R., Cooper, K. M., Granger, D. E., McLean, N. M., & Schoene, B. (2017). *Geochronology and thermochronology*. *Geochronology and Thermochronology*. https://doi.org/10.1002/9781118455876

Renne, P. R. (1995). Excess ^{40}Ar in biotite and hornblende from the Noril'sk 1 intrusion, Siberia: Implications for the age of the Siberian Traps. *Earth and Planetary Science Letters*. https://doi.org/10.1016/0012-821X(95)00015-5

Renne, P. R., & Basu, A. R. (1991). Rapid eruption of the Siberian Traps flood basalts at the Permo-Triassic Boundary. *Science*, *253*(5016), 176–179. https://doi.org/10.1126/science.253.5016.176

Renne, P. R., Arenillas, I., Arz, J. A., Vajda, V., Gilabert, V., & Bermúdez, H. D. (2018). Multi-proxy record of the Chicxulub impact at the Cretaceous-Paleogene boundary from Gorgonilla Island, Colombia. *Geology*, *46*(6), 547–550. https://doi.org/10.1130/G40224.1

Renne, P. R., Balco, G., Ludwig, K. R., Mundil, R., & Min, K. (2011). Response to the comment by W. H. Schwarz et al. on "Joint determination of ^{40}K decay constants and $^{40}Ar^*/^{40}K$ for the Fish Canyon sanidine standard, and improved accuracy for $^{40}Ar/^{39}Ar$ geochronology" by P. R. Renne et al. (2010), *Geochimica et Cosmochimica Acta*, *75*(17), 5097–5100. https://doi.org/10.1016/j.gca.2011.06.021

Renne, P. R., Deino, A. L., Hilgen, F. J., Kuiper, K. F., Mark, D. F., Mitchell, W. S. III, et al. (2013). Time scales of critical events around the Cretaceous-Paleogene boundary. *Science*, *339*(6120), 684–687. https://doi.org/10.1126/science.1230492

Renne, P. R., Karner, D. B., & Ludwig, K. R. (1998a). Absolute ages aren't exactly. *Science*, *282*, 1840–1841. https://doi.org/10.1126/science.282.5395.1840

Renne, P. R., Mundil, R., Balco, G., Min, K., & Ludwig, K. R. (2010). Joint determination of ^{40}K decay constants and $^{40}Ar/^{40}K$ for the Fish Canyon sanidine standard, and improved accuracy for $^{40}Ar/^{39}Ar$ geochronology. *Geochimica et Cosmochimica Acta*, *74*(18), 5349–5367. https://doi.org/10.1016/j.gca.2010.06.017

Renne, P. R., Sprain, C. J., Richards, M. A., Self, S., Vanderkluysen, L., & Pande, K. (2015). State shift in Deccan volcanism at the Cretaceous-Paleogene boundary, possibly induced by impact. *Science*. https://doi.org/10.1126/science.aac7549

Renne, P. R., Swisher, C. C., Deino, A. L., Karner, D. B., Owens, T. L., & DePaolo, D. J. (1998b). Intercalibration of standards, absolute ages and uncertainties in 40Ar/39Ar dating. *Chemical Geology*, *145*(1–2), 117–152. https://doi.org/10.1016/S0009-2541(97)00159-9

Renne, P. R., Zichao, Z., Richards, M. A., Black, M. T., & Basu, A. R. (1995). Synchrony and causal relations between Permian-Triassic boundary crises and siberian flood volcanism. *Science*. https://doi.org/10.1126/science.269.5229.1413

Ricci, J., Quidelleur, X., Pavlov, V. E., Orlov, S., Shatsillo, A., & Courtillot, V. E. (2013). New $^{40}Ar/^{39}Ar$ and K-Ar ages of the Viluy traps (Eastern Siberia): Further evidence for a relationship with the Frasnian-Famennian mass extinction.

Palaeogeography, Palaeoclimatology, Palaeoecology. https://doi.org/10.1016/j.palaeo.2013.06.020

Richards, M. A., Alvarez, W., Self, S., Karlstrom, L., Renne, P. R., Manga, M., et al. (2015). Triggering of the largest Deccan eruptions by the Chicxulub impact. *Geological Society of America Bulletin*, *127*(11–12), 1507–1520. https://doi.org/10.1130/B31167.1

Richards, M. A., Duncan, R. A., & Courtillot, V. E. (1989). Flood basalts and hot-spot tracks: plume heads and tails. *Science*, *246*(4926), 103–107. https://doi.org/10.1126/science.246.4926.103

Riley, T. R., Leat, P. T., Curtis, M. L., Millar, I. L., Duncan, R. A., & Fazel, A. (2005). Early-middle Jurassic dolerite dykes from western Dronning Maud Land (Antarctica): Identifying mantle sources in the Karoo large igneous province. *Journal of Petrology*, *46*(7), 1489-1524. https://doi.org/10.1093/petrology/egi023

Rioux, M., Bowring, S. A., Dudás, F., & Hanson, R. (2010). Characterizing the U-Pb systematics of baddeleyite through chemical abrasion: Application of multi-step digestion methods to baddeleyite geochronology. *Contributions to Mineralogy and Petrology*, *160*(5), 777–801. https://doi.org/10.1007/s00410-010-0507-1

Robinson, N., Ravizza, G., Coccioni, R., Peucker-Ehrenbrink, B., & Norris, R. D. (2009). A high-resolution marine $^{187}Os/^{188}Os$ record for the late Maastrichtian: Distinguishing the chemical fingerprints of Deccan volcanism and the KP impact event. *Earth and Planetary Science Letters*, *281*(3–4), 159–168. https://doi.org/10.1016/j.epsl.2009.02.019

Röhl, U., Westerhold, T., Bralower, T. J., & Zachos, J. C. (2007). On the duration of the Paleocene-Eocene thermal maximum (PETM). *Geochemistry, Geophysics, Geosystems, 8*(12). https://doi.org/10.1029/2007GC001784

Sageman, B. B., Meyers, S. R., & Arthur, M. A. (2006). Orbital time scale and new C-isotope record for Cenomanian-Turonian boundary stratotype. *Geology.* https://doi.org/10.1130/G22074.1

Saunders, A. D. (2016). Two LIPs and two Earth-system crises: The impact of the North Atlantic Igneous Province and the Siberian Traps on the Earth-surface carbon cycle. *Geological Magazine*, *153*(2), 201–222. https://doi.org/10.1017/S0016756815000175

Saunders, A. D., Fitton, J. G., Kerr, A. C., Norry, M. J., & Kent, R. W. (1997). The North Atlantic Igneous Province. In J. Mahoney & M. Coffin (Eds.), *Large igneous provinces: Continental, oceanic, and planetary flood volcanism* (pp. 45–93). Geophysical Monograph Series 100, American Geophysical Union.

Schlanger, S. O., & Jenkyns, H. C. (1976). Cretaceous oceanic anoxic events: Causes and consequences. *Geologie En Mijnbouw*, *55*(3–4), 179–184.

Schmitt, A. K. (2011). Uranium series accessory crystal dating of magmatic processes. *Annual Review of Earth and Planetary Sciences*, *39*(1), 321–349. https://doi.org/10.1146/annurev-earth-040610-133330

Schmitz, M. D., & Schoene, B. (2007). Derivation of isotope ratios, errors, and error correlations for U-Pb geochronology using ^{205}Pb-^{235}U-(^{233}U)-spiked isotope dilution thermal ionization mass spectrometric data. *Geochemistry, Geophysics, Geosystems*, *8*(8). https://doi.org/10.1029/2006GC001492

Schöbel, S., de Wall, H., Ganerød, M., Pandit, M. K., & Rolf, C. (2014). Magnetostratigraphy and ^{40}Ar-^{39}Ar geochronology of the Malwa plateau region (Northern Deccan Traps), central western India: Significance and correlation with the main Deccan Large Igneous Province sequences. *Journal of Asian Earth Sciences*, *89*, 28–45. https://doi.org/http://dx.doi.org/10.1016/j.jseaes.2014.03.022

Schoene, B. (2014). U-Th-Pb Geochronology. *Treatise on geochemistry (second edition)*, *4*, 341–378. https://doi.org/10.1016/B978-0-08-095975-7.00310-7

Schoene, B., Condon, D. J., Morgan, L. E., & McLean, N. M. (2013). Precision and accuracy in geochronology. *Elements*, *9*(1), 19–24. https://doi.org/10.2113/gselements.9.1.19

Schoene, B., Crowley, J. L., Condon, D. J., Schmitz, M. D., & Bowring, S. A. (2006). Reassessing the uranium decay constants for geochronology using ID-TIMS U-Pb data. *Geochimica et Cosmochimica Acta*, *70*(2), 426–445. https://doi.org/10.1016/j.gca.2005.09.007

Schoene, B., Eddy, M.P., Keller, C.B., Samperton, K.M. (in review, 2020). An evaluation of Deccan Traps eruption rates using geochronologic data, Geochronology Discuss, https://doi.org/10.5194/gchron-2020-11

Schoene, B., Eddy, M. P., Samperton, K. M., Keller, C. B., Keller, G., Adatte, T., & Khadri, S. F. R. (2019). U-Pb constraints on pulsed eruption of the Deccan Traps across the end-Cretaceous mass extinction. *Science*, *363*(6429), 862–866. https://doi.org/10.1126/science.aau2422

Schoene, B., Guex, J., Bartolini, A., Schaltegger, U., & Blackburn, T. J. (2010). Correlating the end-Triassic mass extinction and flood basalt volcanism at the 100 ka level. *Geology*, *38*(5), 387–390. https://doi.org/10.1130/G30683.1

Schoene, B., Samperton, K. M., Eddy, M. P., Keller, G., Adatte, T., Bowring, S. A., et al. (2015). U-Pb geochronology of the Deccan Traps and relation to the end-Cretaceous mass extinction. *Science*, *347*(6218), 182–184. https://doi.org/10.1126/science.aaa0118

Schulte, P., Alegret, L., Arenillas, I., Arz, J. A., Barton, P. J., Bown, P. R., et al. (2010). The Chicxulub asteroid impact and mass extinction at the Cretaceous-Paleogene boundary. *Science*, *327*(5970), 1214–1218. https://doi.org/10.1126/science.1177265

Self, S., Jay, A. E., Widdowson, M., & Keszthelyi, L. P. (2008). Correlation of the Deccan and Rajahmundry Trap lavas: Are these the longest and largest lava flows on Earth? *Journal of Volcanology and Geothermal Research*, *172*(1–2), 3–19. https://doi.org/10.1016/j.jvolgeores.2006.11.012

Self, S., Widdowson, M., Thordarson, T., & Jay, A. E. (2006). Volatile fluxes during flood basalt eruptions and potential effects on the global environment: A Deccan perspective. *Earth and Planetary Science Letters*, *248*(1–2), 517–531. https://doi.org/10.1016/j.epsl.2006.05.041

Sell, B., Ovtcharova, M., Guex, J., Bartolini, A., Jourdan, F., Spangenberg, J. E., et al. (2014). Evaluating the temporal link between the Karoo LIP and climatic-biologic events of the Toarcian Stage with high-precision U-Pb geochronology. *Earth and Planetary Science Letters.* https://doi.org/10.1016/j.epsl.2014.10.008

Sell, B., Ovtcharova, M., Guex, J., Bartolini, A., Jourdan, F., Spangenberg, J. E., et al. (2016). Response to comment on "Evaluating the temporal link between the Karoo LIP and

climatic-biologic events of the Toarcian Stage with high-precision U-Pb geochronology." *Earth and Planetary Science Letters*, *434*, 353–354. https://doi.org/10.1016/j.epsl.2015.07.016

Sepkoski, J. J. (1986). Phanerozoic overview of mass extinction. *Patterns and processes in the history of life*. Report of the Dahlem Workshop , Berlin 1985 (pp. 277–295).

Sheldon, N. D., Chakrabarti, R., Retallack, G. J., & Smith, R. M. H. (2014). Contrasting geochemical signatures on land from the Middle and Late Permian extinction events. *Sedimentology*. https://doi.org/10.1111/sed.12117

Shellnutt, J. G. (2014). The Emeishan large igneous province: A synthesis. *Geoscience Frontiers*. https://doi.org/10.1016/j.gsf.2013.07.003

Shellnutt, J. G., Denyszyn, S. W., & Mundil, R. (2012). Precise age determination of mafic and felsic intrusive rocks from the Permian Emeishan large igneous province (SW China). *Gondwana Research*. https://doi.org/10.1016/j.gr.2011.10.009

Shen, S., Crowley, J. L., Wang, Y., Bowring, S. A., Erwin, D. H., Sadler, P. M., et al. (2011). Calibrating the end-Permian mass extinction. *Science*. https://doi.org/10.1126/science.1213454

Shen, S.-Z., Ramezani, J., Chen, J., Cao, C.-Q., Erwin, D. H., Zhang, H., et al. (2018). A sudden end-Permian mass extinction in South China. *GSA Bulletin*, *131*(1–2), 205–223. https://doi.org/10.1130/B31909.1

Shevenell, A. E., Kennett, J. P., & Lea, D. W. (2004). Middle Miocene southern ocean cooling and Antarctic cryosphere expansion. *Science*, *305*, 1766–1770. https://doi.org/10.1126/science.1100061

Shrivastava, J. P., & Pattanayak, S. K. (2002). Basalts of the Eastern Deccan Volcanic Province, India. *Gondwana Research*, *5*(3), 649–665. https://doi.org/10.1016/S1342-937X(05)70636-5

Sinton, C. W., Duncan, R. A., Storey, M., Lewis, J., & Estrada, J. J. (1998). An oceanic flood basalt province within the Caribbean plate. *Earth and Planetary Science Letters*. https://doi.org/10.1016/S0012-821X(97)00214-8

Smit, J. (1999). The global stratigraphy of the Cretaceous-Tertiary Boundary impact ejecta. *Annual Review of Earth and Planetary Sciences*, *27*(1), 75–113. https://doi.org/10.1146/annurev.earth.27.1.75

Snow, L. J., Duncan, R. A., & Bralower, T. J. (2005). Trace element abundances in the Rock Canyon Anticline, Pueblo, Colorado, marine sedimentary section and their relationship to Caribbean plateau construction and ocean anoxic event 2. *Paleoceanography*, *20*(3), 1–14. https://doi.org/10.1029/2004PA001093

Söderlund, U., Ibanez-Mejia, M., El Bahat, A., Ernst, R. E., Ikenne, M., & Soulaimani, A. (2013). Reply to comment on "U-Pb baddeleyite ages and geochemistry of dolerite dykes in the Bas-Drâa inlier of the Anti-Atlas of Morocoo: Newly identified 1380 Ma event in the West African Craton" by André Michard and Dominique Gasquet. *Lithos*, *174*, 101–108. https://doi.org/10.1016/j.lithos.2013.04.003

Sprain, C. J., Renne, P. R., Clemens, W. A., & Wilson, G. P. (2018). Calibration of chron C29r: New high-precision geochronologic and paleomagnetic constraints from the Hell Creek region, *Montana. Geological Society of America Bulletin*. https://doi.org/10.1130/B31890.1

Sprain, C. J., Renne, P. R., Vanderkluysen, L., Pande, K., Self, S., & Mittal, T. (2019). The eruptive tempo of Deccan volcanism in relation to the Cretaceous-Paleogene boundary. *Science*, *363*(6429), 866–870. https://doi.org/10.1126/science.aav1446

Stolper, D. A., Bender, M. L., Dreyfus, G. B., Yan, Y., & Higgins, J. A. (2016). A Pleistocene ice core record of atmospheric O_2 concentrations. *Science*, *353*(6306), 1427–1430. https://doi.org/10.1126/science.aaf5445

Storey, M., Duncan, R. A., & Swisher, C. C. (2007a). Paleocene-Eocene thermal maximum and the opening of the northeast Atlantic. *Science*, *316*(5824), 587–589. https://doi.org/10.1126/science.1135274

Storey, M., Duncan, R. A., & Tegner, C. (2007b). Timing and duration of volcanism in the North Atlantic Igneous Province: Implications for geodynamics and links to the Iceland hotspot. *Chemical Geology*, *241*(3–4), 264–281. https://doi.org/10.1016/j.chemgeo.2007.01.016

Storey, M., Mahoney, J. J., Saunders, A. D., Duncan, R. A., Kelley, S. P., & Coffin, M. F. (1995). Timing of hot spot-related volcanism and the breakup of Madagascar and India. *Science*, *267*(5199), 852–855. https://doi.org/10.1126/science.267.5199.852

Suan, G., Nikitenko, B. L., Rogov, M. A., Baudin, F., Spangenberg, J. E., Knyazev, V. G., et al. (2011). Polar record of Early Jurassic massive carbon injection. *Earth and Planetary Science Letters*, *312*(1–2), 102–113. https://doi.org/10.1016/j.epsl.2011.09.050

Suan, G., Pittet, B., Bour, I., Mattioli, E., Duarte, L. V., & Mailliot, S. (2008). Duration of the Early Toarcian carbon isotope excursion deduced from spectral analysis: Consequence for its possible causes. *Earth and Planetary Science Letters*, *267*(3–4), 666–679. https://doi.org/10.1016/j.epsl.2007.12.017

Subbarao, K. V., Bodas, M. S., Khadri, S. F. R., & Beane, J. E. (2000). Penrose Deccan 2000, field excursion guide to the Western Deccan Basalt Province. *Penrose Field Guides, B. Geological Society of India, Ed*.

Sun, Y., Joachimski, M. M., Wignall, P. B., Yan, C., Chen, Y., Jiang, H., et al. (2012). Lethally hot temperatures during the early Triassic greenhouse. *Science*. https://doi.org/10.1126/science.1224126

Svensen, H. H., Corfu, F., Polteau, S., Hammer, Ø., & Planke, S. (2012). Rapid magma emplacement in the Karoo Large Igneous Province. *Earth and Planetary Science Letters*, *325–326*, 1–9. https://doi.org/10.1016/j.epsl.2012.01.015

Svensen, H. H., Planke, S., & Corfu, F. (2010). Zircon dating ties NE Atlantic sill emplacement to initial Eocene global warming. *Journal of the Geological Society*, *167*(3), 433–436. https://doi.org/10.1144/0016-76492009-125

Svensen, H. H., Planke, S., Malthe-Sørenssen, A., Jamtveit, B., Myklebust, R., Eidem, T. R., & Rey, S. S. (2004). Release of methane from a volcanic basin as a mechanism for initial Eocene global warming. *Nature*, *429*(6991), 542. https://doi.org/10.1038/nature02566

Svensen, H. H., Planke, S., Polozov, A. G., Schmidbauer, N., Corfu, F., Podladchikov, Y. Y., & Jamtveit, B. (2009). Siberian gas venting and the end-Permian environmental crisis. *Earth and Planetary Science Letters*. https://doi.org/10.1016/j.epsl.2008.11.015

Svensen, H. H., Polteau, S., Cawthorn, G., & Planke, S. (2015). Sub-volcanic Intrusions in the Karoo Basin, South Africa. In *Physical Geology of Shallow Magmatic Systems* (pp. 349–362). Springer, Cham. https://doi.org/10.1007/11157_2014_7

Tanner, L. H., Lucas, S. G., & Chapman, M. G. (2004). Assessing the record and causes of Late Triassic extinctions. *Earth-Science Reviews*, *65*, 15–103. https://doi.org/10.1016/S0012-8252(03)00082-5

Tarduno, J. A., Sliter, W. V., Kroenke, L., Leckie, R. M., Mayer, H., Mahoney, J. J., et al. (1991). Rapid formation of Ontong Java plateau by Aptian mantle plume volcanism. *Science*. https://doi.org/10.1126/science.254.5030.399

Tejada, M. L. G., Mahoney, J. J., Duncan, R. A., & Hawkins, M. P. (1996). Age and geochemistry of basement and Alkalic rocks of Malaita and Santa Isabel, Solomon Islands, southern margin of Ontong Java plateau. *Journal of Petrology*, *37*(2), 361–394. https://doi.org/10.1093/petrology/37.2.361

Tejada, M. L. G., Mahoney, J. J., Neal, C. R., Duncan, R. A., & Petterson, M. G. (2002). Basement geochemistry and geochronology of central Malaita, Solomon Islands, with implications for the origin and evolution of the Ontong Java plateau. *Journal of Petrology*, *43*(3), 449–484. https://doi.org/10.1093/petrology/43.3.449

Tejada, M. L. G., Suzuki, K., Kuroda, J., Coccioni, R., Mahoney, J. J., Ohkouchi, N., et al. (2009). Ontong Java plateau eruption as a trigger for the early Aptian oceanic anoxic event. *Geology*, *37*(9), 855–858. https://doi.org/10.1130/G25763A.1

Thibault, N., Galbrun, B., Gardin, S., Minoletti, F., & Le Callonnec, L. (2016). The end-Cretaceous in the southwestern Tethys (Elles, Tunisia): Orbital calibration of paleoenvironmental events before the mass extinction. *International Journal of Earth Sciences*. https://doi.org/10.1007/s00531-015-1192-0

Thordarson, T., & Self, S. (1996). Sulfur, chlorine and fluorine degassing and atmospheric loading by the Roza eruption, Columbia River Basalt Group, Washington, USA. *Journal of Volcanology and Geothermal Research*, *74*(1–2), 49–73. https://doi.org/10.1016/S0377-0273(96)00054-6

Tobin, T. S., Ward, P. D., Steig, E. J., Olivero, E. B., Hilburn, I. A., Mitchell, R. N., et al. (2012). Extinction patterns, $\delta^{18}O$ trends, and magnetostratigraphy from a southern high-latitude Cretaceous-Paleogene section: Links with Deccan volcanism. *Palaeogeography, Palaeoclimatology, Palaeoecology*, *350–352*(0), 180–188. https://doi.org/http://dx.doi.org/10.1016/j.palaeo.2012.06.029

Turgeon, S. C., & Creaser, R. A. (2008). Cretaceous oceanic anoxic event 2 triggered by a massive magmatic episode. *Nature*, *454*(7202), 323–326. https://doi.org/10.1038/nature07076

Turgeon, S. C., Creaser, R. A., & Algeo, T. J. (2007). Re-Os depositional ages and seawater Os estimates for the Frasnian-Famennian boundary: Implications for weathering rates, land plant evolution, and extinction mechanisms. *Earth and Planetary Science Letters*. https://doi.org/10.1016/j.epsl.2007.07.031

Venkatesan, T. R., Kumar, A., Gopalan, K., & Al'Mukhamedov, A. I. (1997). ^{40}Ar-^{39}Ar age of Siberian basaltic volcanism. *Chemical Geology*. https://doi.org/10.1016/S0009-2541(97)00006-5

Venkatesan, T. R., Pande, K., & Gopalan, K. (1993). Did Deccan volcanism pre-date the Cretaceous/Tertiary transition? *Earth and Planetary Science Letters*, *119*(1–2), 181–189. https://doi.org/10.1016/0012-821X(93)90015-2

Verati, C., Bertrand, H., & Féraud, G. (2005). The farthest record of the Central Atlantic Magmatic Province into West Africa craton: Precise $^{40}Ar/^{39}Ar$ dating and geochemistry of Taoudenni basin intrusives (northern Mali). *Earth and Planetary Science Letters*, *235*(1–2), 391–407. https://doi.org/10.1016/j.epsl.2005.04.012

Vernikovsky, V., Vernikovskaya, A., Kotov, A., Sal'nikova, E. B., & Kovach, V.P. (2003). Neoproterozoic accretionary and collisional events on the western margin of the Siberian craton: New geological and geochronological evidence from the Yenisey Ridge. *Tectonophysics*, *375*(1-4), 147-168. https://doi.org/10.1016/S0040-1951(03)00337-8

Voigt, S., Erbacher, J., Mutterlose, J., Weiss, W., Westerhold, T., Wiese, F., et al. (2008). The Cenomanian-Turonian of the Wunstorf section (North Germany): Global stratigraphic reference section and new orbital time scale for Oceanic Anoxic Event 2. *Newsletters on Stratigraphy*, *43*(1), 65–89. https://doi.org/10.1127/0078-0421/2008/0043-0065

Von Hillebrandt, A. V, Krystyn, L., & Kürschner, W. M. (2007). A candidate GSSP for the base of the Jurassic in the Northern Calcareous Alps (Kuhjoch section, Karwendel Mountains, Tyrol, Austria). *International Subcommission on Jurassic Stratigraphy Newsletter*, *34*(1), 2–20.

Walderhaug, H. J., Eide, E. A., Scott, R. A., Inger, S., & Golionko, E. G. (2005). Palaeomagnetism and $^{40}Ar/^{39}Ar$ geochronology from the South Taimyr igneous complex, Arctic Russia: A Middle-Late Triassic magmatic pulse after Siberian flood-basalt volcanism. *Geophysical Journal International*, *163*(2), 501–517. https://doi.org/10.1111/j.1365-246X.2005.02741.x

Ware, B., & Jourdan, F. (2018). $^{40}Ar/^{39}Ar$ geochronology of terrestrial pyroxene. *Geochimica et Cosmochimica Acta*, *230*, 112–136. https://doi.org/10.1016/j.gca.2018.04.002

Wendt, I., & Carl, C. (1991). The statistical distribution of the mean squared weighted deviation. *Chemical Geology: Isotope Geoscience Section*, *86*(4), 275–285. https://doi.org/10.1016/0168-9622(91)90010-T

Westerhold, T., Röhl, U., & Laskar, J. (2012). Time scale controversy: Accurate orbital calibration of the early Paleogene. *Geochemistry, Geophysics, Geosystems*, 13(6). https://doi.org/10.1029/2012GC004096

Westerhold, T., Röhl, U., McCarren, H. K., & Zachos, J. C. (2009). Latest on the absolute age of the Paleocene-Eocene Thermal Maximum (PETM): New insights from exact stratigraphic position of key ash layers +19 and −17. *Earth and Planetary Science Letters*, *287*(3–4), 412–419. https://doi.org/10.1016/j.epsl.2009.08.027

Westerhold, T., Röhl, U., Raffi, I., Fornaciari, E., Monechi, S., Reale, V., et al. (2008). Astronomical calibration of the Paleocene time. *Palaeogeography, Palaeoclimatology, Palaeoecology*, *257*(4), 377–403. https://doi.org/10.1016/J.PALAEO.2007.09.016

White, R. S., Spence, G. D., Fowler, S. R., McKenzie, D. P., Westbrook, G. K., & Bowen, A. N. (1987). Magmatism at rifted continental margins. *Nature*, *330*(6147), 439. https://doi.org/10.1038/330439a0

Whiteside, J. H., Olsen, P. E., Kent, D. V., Fowell, S. J., & Et-Touhami, M. (2007). Synchrony between the Central Atlantic magmatic province and the Triassic-Jurassic mass-extinction event? *Palaeogeography, Palaeoclimatology, Palaeoecology*, *244*(1–4), 345–367. https://doi.org/10.1016/j.palaeo.2006.06.035

Wignall, P. B. (2001). Large igneous provinces and mass extinctions. *Earth Science Reviews*, *53*(1–2), 1–33. https://doi.org/10.1016/S0012-8252(00)00037-4

Wignall, P. B., Sun, Y., Bond, D. P. G., Izon, G., Newton, R. J., Védrine, S., et al. (2009). Volcanism, mass extinction, and carbon isotope fluctuations in the Middle Permian of China. *Science (New York, N.Y.)*, *324*(5931), 1179–82. https://doi.org/10.1126/science.1171956

Wilf, P., Johnson, K. R., & Huber, B. T. (2003). Correlated terrestrial and marine evidence for global climate changes before mass extinction at the Cretaceous-Paleogene boundary. *Proceedings of the National Academy of Sciences*, *100*(2), 599–604. https://doi.org/10.1073/pnas.0234701100

Wilkinson, C. M., Ganerød, M., Hendriks, B. W. H., & Eide, E. A. (2017). Compilation and appraisal of geochronological data from the North Atlantic Igneous Province (NAIP). *Geological Society, London, Special Publications*, *447*(1), 69–103. https://doi.org/10.1144/SP447.10

Williams, G. E., & Gostin, V. A. (2000). Mantle plume uplift in the sedimentary record: Origin of kilometre-deep canyons within late Neoproterozoic successions, south Australia. *Journal of the Geological Society, London.* https://doi.org/10.1144/jgs.157.4.759

Wilson, G. P. (2014). Mammalian extinction, survival, and recovery dynamics across the Cretaceous-Paleogene boundary in northeastern Montana, *USA. Geological Society of America Special Papers*, *503*, 365–392. https://doi.org/10.1130/2014.2503(15)

Wilson, G. P., DeMar, D. G., & Carter, G. (2014). Extinction and survival of salamander and salamander-like amphibians across the Cretaceous-Paleogene boundary in northeastern Montana, *USA. Geological Society of America Special Papers*, *503*, 271–297. https://doi.org/10.1130/2014.2503(10)

Wotzlaw, J.-F., Bindeman, I. N., Schaltegger, U., Brooks, C. K., & Naslund, H. R. (2012). High-resolution insights into episodes of crystallization, hydrothermal alteration and remelting in the Skaergaard intrusive complex. *Earth and Planetary Science Letters*, *355–356*, 199–212. https://doi.org/10.1016/j.epsl.2012.08.043

Wotzlaw, J.-F., Guex, J., Bartolini, A., Gallet, Y., Krystyn, L., McRoberts, C. A., et al. (2014). Towards accurate numerical calibration of the Late Triassic: High-precision U-Pb geochronology constraints on the duration of the Rhaetian. *Geology*, *42*(7), 571–574. https://doi.org/10.1130/G35612.1

Wotzlaw, J.-F., Schaltegger, U., Frick, D. A., Dungan, M. A., Gerdes, A., & Günther, D. (2013). Tracking the evolution of large-volume silicic magma reservoirs from assembly to supereruption. *Geology*, *41*(8), 867–870. https://doi.org/10.1130/G34366.1

Wu, H., Zhang, S., Hinnov, L. A., Jiang, G., Feng, Q., Li, H., & Yang, T. (2013). Time-calibrated Milankovitch cycles for the late Permian. *Nature Communications*, *4*. https://doi.org/10.1038/ncomms3452

Zachos, J. C., Dickens, G. R., & Zeebe, R. E. (2008). An early Cenozoic perspective on greenhouse warming and carbon-cycle dynamics. *Nature*, *451*, 279–283. https://doi.org/10.1038/nature06588

Zachos, J. C., Pagani, M., Sloan, L., Thomas, E., & Billups, K. (2001). Trends, rhythms, and aberrations in global climate 65 Ma to present. *Science*, *292*(5517), 686–693. https://doi.org/10.1126/science.1059412

Zachos, J. C., Röhl, U., Schellenberg, S. A., Sluijs, A., Hodell, D. A., Kelly, D. C., et al. (2005). Rapid acidification of the ocean during the Paleocene-Eocene thermal maximum. *Science*, *308*(5728), 1611–1615. https://doi.org/10.1126/science.1109004

Zhang, Y. G., Pagani, M., Liu, Z., Bohaty, S. M., & Deconto, R. (2013). A 40-million-year history of atmospheric CO_2. *Philosophical Transactions of the Royal Society of London.*, (September). https://doi.org/10.1098/rsta.2013.0096

Zheng, L., Yang, Z., Tong, Y., & Yuan, W. (2010). Magnetostratigraphic constraints on two-stage eruptions of the Emeishan continental flood basalts. *Geochemistry, Geophysics, Geosystems.* https://doi.org/10.1029/2010GC003267

Zhong, Y. T., He, B., Mundil, R., & Xu, Y. G. (2014). CA-TIMS zircon U-Pb dating of felsic ignimbrite from the Binchuan section: Implications for the termination age of Emeishan large igneous province. *Lithos.* https://doi.org/10.1016/j.lithos.2014.03.005

Zhuravlev, A. Y., & Wood, R. A. (1996). Anoxia as the cause of the mid-Early Cambrian (Botomian) extinction event. *Geology.* https://doi.org/10.1130/0091-7613(1996)024<0311:AATCOT>2.3.CO;2